

**Electroquasistatic Sensors for Surface and Subsurface Nano-
Imaging of Integrated Circuit Features**

by

Benjamin L. Cannon

B.S., Electrical and Computer Engineering
Carnegie Mellon University, 2008

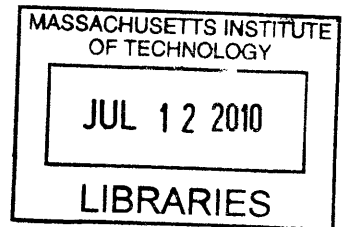
Submitted to the Department of Electrical Engineering and Computer Science in
partial fulfillment of the requirements for the degree of

Master of Science in Electrical Engineering

at the

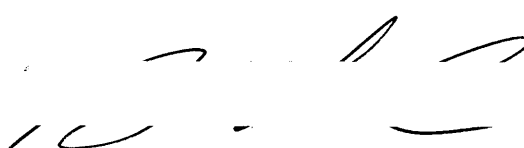
MASSACHUSETTS INSTITUTE OF TECHNOLOGY

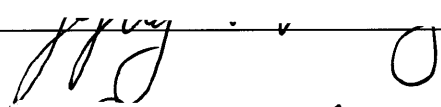
June 2010



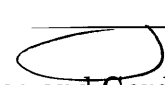
© Massachusetts Institute of Technology, 2010. All rights reserved.

ARCHIVES

Author 
Department of Electrical Engineering and Computer Science
May 17, 2010

Certified by  Thesis Supervisor: Jeffrey H. Lang
Professor of Electrical Engineering

Certified by  Thesis Supervisor: David L. Trumper
Professor of Mechanical Engineering

Certified by  Thesis Supervisor: Markus Zahn
Thomas and Gerd Perkins Professor of Electrical Engineering

Accepted by  Terry P. Orlando
Chair, Department Committee on Graduate Students

Electroquasistatic Sensors for Surface and Subsurface Nano-Imaging of Integrated Circuit Features

by

Benjamin L. Cannon

Submitted to the Department of Electrical Engineering and Computer Science on
May 17, 2010, in partial fulfillment of the requirements for the degree of

Master of Science in Electrical Engineering

Abstract

The following thesis relates to the design, simulation, and testing of electroquasistatic (EQS) sensors to be used for feature/defect location and imaging. The aim of this thesis is to launch an investigation into the use of EQS sensor arrays for non-destructive evaluation and quality control purposes for integrated circuit industry applications. Research into three specific areas serves as the primary focus of the thesis:

1.) The use of EQS sensors to penetrate the surface of doped silicon and locate p-n junctions and doped wells. Arrays of coplanar EQS sensors are scanned laterally over the surface of a doped silicon bulk at a fixed scan height. Electric fields from the driven EQS sensor array are capable of penetrating the surface of the semiconductor when sensors are operated at a frequency comparable to its charge relaxation break frequency. It is demonstrated through finite element method (FEM) simulations that voltage-driven EQS electrodes can couple into the p-n junction without making any direct electrical contact with the semiconducting bulk. A new methodology for locating p-n junctions is presented where the currents on these voltage-driven sensors are monitored for harmonic distortion due to the junction's nonlinear drift/diffusion carrier dynamics. With sensors located over a p-n junction at a scan height of 200 nm and driven at 1GHz, the ratio of the second harmonic current to the fundamental current on a sensor is shown to exceed 9%. Such an IC imaging technique could prove to be useful for verification and detection of fabrication errors, externally monitoring current flows, as well as detecting hidden Trojan circuits that might be present.

2.) The use of EQS sensors to locate and image surface features and contaminant objects on photomasks. Motivation for research into this area comes from the desire to be able to locate and remove contaminant particles that might be present on extreme ultraviolet lithography (EUVL) photomasks used in the mass production of next-generation integrated circuits. FEM simulation results demonstrate the sensitivity of EQS sensor arrays in detecting various contaminant particles located

in a 100nm wide by 70nm deep gap in the absorber layer of an EUVL photomask. A millimeter-scale, in-lab experiment using capacitive sensors is performed with sensors and materials having similar aspect ratios and electrical properties to those simulated. Experiments demonstrate both the capabilities and limitations of sensors in detecting various objects located in a trenches milled out of aluminum. Additionally, a discussion of the need for low-noise pickup circuitry to interface with sensors is presented.

3.) An investigation into the inversion of sensor transimpedance response signals into predicted feature/defect profiles. In this case study, an inverse electromagnetic sensor problem is solved by training a radial basis function artificial neural network (RBF-ANN) to accurately approximate the forward mapping of the physical dimensions (width and depth) of a high aspect ratio trench in doped silicon into a sensor's transimpedance response as the sensor array scans past the trench at a fixed scan height. This is an example of the type of inverse problem that might be encountered in an EQS array microscope and one possible approach to its solution. The function-approximation network is then inserted into an iterative signal inversion routine which converges to a prediction for the trench's dimensions, given a measured transimpedance response. The routine is capable of predicting trench dimensions to within 1% of their actual value.

In all three cases, research involves extensive finite element method (FEM) simulations of sensor performance using COMSOL Multiphysics.

Thesis Supervisors:

Jeffrey H. Lang
Professor of Electrical Engineering

David L. Trumper
Professor of Mechanical Engineering

Markus Zahn
Thomas and Gerd Perkins Professor of Electrical Engineering

Acknowledgements

I have many people to thank for making the last two years at MIT both a rich and enjoyable experience.

I want to first thank my thesis advisors—Profs. Jeff Lang, Dave Trumper, and Mark Zahn—for their incredible amount of knowledge, advice, and guidance. Having the chance to meet with these three outstanding MIT professors on a weekly basis was truly a privilege. Being a triple-advised master’s student (sounds scary, right?) undoubtedly broadened my knowledge base and the scope of my thesis, and for that I am extremely grateful. I must extend a very special thanks to Professor Lang for always so very quickly setting me on the right path whenever I needed help.

I would also like to thank many other members of the LEES community. A special thanks goes out to the following individuals, with whom brief conversations saved me many hours of spinning tires: Shahriar, Brandon, Warit, Al, Tony, and George. Thanks to the rest of the folks on the 10-061 side of town for many enjoyable moments in the office.

I’m not sure I can ever repay my parents for all they have done for me. I can only say “thank you” and hope that this thesis can serve as a symbol of appreciation for all their support for me both academically and in life. I’d also like to Sara for being such a great sister and friend. Cannons rule.

Finally, I thank my loving fiancée Stephanie for all the support and listening to me vent all too often. A girl who is willing to spend her Saturday night coding up some C++ for you in the lab is a keeper. I love you.

Contents

1	Introduction.....	17
1.1	Theory and Background of Electromagnetic Sensors	18
1.2	Scanning Force Microscopy Methods.....	23
1.3	Thesis Overview.....	25
2	Subsurface Sensor Application: Locating a p-n Junction.....	29
2.1	The p-n Junction Diode	30
2.2	Coupling into a p-n Junction Diode through an Air Gap.....	33
2.3	FEM Model #1 Setup.....	34
2.3.1	Geometric Properties	34
2.3.2	Physical Properties	36
2.3.3	Solver Properties.....	37
2.4	FEM Model #1 Simulation Results.....	40
2.4.1	Charge Relaxation.....	44
2.4.2	Results	45
2.5	FEM Model #2 Setup.....	56
2.5.1	Geometric Properties	56
2.5.2	Physical Properties	58
2.5.3	Solver Properties.....	59
2.6	FEM Model #2 Simulation Results.....	60
2.7	FEM Model #2 Sensor Scan Results	68
3	Locating Surface Features and Contaminants	75
3.1	Detecting Contaminants on a Photomask	76
3.1.1	Contaminated Photomask Simulation Setup	77
3.1.2	Contaminated Photomask Results	80
3.2	Laboratory Experiment.....	85

3.2.1	Laboratory Setup	86
3.2.2	Experimental Results	91
3.3	Low-Noise Pickup Circuitry	99
4	Sensor Signal Inversion through a Radial Basis Function Artificial Neural Network.....	115
4.1	Simulating the Forward Problem	116
4.2	Solving the Inverse Problem	119
4.2.1	Artificial Neural Networks (ANNs): Training and Operation	121
4.2.2	Training Results.....	124
4.2.3	Signal Inversion Results.....	127
5	Conclusions and Suggestions for Future Work.....	133
	Bibliography.....	137
	Appendix A: MATLAB Code for Iterative Signal Inversion Routine	139
	Appendix B: COMSOL Settings for p-n Junction Geometry #1	141
	Appendix C: COMSOL Settings for p-n Junction Geometry #2	157
	Appendix D: COMSOL Settings for Contaminated Photomask	173

List of Figures

Figure 1-1: Multiple wavelength coplanar EQS sensor [4]. Such a sensor is useful for penetrating dielectric or poorly conducting substrates to multiple depths, providing both lateral and depth resolution.....	21
Figure 1-2: Generic interdigital EQS sensor [4].....	21
Figure 1-3: Parallel plate capacitor (a) opened to form fringing field capacitor (b)..	22
Figure 1-4: Forward/Inverse problem cycle.....	23
Figure 2-1: p-n Junction under static equilibrium.....	32
Figure 2-2: COMSOL geometry #1 to be analyzed.....	35
Figure 2-3: Boundary conditions for COMSOL geometry #1.....	39
Figure 2-4: Initial Concentration of holes (a) and electrons (b) in $[1/m^3]$ shown as a 3-D colormapped surface plot.....	41
Figure 2-5: Initial space charge density $[C/m^3]$ shown as both a 2-D and 3-D colormapped surface plot.....	42
Figure 2-6: Initial scalar potential $[V]$ shown as both a 2-D and 3-D colormapped surface plot.....	42
Figure 2-7: Integration path (shown in red) for surface charge density integration to simulate guarded electrodes in Figure 2-8.	43
Figure 2-8: Sensor drive scheme with individual guard electrodes shown.	44
Figure 2-9: FFT of sensor current magnitude per unit depth $[A/m]$ at 1GHz fundamental drive. In this lower frequency limit, no harmonic distortion is witnessed in the sensor current.	46
Figure 2-10: FFT of sensor current magnitude per unit depth $[A/m]$ at 5GHz fundamental drive. Harmonic distortion begins to show up in the sensor current.	46
Figure 2-11: FFT of sensor current magnitude per unit depth $[A/m]$ at 10GHz fundamental drive.	47
Figure 2-12: FFT of sensor current magnitude per unit depth $[A/m]$ at 50GHz fundamental drive.	47
Figure 2-13: FFT of sensor current magnitude per unit depth $[A/m]$ at 100GHz fundamental drive.	48
Figure 2-14: Ratio of 2 nd harmonic amplitude to 1 st harmonic amplitude (expressed as a percentage) vs. fundamental drive frequency $[Hz]$	48
Figure 2-15: Scalar potential $[V]$ at $t=T/10$ for 1GHz drive.....	49

Figure 2-16: Colormapped surface plots of scalar potential [V] (a1—a10) and space charge density [C/m ³] (b1—b10) at intervals of length T/10 for 10GHz excitation. .	54
Figure 2-17: Electric field (streamlines) and space charge density [C/m ³] (colormapped surface plot) when silicon region is under forward bias.	55
Figure 2-18: COMSOL geometry #2 to be analyzed.....	57
Figure 2-19: Zoomed-in version of COMSOL geometry #2 to show important geometric dimensions.	57
Figure 2-20: Boundary conditions for COMSOL geometry #2.....	60
Figure 2-21: Log ₁₀ (initial concentration of holes) in [1/m ³] displayed as a 3-D (left) and 2-D (right) colormap.	61
Figure 2-22: Log ₁₀ (initial concentration of electrons) in [1/m ³] displayed as a 3-D (left) and 2-D (right) colormap (note: 3-D view is shown at a reverse angle of Figure 2-21).....	61
Figure 2-23: Initial scalar potential distribution [V]. There exists a built-in equilibrium potential of approximately 0.6 V across the p-n junction.	62
Figure 2-24: Initial space charge density [C/m ³] zoomed in near p-well to illustrate the width of the depletion region.	62
Figure 2-25: Integration path for simulating a guarded electrode.....	64
Figure 2-26: FFT of sensor current magnitude per unit depth [A/m] at 500MHz fundamental drive.	64
Figure 2-27: FFT of sensor current magnitude per unit depth [A/m] at 1GHz fundamental drive.	65
Figure 2-28: FFT of sensor current magnitude per unit depth [A/m] at 5GHz fundamental drive.	65
Figure 2-29: FFT of sensor current magnitude per unit depth [A/m] at 10GHz fundamental drive.	66
Figure 2-30: FFT of sensor current magnitude per unit depth [A/m] at 50GHz fundamental drive.	66
Figure 2-31: Ratio of 2 nd harmonic amplitude to 1 st harmonic amplitude of center sensor current per unit depth (expressed as a percentage) vs. fundamental drive frequency [Hz]......	67
Figure 2-32: Horizontal scan of sensor array past a p-type well in an n-type bulk. The sensor array is scanned from 8μm left-of-center to 8μm right-of-center in 2μm increments (nine total positions). The sensor array is shown to be moving from its leftmost position (solid sensors) to its rightmost position (dashed sensors).	69
Figure 2-33: FFT of center sensor current magnitude per unit depth [A/m] when positioned 0μm left-of-center. 1GHz fundamental drive frequency.	69
Figure 2-34: FFT of center sensor current magnitude per unit depth [A/m] when positioned 2μm left-of-center. 1GHz fundamental drive frequency. False	

subharmonics are present in the FFT because the sensor current did not reach perfect sinusoidal steady state in the COMSOL simulation. This creates a periodically modulated envelope on the waveform which causes unwanted spikes in the frequency spectrum. 70

Figure 2-35: FFT of center sensor current magnitude per unit depth [A/m] when positioned 4 μ m left-of-center. 1GHz fundamental drive frequency. Again, false subharmonics are present in the FFT because the sensor current did not reach perfect sinusoidal steady state in the COMSOL simulation. This creates a periodically modulated envelope on the waveform which causes small, unwanted spikes in the frequency spectrum. 70

Figure 2-36: FFT of center sensor current magnitude per unit depth [A/m] when positioned 6 μ m left-of-center. 1GHz fundamental drive frequency. 71

Figure 2-37: FFT of center sensor current magnitude per unit depth [A/m] when positioned 8 μ m left-of-center. 1GHz fundamental drive frequency. 71

Figure 2-38: Ratio of 2nd harmonic amplitude to 1st harmonic amplitude of center sensor current per unit depth (expressed as a percentage) vs. horizontal position [μ m] (relative to the center of the p-well). 72

Figure 3-1: Illustration of contaminated photomask. 76

Figure 3-2: COMSOL geometry for contaminated EUVL photomask simulation. Since simulation is performed on 2D solvers, contaminant object is cylindrical..... 77

Figure 3-3: Two-dimensional COMSOL simulation results with cylindrical contaminant particle positioned 200nm right of center. In this case, the contaminant particle is characterized by a dielectric constant of $\epsilon_r = 4$. Purple streamlines are electric field lines and the colormapped contours represent equipotentials (lines of constant voltage [V]). 80

Figure 3-4: Sensors 1, 2, 3, and 4 current magnitudes per-unit-depth [A/m] vs. horizontal position [nm] relative to center of absorber layer gap..... 82

Figure 3-5: COMSOL simulation results for reduced sensor size (50nm width) with contaminant particle positioned 130nm right-of-center. Contaminant particle is characterized by dielectric constant of $\epsilon_r = 4$. Purple streamlines are electric field lines and the colormapped contours represent equipotentials (lines of constant voltage [V]). 83

Figure 3-6: Sensor 3 and Sensor 4 current magnitudes per-unit-depth [A/m] vs. position [nm]. 84

Figure 3-7: Experiment block diagram. 86

Figure 3-8: Capacitance detection electronics (top view). AD7747 capacitance-to-digital converter is shown to the left. 87

Figure 3-9: Various capacitive sensors (bottom view). 87

Figure 3-10: Capacitive sensor (side view). 88

Figure 3-11: Trenches milled out of aluminum bar to represent absorber layer gaps of various depths and widths.	89
Figure 3-12: Laboratory setup (top view).	90
Figure 3-13: Laboratory setup (side view).	90
Figure 3-14: Capacitive sensor over contaminant filled trench. Contaminants of various shapes, sizes, and material properties were used.	91
Figure 3-15: Cross-sections of various “contaminant” objects in 5.15mm×9.13mm trench. An empty trench is shown in (a) and the six objects that were tested include: (b) copper rod with square cross-section, (c) copper cylindrical rod, (d) stainless steel cylindrical rod, (e) aluminum cylindrical rod, (f) styrene plastic cylindrical rod, and (g) polymer modeling clay rolled into a cylindrical rod.	92
Figure 3-16: Sensor-Sample capacitance [pF] vs. horizontal position [mm] for 5.75mm scan height.	94
Figure 3-17: Sensor-Sample capacitance [pF] vs. horizontal position [mm] for 7.75mm scan height.	95
Figure 3-18: Cross-sections of various “contaminant” objects in 9.1mm×8.8mm trench. A empty trench is shown in (a) and the six objects that were tested include: (b) copper rod with square cross-section, (c) copper cylindrical rod, (d) stainless steel cylindrical rod, (e) aluminum cylindrical rod, (f) styrene plastic cylindrical rod, and (g) polymer modeling clay rolled into a cylindrical rod.	96
Figure 3-19: Sensor-Sample capacitance [pF] vs. horizontal position [mm] for 5.75mm scan height. Figure (b) is a zoomed-in version of the trough in Figure (a).	97
Figure 3-20: Sensor-Sample capacitance [pF] vs. horizontal position [mm] for 7.75mm scan height. Figure (b) is a zoomed-in version of the trough in Figure (a).	97
Figure 3-21: COMSOL geometry for contaminated EUVL photomask simulation.	100
Figure 3-22: Lumped circuit model of EQS sensor-substrate interaction.	101
Figure 3-23: Electric potential [V] along absorber layer surface vs. horizontal position [nm] with sensor head centered over absorber layer gap.	101
Figure 3-24: Sensor-substrate interaction parameters for depth of 100nm.	103
Figure 3-25: Sensor signal detection circuit.	104
Figure 3-26: Resistor thermal noise model [26].	105
Figure 3-27: Circuit for evaluating output noise due to R_{absorb} only.	106
Figure 3-28: Circuit for evaluating output noise due to R_f only.	107
Figure 3-29: R_{absorb} and C_{air} transformed into impedance Z_{in}	107
Figure 3-30: Output voltage noise PSD due to R_{absorb} vs. ω for various turns ratios N.	109
Figure 3-31: Output voltage noise PSD due to R_f vs. ω (independent of N).	109
Figure 3-32: SNR at output for various turns ratios.	111

Figure 3-33: SNR at output for various turns ratios for 1V, 5V, and 10V sensor drive at 1GHz drive frequency.....	112
Figure 3-34: SNR at output for various turns ratios for 1V, 5V, and 10V sensor drive at 5GHz drive frequency.....	113
Figure 4-1: COMSOL geometry for locating trenches of various dimensions (depth and width) in doped silicon with an array of coplanar EQS electrodes.....	116
Figure 4-2: COMSOL simulation results with 300nm×25nm trench positioned 100nm right of center. Red streamlines are electric field lines and the blue contours represent equipotentials (lines of constant voltage). For simplicity, fields from guard electrodes are not shown.....	118
Figure 4-3: Sensor 2 – Sensor 5 transimpedance [$\Omega \cdot m$] vs. sensor head position [nm] for trenches of various depths and widths. In this case impedance has units of [$\Omega \cdot m$] because the simulation is performed on a 2D solver. Figure (a) shows a family of responses for trenches of varying depths with width fixed at 50nm, Figure (b) shows a family of responses for trenches of varying widths with depth fixed at 100nm. .	119
Figure 4-4: Iterative signal inversion block diagram [31].	120
Figure 4-5: RBF-ANN basic architecture.	121
Figure 4-6: MATLAB RBF-ANN architecture details [32].	122
Figure 4-7: Training data inputs.....	124
Figure 4-8: Screenshot of iterative RBF network training progress. The network reaches its sum-squared error goal of 1×10^{-6} after adding 29 neurons.	125
Figure 4-9: Forward model prediction performance for exact-trained and iteratively-trained RBF networks. Results are for a trench that is 100nm deep and 80nm wide.	126
Figure 4-10: Forward model prediction performance for exact-trained and iteratively-trained RBF networks. Results are for a trench that is 120nm deep and 60nm wide.	126
Figure 4-11: Demonstration of iteratively-trained RBF network performance. For a fixed trench width of 50nm, both network-predicted and actual outputs are plotted for various trench depths. The family of curves shows the accuracy of the RBF network compared to actual COMSOL results.....	127
Figure 4-12: Iterative signal inversion block diagram [31].....	128
Figure 4-13: Signal inversion routine convergence for 120nm×60nm trench with initial guess of 50nm×50nm for exact-trained ANN.	129
Figure 4-14: Signal inversion routine convergence for 120nm×60nm trench with initial guess of 50nm×50nm for iteratively-trained ANN.....	129
Figure 4-15: Signal inversion routine convergence for 100nm×80nm trench with initial guess of 200nm×200nm for exact-trained ANN.	130

Figure 4-16: Signal inversion routine convergence for 100nm×80nm trench with initial guess of 200nm×200nm for iteratively-trained ANN..... 130

List of Tables

Table 2-1: Key geometric dimensions for geometry #1.....	35
Table 2-2: Electrical parameters used in FEM simulation.....	36
Table 2-3: Key geometric dimensions for geometry #2.....	58
Table 2-4: Electrical parameters used in FEM simulation.....	59
Table 3-1: Key geometric dimensions for contaminated EUVL photomask simulation	78
Table 3-2: Electrical Parameters used in contaminated EUVL photomask simulation	78
Table 3-3: Key geometric dimensions for laboratory experiment.....	93
Table 4-1: Key geometric dimensions for trench simulations.....	117
Table 4-2: Electrical parameters used in FEM simulation.....	117

1 Introduction

This thesis is an investigation into the potential use of electroquasistatic (EQS) impedance sensors as an inspection and imaging tool for the integrated circuit industry. Large arrays of individually addressable EQS sensors could provide the integrated circuit industry with a new class of fast-scanning imaging tools to aid in the quality control of integrated circuits and photolithography equipment. This thesis launches an investigation into several different case studies that evaluate the sensitivity of EQS sensors in detecting both surface and subsurface features and contaminant objects that are typical to an integrated circuit. Both forward and inverse EQS problems are considered. Although this thesis focuses solely on EQS sensors, there exists an entire dual class of magnetoquasistatic (MQS) sensors. MQS sensors are particularly advantaged over EQS sensors when detecting features in highly conducting substrates due to the capabilities of magnetic fields to see beneath the surface of conductors at very low frequencies [1-5].

Current applications of both EQS and MQS sensors include, but are not limited to: detection of buried objects such as metallic and non-metallic landmines [1]; humidity and moisture sensing [3]; determining absolute electrical and magnetic properties and characterization of layered, heterogeneous materials [3, 4, 6]; measuring corrosion, aging, and cracking in structures [5, 7]; and proximity detection [8]. The electromagnetic operation of the sensors presented in this thesis is governed by the same fundamental set of equations as those described in the various applications above but provide new applications and methodologies for feature/defect detection and imaging.

1.1 Theory and Background of Electromagnetic Sensors

Given the breadth of applications in which electromagnetic sensors are used, it is appropriate to first describe their theory of operation at a fundamental level. The well-known and well-tested Maxwell's Equations that describe the coupling between electric and magnetic fields and their sources are listed in differential form:

$$\nabla \times \vec{E} = -\frac{\partial \vec{B}}{\partial t} \quad (1.1)$$

$$\nabla \times \vec{H} = \vec{j} + \frac{\partial \vec{D}}{\partial t} \quad (1.2)$$

$$\nabla \cdot \vec{D} = \rho_f \quad (1.3)$$

$$\nabla \cdot \vec{B} = 0 \quad (1.4)$$

$$\nabla \cdot \vec{j} + \frac{\partial \rho_f}{\partial t} = 0 \quad (1.5)$$

where \vec{E} is defined as the electric field vector in [V/m], \vec{H} the magnetic field intensity vector in [A/m], \vec{D} the electric displacement vector in [C/m²], and \vec{B} the magnetic flux density in [T]. The source terms \vec{j} and ρ_f represent the free current density in [A/m²] and the free volume charge density in [C/m³], respectively. Equation (1.5) is simply the source continuity equation. For linear, homogeneous media, these vector fields are related through the following set of constitutive relations:

$$\vec{D} = \epsilon \vec{E} \quad (1.6)$$

$$\vec{B} = \mu \vec{H} \quad (1.7)$$

$$\vec{j} = \sigma \vec{E} \quad (1.8)$$

where ϵ is the electrical permittivity of the medium, μ the magnetic permeability, and σ the electrical conductivity.

For problems in which sensor sizes are much smaller than the free space wavelength of electromagnetic waves that propagate at the sensors' operating frequency, Equations (1.1)—(1.5) can be decoupled and broken into two sets of approximate equations: electroquasistatics (EQS) and magnetoquasistatics (MQS). These equations are:

EQS		MQS	
$\nabla \times \vec{E} \approx 0$	(1.9)	$\nabla \times \vec{E} = -\frac{\partial \vec{B}}{\partial t}$	(1.12)
$\nabla \cdot \vec{D} = \rho_f$	(1.10)	$\nabla \times \vec{H} \approx \vec{j}$	(1.13)
$\nabla \cdot \vec{j} + \frac{\partial \rho_f}{\partial t} = 0$	(1.11)	$\nabla \cdot \vec{B} = 0$	(1.14)
		$\nabla \cdot \vec{j} \approx 0$	(1.15)

The EQS set of equations are used when the dominant sources are charges creating electric fields, while the MQS equations govern situations where the dominant sources are currents creating magnetic fields. In this quasistatic approximation, time-varying electric and magnetic fields no longer serve as source terms, and consequently, the equations do not describe the propagation of electromagnetic waves. This is appropriate as all electrically driven elements under consideration in a quasistatic regime are extremely poor at radiating electromagnetic waves.

The sensors described in this thesis are governed by the EQS set of equations; however, as stated previously, there also exists an entire class of analogous MQS-governed sensors useful for the detection of surface and subsurface features and objects. This thesis did not investigate the use of MQS sensors, because the original goal of this thesis was to detect features and objects that are

described electrically by their relative permittivity and electrical conductivity; moreover all materials considered in this thesis have relative permeability, $\mu_r = 1$. For a detailed description of the operation of MQS sensors and the duality between EQS and MQS sensors, sources [1-5, 7, 9] are suggested readings.

Because we treat the curl of the electric field as zero under the EQS approximation, we can write the electric field as the gradient of a scalar potential:

$$\vec{E} = -\nabla\Phi \quad (1.16)$$

By taking the divergence of the above equation and applying the constitutive relationship from Equation (1.6), one can see that the scalar potential obeys Poisson's Equation (1.17), and in source-free regions where $\rho_f = 0$, Equation (1.17) reduces to Laplace's Equation (1.18):

$$\begin{aligned} -\nabla \cdot \nabla\Phi &= \nabla \cdot \vec{E} \\ -\epsilon\nabla^2\Phi &= \nabla \cdot \vec{D} \\ \nabla^2\Phi &= -\frac{\rho_f}{\epsilon} \end{aligned} \quad (1.17)$$

$$\nabla^2\Phi = 0; \quad \rho_f = 0 \quad (1.18)$$

A consequence of Laplace's Equation for planar sensor arrays excited with a spatial periodicity is that solutions for the scalar potential Φ have evanescent fields that decay exponentially in the direction orthogonal to the sensor plane, even in the absence of a lossy medium. The range of these evanescent fields is proportional to the electrode size and spacing [3, 4]. Figure 1-1 illustrates an EQS sensor with sensitivity at multiple penetration depths [4].

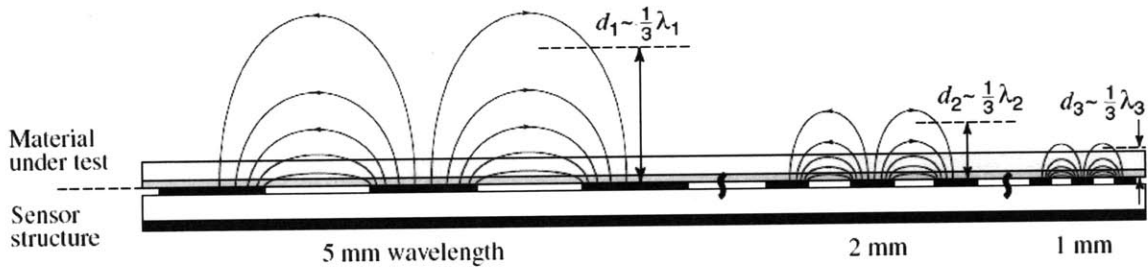


Figure 1-1: Multiple wavelength coplanar EQS sensor [4]. Such a sensor is useful for penetrating dielectric or poorly conducting substrates to multiple depths, providing both lateral and depth resolution.

Present generation quasistatic sensors utilize various coplanar electrode layouts to investigate materials at multiple depths of penetration. Electrodes are often interdigitated (EQS) or meandered (MQS) to achieve excitation patterns with desired periodic spatial wavelength(s) [1, 3-5, 10, 11]. Figure 1-2 shows a generic interdigital EQS sensor where one of the two interdigitated combs is driven by a source voltage, V_D , and the current on the other comb, I_S , is measured [4]. Such sensors are useful for the nondestructive testing and evaluation (NDT/NDE) of materials, as well as measuring absolute electrical properties [3, 11].

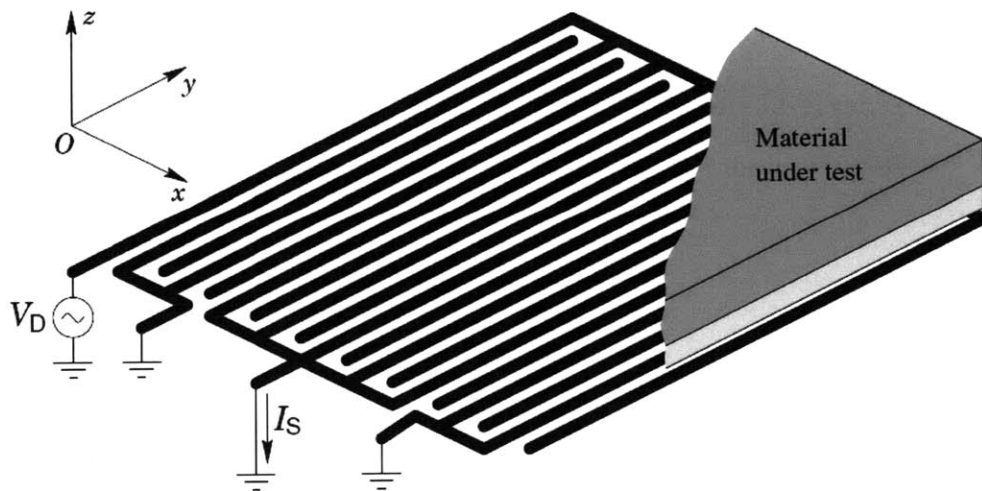


Figure 1-2: Generic interdigital EQS sensor [4].

EQS sensor electrodes are typically excited by a known, time-varying voltage with sensor currents measured to determine terminal impedances/admittances (alternatively, electrodes can be driven by a known current with terminal voltages measured). For a given position in space, the current-voltage relation on a sensor is a function of the local electrical properties (permittivity ϵ and conductivity σ) of the material(s) near the sensor.

Consider, for instance, the canonical parallel plate capacitor shown in Figure 1-3(a) with plate area, A , and spacing, d .

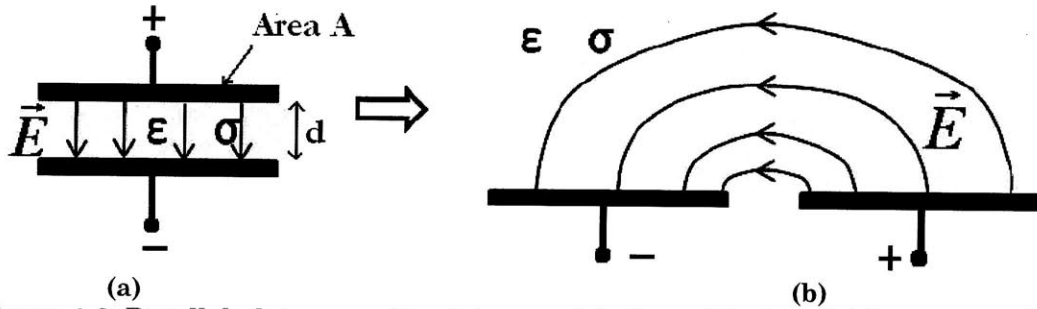


Figure 1-3: Parallel plate capacitor (a) opened to form fringing field capacitor (b).

Ignoring fringing field effects in this parallel-plate configuration, the complex terminal admittance, Y_{cap} , is determined by ϵ and σ between the two plates, where the capacitive susceptance goes as:

$$Imag\{Y_{cap}\} = \frac{\omega\epsilon A}{d} \quad (1.19)$$

and the conductance goes as:

$$Real\{Y_{cap}\} = \frac{\sigma A}{d} \quad (1.20)$$

By opening up the capacitor plates into a co-planar geometry, an intentional fringing field sensor is formed, where Y_{cap} is now a function of the material(s) surrounding the electrodes. The co-planar geometry is convenient when scanning sensors over a material under test at a fixed height. As driven electrodes are scanned over the surface of the material under test, terminal currents vary as local material properties change. Objects, features, and material interfaces can be detected by monitoring these variations in the sensors' currents.

This process is often described as solving the forward problem. Forward sensor problems are in general well-posed in that for a given geometry a unique sensor current response exists. The inverse problem is then to determine absolute material properties or absolute locations of features and objects from the sensor current response. These problems are in general ill-posed, as there does not necessarily exist a single unique solution for a given sensor current response [12]. An illustration of this forward/inverse problem cycle is provided in Figure 1-4.

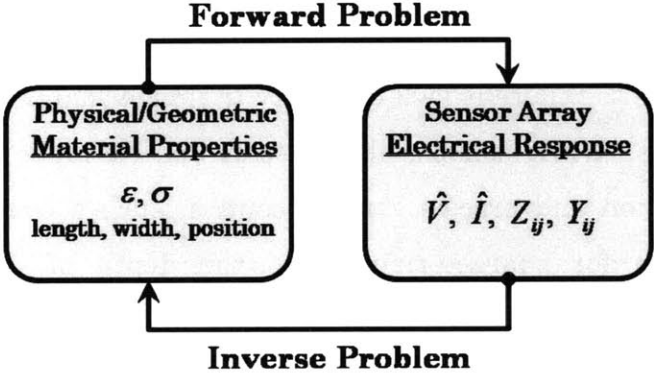


Figure 1-4: Forward/Inverse problem cycle.

1.2 Scanning Force Microscopy Methods

Scanning force microscopy (SFM) or atomic force microscopy (AFM) is one of the leading tools for imaging materials at the nanoscale. In general, SFM methods work by scanning (typically raster-scanning) a sharp probe tip over the surface of a

sample, and creating an image of that sample, where the contrast agent for the image comes from variations in a measurable force/interaction between the probe tip and the surface of the material [13-15]. In 1984, Matey and Blanc of RCA Laboratories invented scanning capacitive microscopy (SCM) where they utilized pre-developed instrumentation and pickup circuitry from the RCA CED VideoDisc player [14]. SCM is similar to AFM but specifically targets changes in the electrostatic capacitance between the probe tip and the surface. An image is created by monitoring local changes in capacitance between the probe tip and the sample or a conducting surface under the sample. The capacitance is a function of electrode and sample geometry, as well as the local permittivity of the sample.

While there have been many different approaches toward improving scanning probe microscopy methods—primarily with respect to probe shape, probe guarding, pickup circuitry, and image reconstruction—what has remained common amongst all of the groups attempting to develop high-resolution nanometer scale images via AFM/SCM methods is the use of a single sense electrode. A well known and well documented drawback of the single sense electrode (both guarded and unguarded implementations) is its inherent lack of ability to image/characterize the sample in all three dimensions. While it is possible to scan a single probe over a surface with high lateral resolution and precise vertical control, such a configuration does not provide information for characterizing into the depth of the material under evaluation. Consequently, AFM/SCM images are only capable of providing accurate maps of surface topology and near-surface material properties [13-15].

Another drawback of SCM is that it requires access to an electrical contact beneath the sample being imaged. EQS/MQS arrays are capable of imaging samples without making any direct electrical contact as they work by monitoring the fringing field effects between two or more sensors in the array and how they respond to changes in the sample's bulk electrical properties.

Large arrays of EQS/MQS electrodes could potentially provide an new class of inspection tools that can quickly scan nanoscale samples (photolithography equipment, ICs, biological samples, etc.) for features, defects, and contaminants at speeds far above the capabilities of current, single-probe technologies due to massive array parallelism. This thesis considers the ability of small arrays (less than ten electrodes) of EQS sensors to detect both surface and subsurface features and objects.

1.3 Thesis Overview

The aim of this thesis is to launch an investigation—solving both forward and inverse problems—into the potential use of EQS sensor arrays for nondestructive evaluation, imaging, and quality control purposes for integrated circuit industry applications. Research into three specific core areas will serve as the primary focus of the thesis:

- 1.) The use of EQS sensors to penetrate the surface of doped silicon and locate junctions
- 2.) The use of EQS sensors to locate and image sub-micron-scale surface features and contaminants
- 3.) An investigation into the inversion of sensor current response signals for determining exact feature dimensions and imaging purposes

In all cases sensors are coplanar and operate at a fixed height over the surface of the material under evaluation.

The first case study is presented in “Chapter 2: Subsurface Sensor Application: Locating a p-n Junction.” This case study serves as a primary investigation into a potentially new technology for mapping and imaging semiconductor devices. The results of this case study are intended to serve as a building block for future research into this new technology. The work comprising this chapter makes use of the commercially available finite element method (FEM)

software package COMSOL Multiphysics [16]. Simulations demonstrate how fringing fields from driven EQS sensors can couple into doped semiconducting substrates by operating sensors at a frequency comparable to the charge relaxation time of the silicon. It is demonstrated how p-n junctions in the substrate can be located by monitoring steady-state sensor currents for harmonic distortion.

The second area of focus is presented in “Chapter 3: Locating Surface Features and Contaminants.” This case study is an investigation into the use of EQS electrode arrays for quickly scanning surfaces for unwanted contaminant particles. One specific application that motivates research into this area is locating and removing contaminant particles on photomasks used in the mass production of integrated circuitry. Section 3.1 provides simulation results of the sensitivity of a EQS sensor array to various contaminant particles located in a gap in the absorber layer of an extreme ultraviolet lithography (EUVL) photomask. Section 3.2 presents the results of a macroscopic-scale laboratory experiment to confirm the results of Section 3.1. Laboratory experiments are performed where samples have similar aspect ratios and material properties to the simulated EUVL masks. Section 3.3 discusses the need for low-noise pickup circuitry for detecting sub-nano-amp variations in sensor currents as they scan past photomask contaminants and surface features.

These first two case studies deal solely with solving well-posed forward problems. The third core area presented in “Chapter 4: Sensor Signal Inversion through a Radial Basis Function Artificial Neural Network” provides one specific algorithm for solving an inverse problem for feature detection and imaging. In Chapter 4 a radial basis function artificial neural network (RBF-ANN) is trained to accurately predict the forward mapping of a feature’s physical dimensions into a sensor’s impedance response as it scans past the feature. The RBF-ANN is first trained with a small database of COMSOL simulation results to act as a forward function-approximation network. Once the RBF-ANN is trained, it is integrated

into an iterative signal inversion routine that can accurately predict a feature's dimensions when provided a sensor's impedance response and an initial guess.

Thesis results are summarized in “Chapter 5: Conclusions and Suggestions for Future Work.”

2 Subsurface Sensor Application: Locating a p-n Junction

This chapter describes how a p-n junction can be detected in a doped semiconductor substrate with an array of non-contact EQS sensors. This case study is a primary investigation into a new methodology for mapping and testing semiconductor devices. The results in this chapter are intended to serve as a building block for future investigation into this technology. Locating device junctions by coupling into them through an air gap could allow for new, fast scanning microscopy methods for IC imaging. IC imaging is useful for verification and detection of fabrication errors as well as detecting hidden Trojan circuits that might be present [17]

This chapter makes use of the commercially available COMSOL Multiphysics finite element method (FEM) simulation package [16]. Two different geometries are simulated in COMSOL to evaluate sensor performance. In both cases, sensors are driven with an AC voltage and held at a fixed height over the surface of a doped silicon substrate. Sensor currents are then measured and monitored for harmonic distortion caused by the junction's nonlinear drift-diffusion dynamics.

Results demonstrate how EQS sensors' fringing fields can couple into doped semiconducting substrates by operating sensors at a frequency comparable to the charge relaxation time of the silicon bulk. The frequency bandwidth over which these junctions are detectable is presented, illustrating both the capabilities and limitations of EQS sensors for such an application.

2.1 The p-n Junction Diode

The p-n junction is a fundamental component of many semiconductor devices including diodes, solar cells, and transistors. A p-n junction is the interface between a positively doped p-type region (where there exists a greater concentration of free holes than free electrons), and a negatively doped n-type region (where there exists a greater concentration of free electrons than free holes). The abrupt discontinuity in carrier concentrations that exists when the two regions meet forms a device with a nonlinear current-voltage relationship.

The two ways in which electrical current can flow in a semiconductor are due to carrier drift and carrier diffusion. Carrier drift exists due to the Coulombic force experienced by free charge carriers (electrons and holes) under the influence of an electric field, while carrier diffusion is the natural tendency for free carriers to flow along a concentration gradient in an attempt to equilibrate. The total current density for holes inside a semiconductor \vec{J}_p is simply the sum of these two currents:

$$\vec{J}_p = \vec{J}_{p,drift} + \vec{J}_{p,diffusion} \quad (2.1)$$

$$\vec{J}_p = q\mu_p p \vec{E} - qD_p \nabla p \quad (2.2)$$

and the total current density for electrons \vec{J}_n is:

$$\vec{J}_n = \vec{J}_{n,drift} + \vec{J}_{n,diffusion} \quad (2.3)$$

$$\vec{J}_n = q\mu_n n \vec{E} + qD_n \nabla n \quad (2.4)$$

where p and n are the concentrations of holes and electrons in [$1/\text{cm}^3$], μ_p and μ_n are the hole and electron mobilities in [$\text{cm}^2/\text{V}\cdot\text{s}$] (taken to be positive numbers), D_p and D_n are the hole and electron diffusivities in [cm^2/s], and q is the magnitude of charge of an electron ($1.602(10^{-19})[\text{C}]$), all satisfying the Einstein Relation:

$$\frac{D_p}{\mu_p} = \frac{D_n}{\mu_n} = \frac{kT}{q} \quad (2.5)$$

With \vec{J}_p and \vec{J}_n defined as such, the *total* free current density \vec{J} is then:

$$\vec{J} = \vec{J}_p + \vec{J}_n$$

$$\vec{J} = q(\mu_p p + \mu_n n)\vec{E} + q(-D_p \nabla p + D_n \nabla n) \quad (2.6)$$

When a p-n junction is formed, the steep gradients in carrier concentrations cause free hole and electrons to diffuse across the junction. Figure 2-1 (a)-(c) illustrates this. As a result, each region is no longer charge neutral and a space charge layer begins to form on each side of the junction (Figure 2-1(d)). This charge imbalance produces an electric field across the junction that acts to “push” holes and electrons—via carrier drift—back up the concentration gradient as seen in Figure 2-1 (e). This region of charge imbalance is known as the depletion region. Static equilibrium is achieved when carrier drift balances out carrier diffusion. Under static equilibrium, there then exists a built-in potential across the p-n junction even when the diode is unexcited by an external source shown in Figure 2-1 (f) [18].

When the diode is excited by an external voltage source, it is no longer under static equilibrium. Under forward bias—where the p-region potential is excited at a higher potential than the n-region—free holes in the p-region and free electrons in the n-region are pushed toward the depletion region. As the bias is increased, the depletion region narrows and the built-in electric field is unable to balance carrier diffusion across the junction; at a large enough forward biasing potential, diffusion then overcomes drift and the diode can conduct significant current. Under reverse biasing conditions, where the p-region potential is excited at a lower potential than the n-region, free holes in the p-region and free electrons in the n-region are now

pulled away from the depletion region. Consequently, the diode fails to conduct a significant current across the junction (unless the potential is increased to such a high level that the diode breaks down [18]). Since the diode conducts differently under forward and reverse bias, it forms a device with a nonlinear current—voltage relationship. For a more detailed explanation on p-n junction physics, the sources [18, 19] are suggested readings.

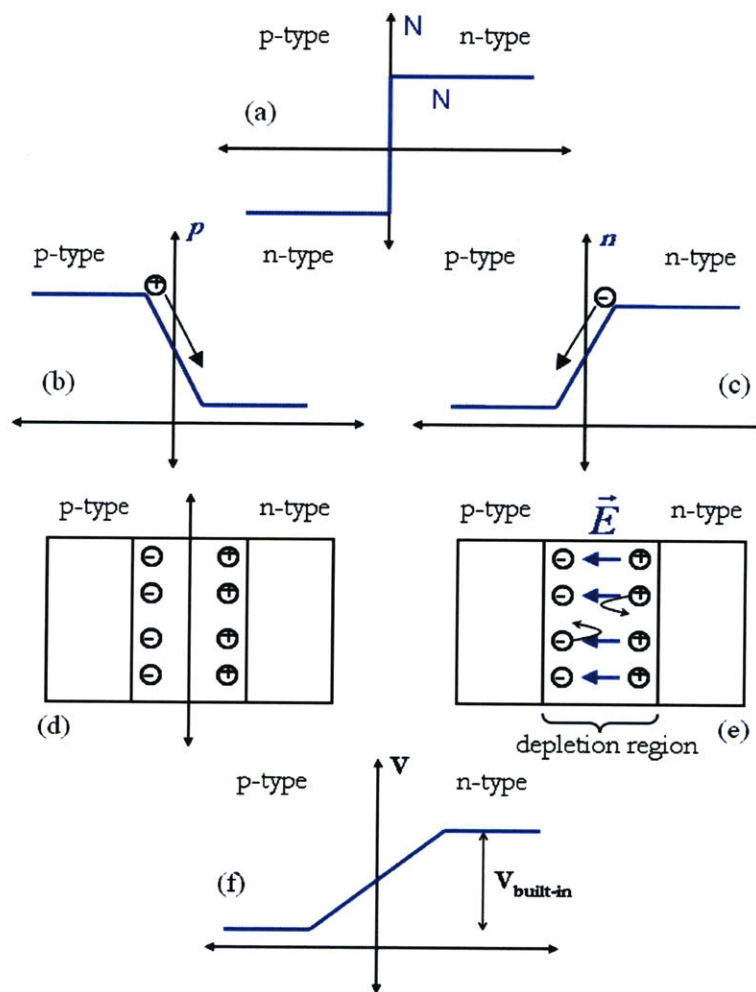


Figure 2-1: p-n Junction under static equilibrium.

2.2 Coupling into a p-n Junction Diode through an Air Gap

A p-n diode can be repeatedly turned on and off by applying a sinusoidal voltage to a terminal pair that is electrically connected to the diode's two differently doped regions. This creates a terminal current that is inherently nonlinear. If we look at the frequency spectrum of this diode current, we would see that there exist contributions to the total current at integer multiples of the fundamental drive frequency. We say that the diode current then experiences a harmonic distortion where this harmonic distortion is solely due to the nonlinear drift-diffusion barrier between the p-type and n-type regions described in the previous section.

The challenge of this chapter is to determine if p-n junctions can be coupled into and turned on and off by driven EQS electrodes *without* making any direct electrical contact to either of the p-type or n-type regions. One can imagine scanning an array of two (or more) voltage driven EQS electrodes at a fixed height over the surface of a semiconductor that has doped into it several p-type and n-type regions that form nonlinear drift-diffusion barriers at each of their interfaces. If these electrodes are positioned so that they are not over the top of any junctions—for instance they might be over top of a large p-type bulk region with no n-type wells doped into it—then the current on these sensors will be linear and experience no harmonic distortion whatsoever. However, if two of these sensors are located over the top of a p-n junction, then they might manage to couple into that junction, repeatedly turning it on and off over time causing harmonic distortion in the sensor currents. One can then imagine scanning a massive array of these electrodes over the surface of a semiconductor and monitoring the individual sensor currents for harmonic distortion. This concept could then provide a new, fast-scanning method for mapping and imaging the semiconducting layers of an integrated circuit, where doped wells and junctions are located by looking for these higher harmonics in the sensors' current responses.

Two different geometries were simulated in COMSOL to investigate the ability and sensitivity of EQS sensors in locating a p-n junction. The setup and the results of each of these two case studies are summarized in Sections 2.3—2.6.

2.3 FEM Model #1 Setup

2.3.1 Geometric Properties

A geometry was drawn in COMSOL to represent a silicon p-n junction diode with an air-filled region interfacing one of the diode's sides. The simulation was performed using two-dimensional solvers for simplicity, so all results presented in this chapter are in per-unit-depth format. This first geometry under evaluation is shown in Figure 2-2 with important geometric dimensions listed in Table 2-1.

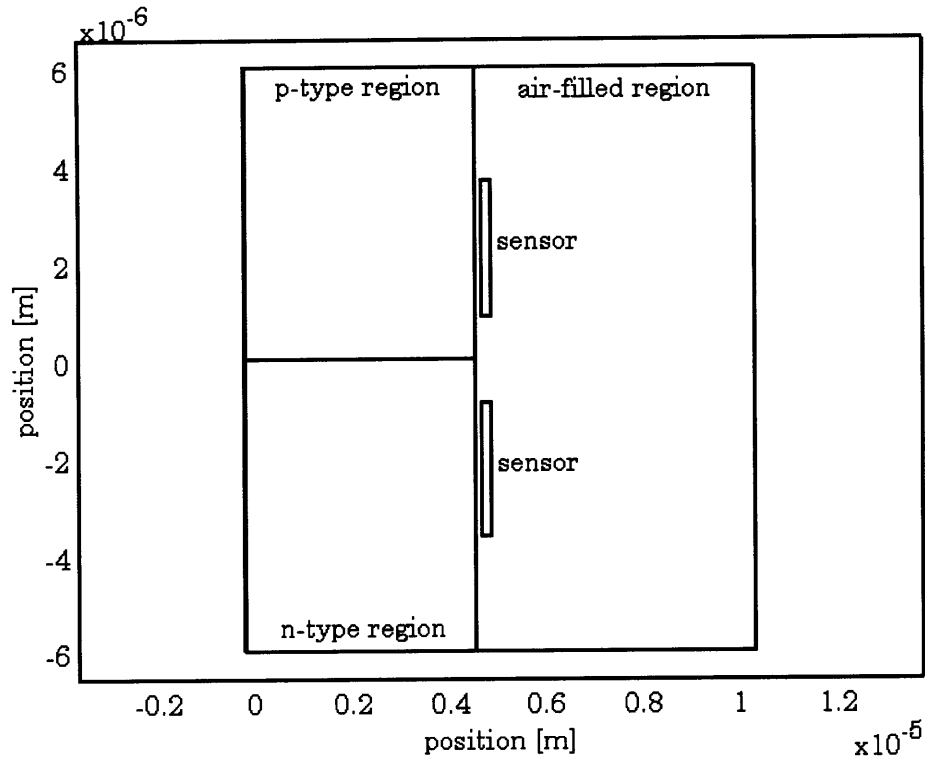


Figure 2-2: COMSOL geometry #1 to be analyzed.

Table 2-1: Key geometric dimensions for geometry #1

Dimension	Length [μm]
silicon region horizontal dimension	5
air-filled region horizontal dimension	6
p-type region vertical dimension	6
n-type region vertical dimension	6
sensor horizontal dimension	0.2
sensor vertical dimension	2.75
sensor-silicon air gap	0.1
sensor-sensor inner edge-to-edge spacing	1.8

2.3.2 Physical Properties

The silicon region was doped to represent a p-n junction at the interface shown in Figure 2-2. In the interest of achieving numerical convergence in COMSOL, an abrupt, discontinuous “step-junction” was not specified; rather, the dopant concentration function, N , was described using a Gaussian function with a very steep drop-off constant, c_d :

$$N = \begin{cases} 2N_{Dnmax}e^{-\left(\frac{y-y_1}{c_d}\right)^2} - N_{Apmax}, & y > y_1 \\ N_{Dnmax}, & y \leq y_1 \end{cases} \quad (2.7)$$

where N_{Dnmax} is the maximum donor (n-type) doping concentration and N_{Apmax} is the maximum acceptor (p-type) doping concentration. A negative value for N indicates a doping of acceptor atoms, while a positive value indicates a doping of donor atoms. By specifying the dopant concentrations in this manner, a p-n step junction is created with a smooth but still steep concentration function rather than a sharp, discontinuous function over several orders of magnitude (N changes on the order of 10^{22} [1/m³] across the junction).

The relevant physical parameter values assigned to the silicon region are listed in Table 2-2.

Table 2-2: Electrical parameters used in FEM simulation

Parameter	Value	Units
N_{Dnmax} : maximum n-type doping	10^{16}	[1/cm ³]
N_{Apmax} : maximum p-type doping	10^{16}	[1/cm ³]
n_i : intrinsic impurity concentration for Si	$1.46(10^{10})$	[1/cm ³]
μ_p : hole mobility	400	[cm ² /Vs]
μ_n : electron mobility	800	[cm ² /Vs]

D_p : hole diffusivity	10.34	[cm ² /s]
D_n : electron diffusivity	20.67	[cm ² /s]
k : Boltzmann's constant	1.38(10 ⁻²³)	[J/K]
T : temperature	300	[K]
q : elementary electric charge	1.602(10 ⁻¹⁹)	[C]
ϵ_r : Si relative permittivity	11.8	--
c_d : doping fall-off constant	0.329	[μ m]
y_1 : doping fall-off position	-0.3	[μ m]

2.3.3 Solver Properties

The semiconductor problem was solved by coupling together two COMSOL Multiphysics modules: an electrostatics module to solve Poisson's Equation (Equation (1.17)) for the electric scalar potential and a convection and diffusion module to describe the drift-diffusion carrier dynamics through a source continuity equation. Hole and electron flows are described with separate modules where the flow of holes is described with the following differential equation:

$$\frac{\partial p}{\partial t} + \nabla \cdot (-D_p \nabla p - \mu_p p \nabla \Phi) = R_p - G_p \quad (2.8)$$

and the flow of electrons satisfies the following differential equation:

$$\frac{\partial n}{\partial t} + \nabla \cdot (-D_n \nabla n + \mu_n n \nabla \Phi) = R_n - G_n \quad (2.9)$$

where R and G are the recombination and generation terms, respectively. For this analysis R and G can be set to zero—as there is no recombination/generation in the

bulk or depletion regions—and equations (2.8)—(2.9) then reduce to Equation (1.11). These drift/diffusion solvers for p and n are coupled to the Poisson's Equation solver through the free space charge density ρ_f :

$$\rho_f = q(N - n + p) \quad (2.10)$$

In a uniformly doped semiconductor region, the net charge in that region is zero and Equation (2.10) reduces to:

$$(N - n + p) = 0 \quad (2.11)$$

Additionally, n and p are related through the np product:

$$np = n_i^2 \quad (2.12)$$

where n_i^2 is the intrinsic impurity concentration. Equations (2.11) and (2.12) provide two equations and two unknowns. Solving these two equations allows us to provide the solver with an initial equilibrium value on p and n in the silicon region:

$$p_{init} = \begin{cases} \frac{|N|}{2} + \sqrt{\left(\frac{N}{2}\right)^2 + n_i^2}, & N < 0 \\ \frac{n_i^2}{\frac{|N|}{2} + \sqrt{\left(\frac{N}{2}\right)^2 + n_i^2}}, & N \geq 0 \end{cases} \quad (2.13)$$

$$n_{init} = \begin{cases} \frac{|N|}{2} + \sqrt{\left(\frac{N}{2}\right)^2 + n_i^2}, & N \geq 0 \\ \frac{n_i^2}{\frac{|N|}{2} + \sqrt{\left(\frac{N}{2}\right)^2 + n_i^2}}, & N < 0 \end{cases} \quad (2.14)$$

The initial, static equilibrium value for the built in potential in the semiconductor region is:

$$\phi_{init} = \begin{cases} -\frac{kT}{q} \ln\left(\frac{p_{init}}{n_i}\right), & N < 0 \\ \frac{kT}{q} \ln\left(\frac{n_{init}}{n_i}\right), & N \geq 0 \end{cases} \quad (2.15)$$

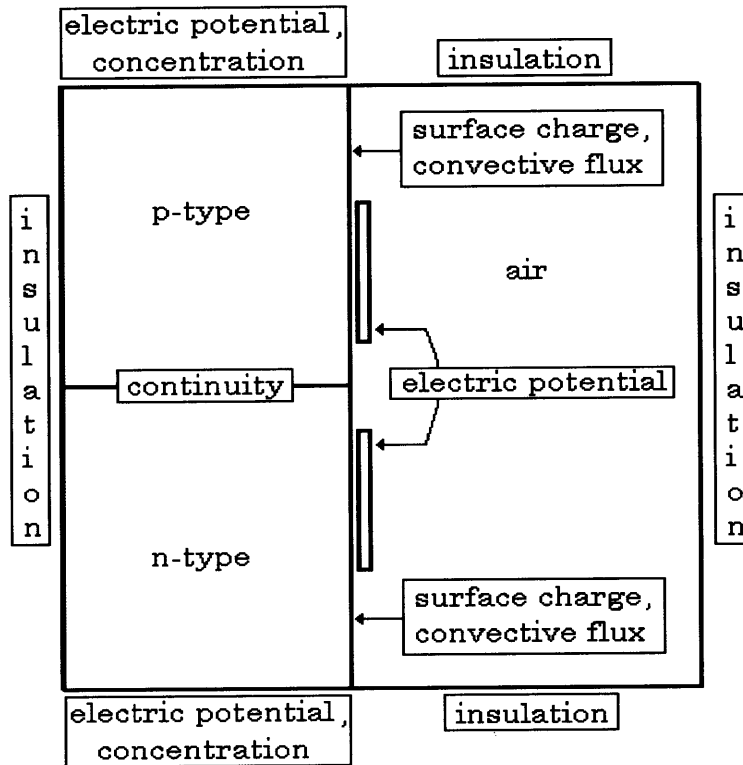


Figure 2-3: Boundary conditions for COMSOL geometry #1.

The boundary conditions for both the electrostatics module and the convection and diffusion modules are shown in Figure 2-3. The insulation boundary conditions truncate the solution space by forcing the normal component of \vec{D} and \vec{j} to be zero. The boundary conditions at the top of the p-type region and the bottom of the n-type region force the electric potential and hole and electron concentrations to their initial values ϕ_{init} , p_{init} , and n_{init} , respectively. These boundaries represent

un-driven electrical contacts. The continuity boundary condition that divides the p-type and n-type regions exists solely for the purpose of mesh refinement near the active depletion region and adds no additional constraints to the solution. The electric potential boundary conditions on the EQS sensors allow us to impose a known AC voltage onto each of the sensors. Since the silicon region has a different permittivity and conductivity than that of the air-filled region, the normal component of the electric displacement vector \vec{D} is discontinuous, and the relevant boundary condition is a surface charge boundary condition:

$$\hat{n} \cdot (\vec{D}_{air} - \vec{D}_{Si}) = \rho_s \quad (2.16)$$

where \hat{n} points from the silicon region into the air-filled region. Since ρ_s is not known beforehand and is time-varying, the source continuity boundary condition

$$\hat{n} \cdot (\vec{J}_{air} - \vec{J}_{Si}) = -\frac{\partial \rho_s}{\partial t} \quad (2.17)$$

is solved simultaneously. Since carriers cannot diffuse across the silicon-air interface, it is also necessary to apply COMSOL's "convective flux only" boundary conditions to the convection and diffusion solvers.

Additional details regarding the COMSOL model properties and solver settings for FEM Model #1 can be found in Appendix B.

2.4 FEM Model #1 Simulation Results

This section provides the results of several COMSOL simulations that were run with the parameters and settings from Section 2.3. Figure 2-4, Figure 2-5, and Figure 2-6 show the initial values for the carrier concentrations p and n , space charge density ρ_s , and electric potential Φ , respectively. These figures match the

description of p-n junction behavior under static equilibrium from Section 2.1. Figure 2-4 illustrates the sharp roll-off in the hole concentration from the p-type region into the n-type region and the same behavior for electrons from the n-type region into the p-type region. Figure 2-5 shows the space charge layers that are formed on each side of the junction, and Figure 2-6 shows the resulting built-in potential to be approximately 0.694V across the junction. This makes sense, because the theoretical built-in potential for an abrupt p-n step junction is [18]:

$$V_{bi} = \frac{kT}{q} \ln \left(\frac{n_n p_p}{n_i^2} \right) = 0.695 \text{ [V]} \quad (2.18)$$

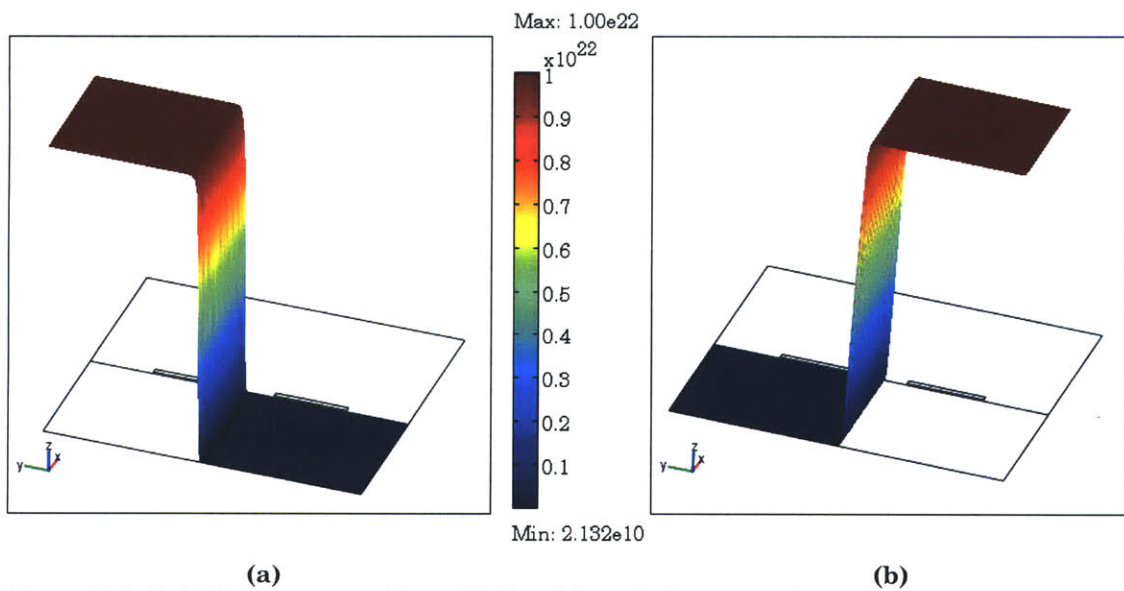


Figure 2-4: Initial Concentration of holes (a) and electrons (b) in $[1/m^3]$ shown as a 3-D colormapped surface plot.

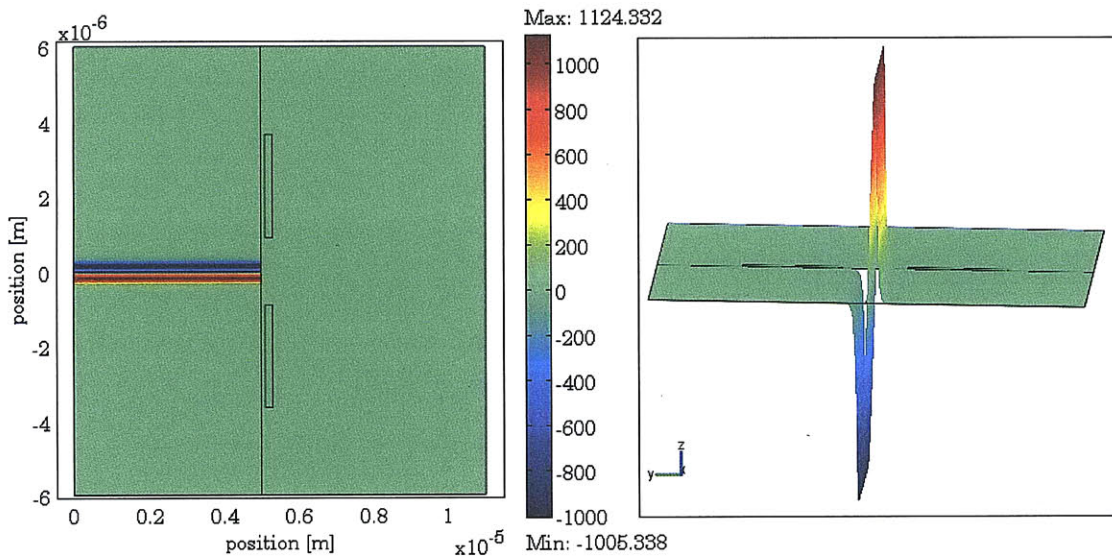


Figure 2-5: Initial space charge density [C/m³] shown as both a 2-D and 3-D colormapped surface plot.

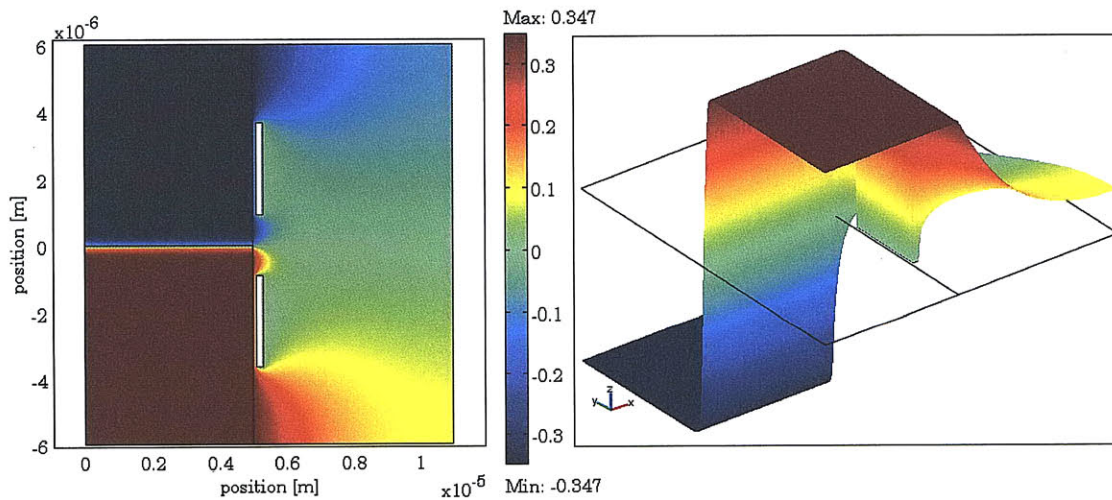


Figure 2-6: Initial scalar potential [V] shown as both a 2-D and 3-D colormapped surface plot.

The sensors were driven by an AC voltage, and the resulting current on the upper electrode was measured. The current was measured by integrating the surface charge density on the electrode's surface to get the total charge on the electrode Q_{sensor} and then taking the time derivative of the total charge:

$$i_{sensor} = \frac{\partial Q_{sensor}}{\partial t} \quad (2.19)$$

To simulate guarding—and to increase the sensitivity of the current response to the semiconductor region—only a portion of the sensor’s surface was integrated. Figure 2-7 shows the integration path that was chosen along the upper sensor. Figure 2-8 shows a sensor drive scheme, with individual guard electrodes shown, that motivates this integration path approximation. The integration path on the upper electrode in Figure 2-7 represents the upper sense electrode in Figure 2-8, while the rest of the upper electrode in Figure 2-7 represents the two surrounding guards for the upper electrode in Figure 2-8. With such a configuration, guard electrodes shunt the fields from the sense electrodes toward the silicon bulk, thus increasing sensitivity.

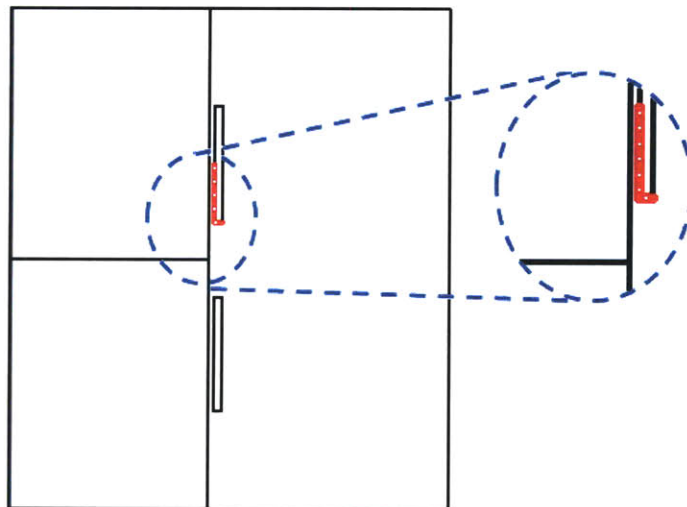


Figure 2-7: Integration path (shown in red) for surface charge density integration to simulate guarded electrodes in Figure 2-8.

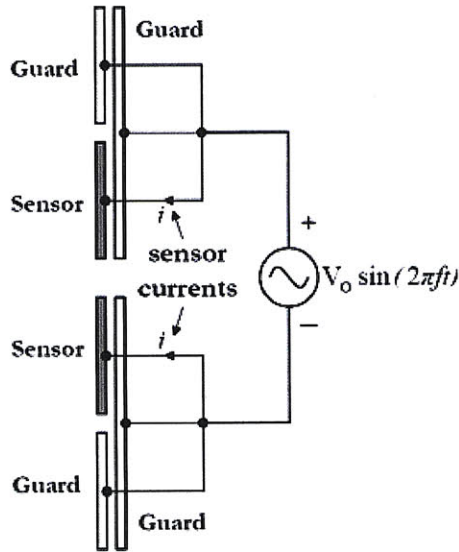


Figure 2-8: Sensor drive scheme with individual guard electrodes shown.

2.4.1 Charge Relaxation

In order for a significant portion of the sensors' fields to penetrate the semiconducting bulk, the AC excitation frequency must be on the order of the charge relaxation break frequency of the material, f_{break} , where:

$$f_{break} = \frac{\sigma}{2\pi\epsilon} \quad (2.20)$$

For frequencies much lower than f_{break} , the region appears as a conductor to the sensors because free charge in the bulk has ample time to migrate to the surface and terminate the electric field as a surface charge. On the other hand, for frequencies much higher than f_{break} , the region appears as an insulator because the fields alternate far too quickly for a significant amount of free bulk charge to migrate to the surface. For a homogeneous semiconductor:

$$\sigma = q(\mu_n n + \mu_p p) \quad (2.21)$$

so the conductivities of the p-region and n-regions will vary due to the difference in hole and electron mobilities (listed in Table 2-1):

$$\sigma_{p,region} \approx 64 \left[\frac{S}{m} \right] \quad ; \quad \sigma_{n,region} \approx 128 \left[\frac{S}{m} \right]$$

The charge relaxation break frequencies are then:

$$f_{break,p} \approx 97.5GHz \quad ; \quad f_{break,n} \approx 195GHz$$

In order to get deep penetration of fields into the silicon region, it is then desirable to operate the sensors at a frequency comparable to f_{break} .

2.4.2 Results

Simulations were run at 1GHz, 5GHz, 10GHz, 50GHz, and 100GHz with the upper and lower sensors excited as follows:

$$V_{upper} = 15 \sin(2\pi ft) \text{ [V]} \quad (2.22)$$

$$V_{lower} = -15 \sin(2\pi ft) \text{ [V]} \quad (2.23)$$

For each of these cases, the upper sensor current was measured using the integration path shown in Figure 2-7. A Fast Fourier Transform (FFT) was performed to determine if the junction's nonlinear dynamics were reflected in the sensor current's frequency spectrum. Figure 2-9 – Figure 2-14 show the results of the FFT for each of the five different fundamental operating frequencies.

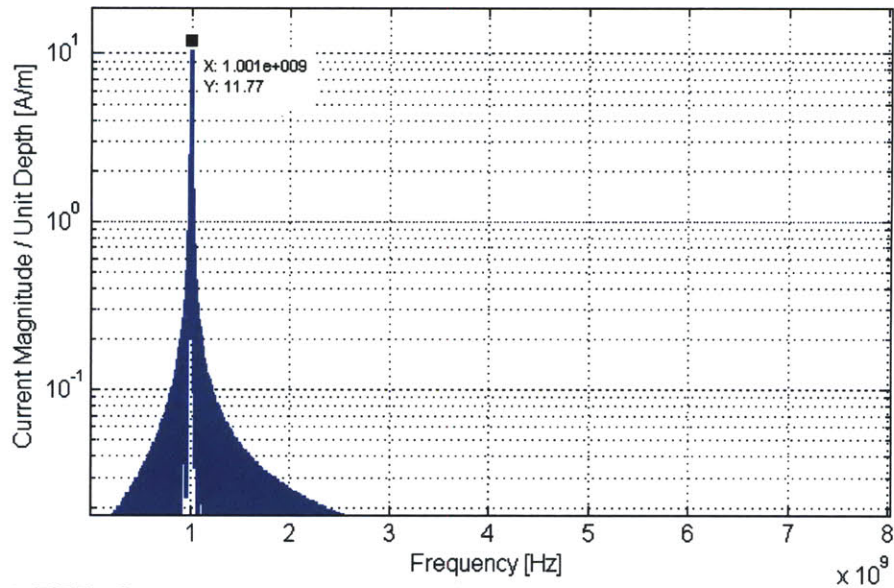


Figure 2-9: FFT of sensor current magnitude per unit depth [A/m] at 1GHz fundamental drive. In this lower frequency limit, no harmonic distortion is witnessed in the sensor current.

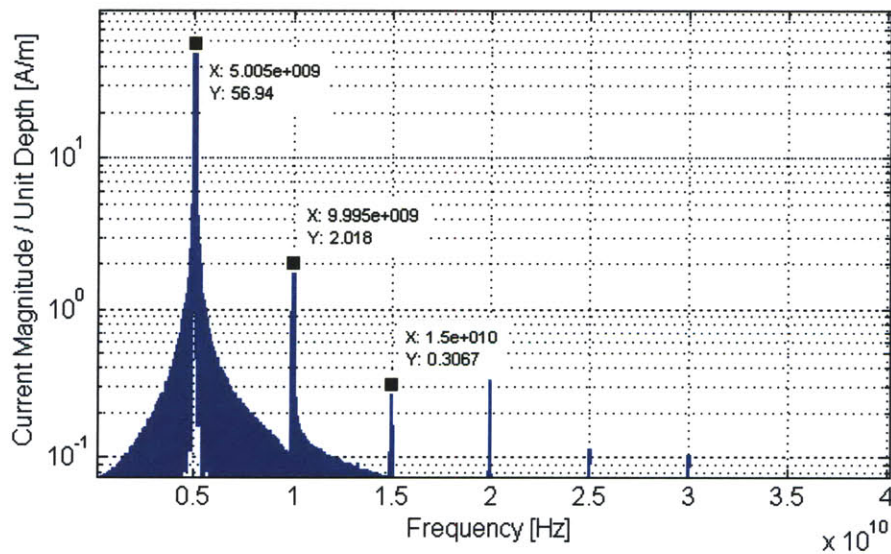


Figure 2-10: FFT of sensor current magnitude per unit depth [A/m] at 5GHz fundamental drive. Harmonic distortion begins to show up in the sensor current.

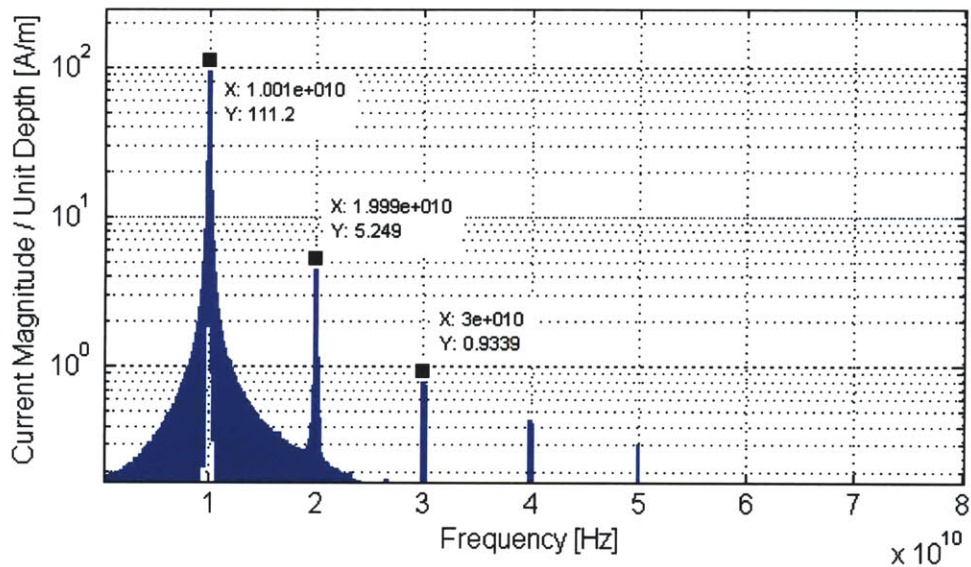


Figure 2-11: FFT of sensor current magnitude per unit depth [A/m] at 10GHz fundamental drive.

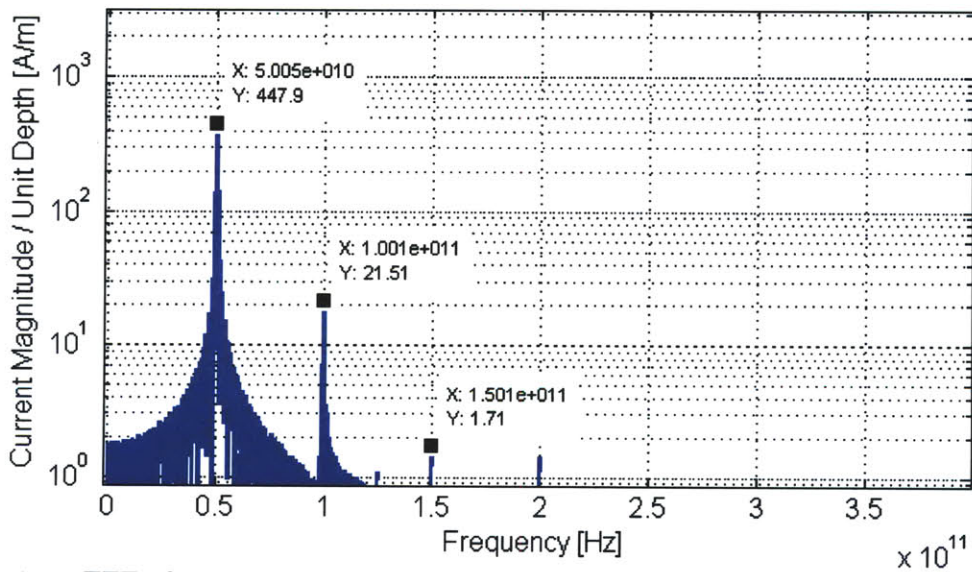


Figure 2-12: FFT of sensor current magnitude per unit depth [A/m] at 50GHz fundamental drive.

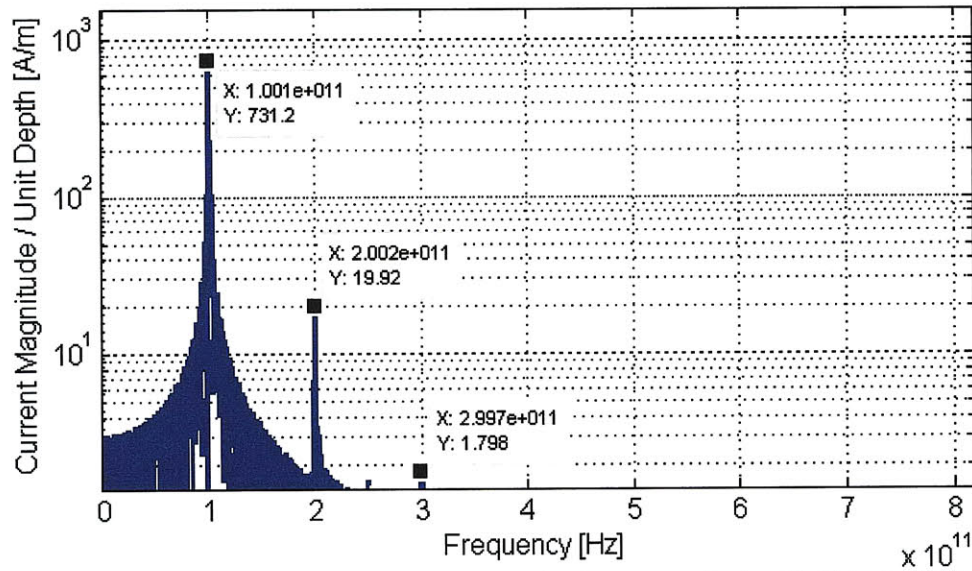


Figure 2-13: FFT of sensor current magnitude per unit depth [A/m] at 100GHz fundamental drive.

These results can be summarized and compared by examining the ratio of the second harmonic component of the current to the first harmonic component (as shown in Figure 2-14).

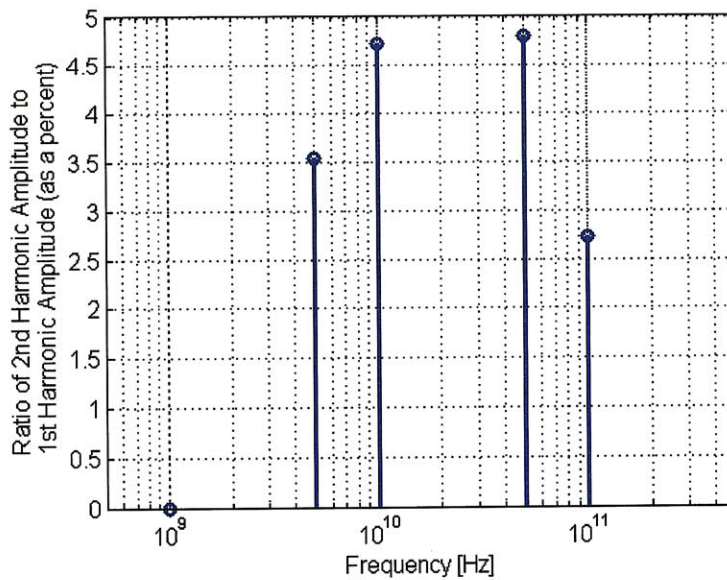


Figure 2-14: Ratio of 2nd harmonic amplitude to 1st harmonic amplitude (expressed as a percentage) vs. fundamental drive frequency [Hz].

In the low frequency limit (1GHz), it is clear that the p-n junction cannot be detected. The FFT in Figure 2-9 fails to show any noticeable harmonic distortion to the sensor current. As stated previously, this is most likely due to the fact that the excitation frequency is too low compared to the charge relaxation break frequency of the silicon regions. For visual confirmation that this is the case, Figure 2-15 shows a colormapped surface plot of the scalar potential at time $t = \frac{T}{10}$ where T is the excitation period [10^{-9} s]. The scale of the colormapped surface plot is truncated to $-2V \leq \Phi \leq 2V$. This is done to highlight variations in the semiconductor where the potential varies less than in the air-filled region. At 1GHz, there exists only a weak and shallow gradient in scalar potential in the semiconducting region due to the sensors; consequently, the sensors are only capable of turning the diode on and off at a very shallow depth. Moreover, a majority of the junction remains in its static equilibrium state, and the sensor current is heavily dominated by the linear air gap capacitance.

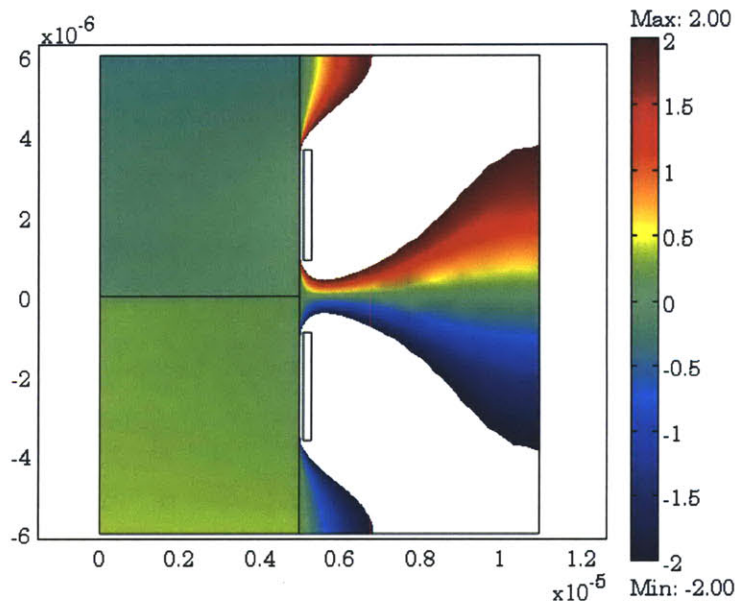
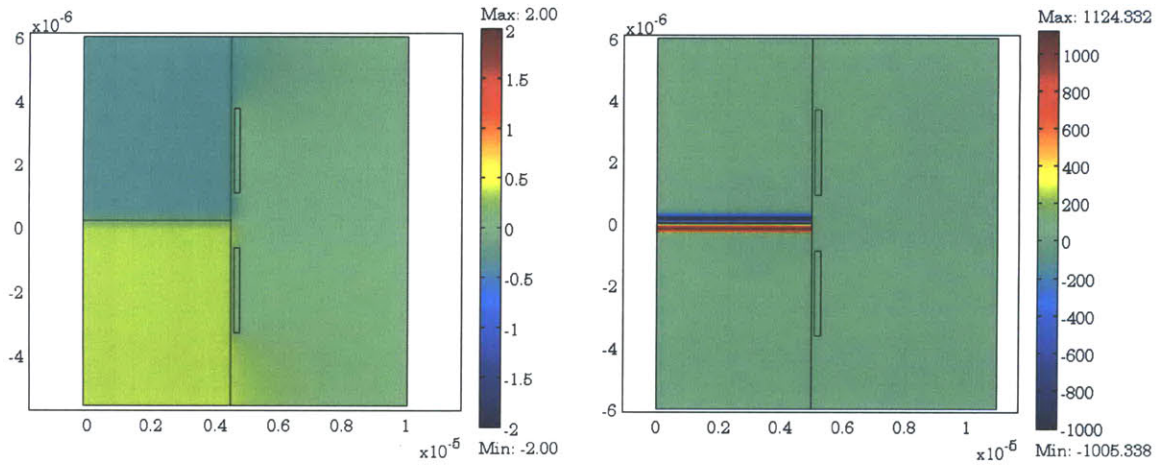


Figure 2-15: Scalar potential [V] at $t=T/10$ for 1GHz drive.

As the excitation frequency is raised, harmonic distortion begins to show up in the sensor current. Figure 2-14 shows approximately a 21:1 ratio in the first to

second harmonic components of the sensor current at 10GHz. Colormapped surface plots of the scalar potential and space charge density for the 10GHz excitation are provided in Figure 2-16 for several times during the first excitation period. These snapshots in time are taken every $\frac{T}{10}$ seconds for the first full excitation period. At time $t = 0$, the system is under static equilibrium. At $t = \frac{T}{10}$ there exists a large forward bias across the junction and the space charge layer begins to thin out as the diode conducts current. The imbalance in penetration depths between the p-type and n-type regions is due to the difference in conductivities (Equation (2.21)). At $t = 2\frac{T}{10}$, the sensor excitation is still on its rising edge, but free charge in the semiconducting bulk begins to resist field penetration. By $t = 4\frac{T}{10}$ a significant amount of image charges have migrated to the silicon-air interface to terminate the electric fields, forming an air-gap capacitor. It can be seen that the diode is entering a reverse bias while the sensors are still forward biased. By $t = 5\frac{T}{10}$ the space charge layer has begun to grow as the diode is increasingly reverse biased. At this point the sensors are halfway through one period and the phase difference between the sensor excitation and the semiconductor dynamics is obvious. By $t = 9\frac{T}{10}$, image charges in the bulk have caught up with the sensors to again form an air-gap capacitor as was the case at time $t = 4\frac{T}{10}$, and the space charge layer begins to diminish as the diode enters forward bias. At $t = T$ the simulation has completed one full period and the junction is forward biased.

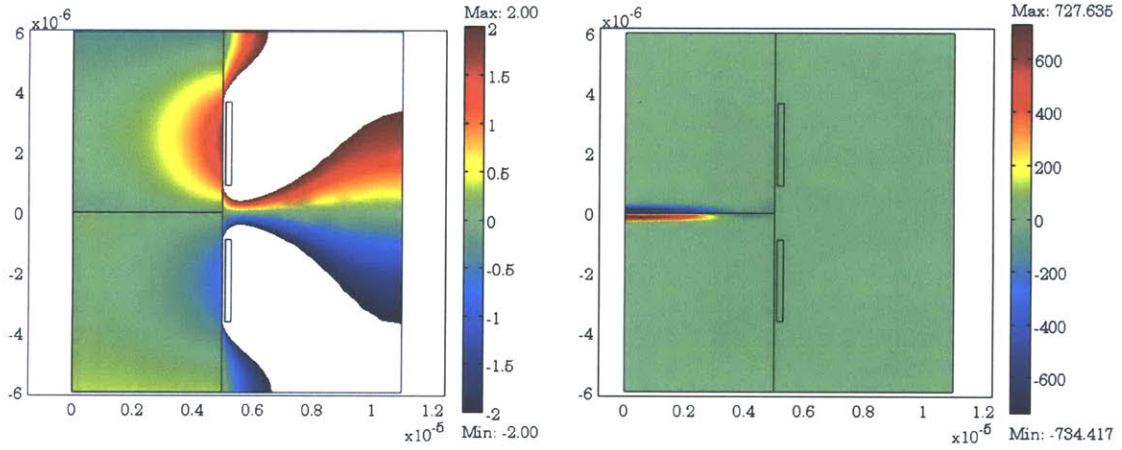
When taking the FFT of the sensor current's steady state response, it is important to ignore this first transient period and to only consider the sensor current once it has reached sinusoidal steady state.



(a0) Potential [V]

$t = 0$

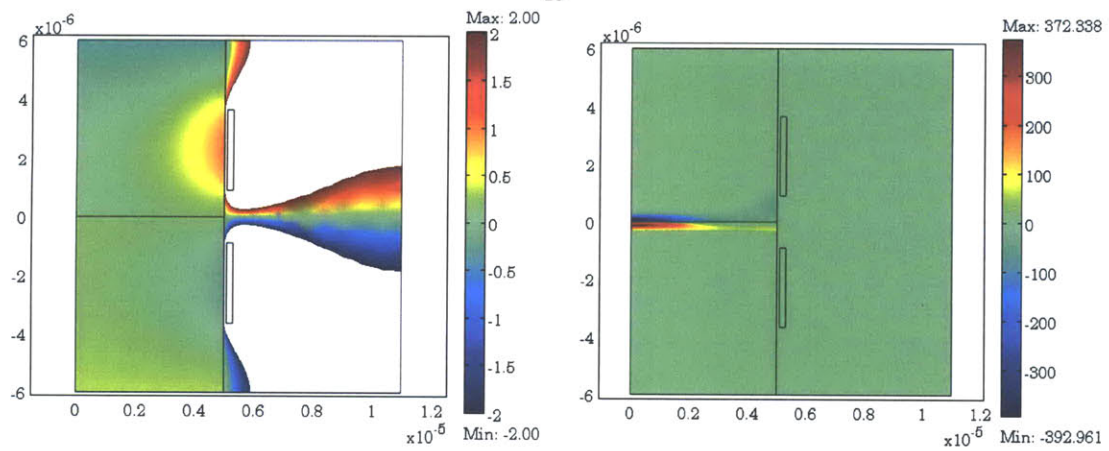
(b0) Charge Density [C/m³]



(a1) Potential [V]

$t = \frac{T}{10}$

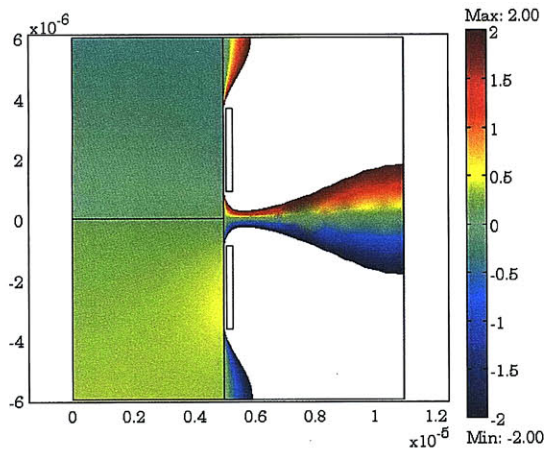
(b1) Charge Density [C/m³]



(a2) Potential [V]

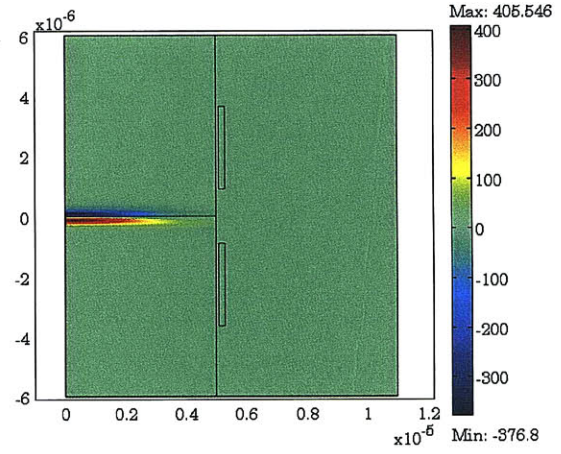
$t = 2 \frac{T}{10}$

(b2) Charge Density [C/m³]

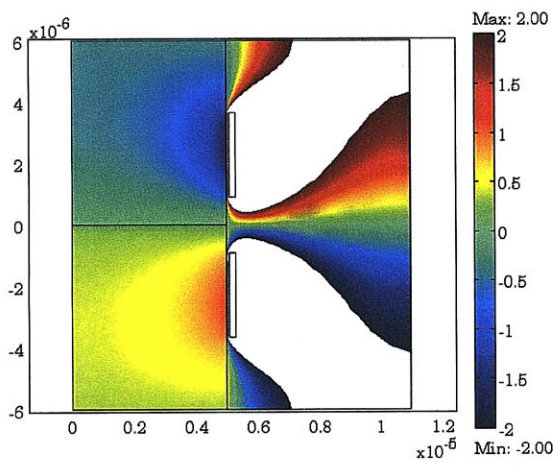


(a3) Potential [V]

$t = 3 \frac{T}{10}$

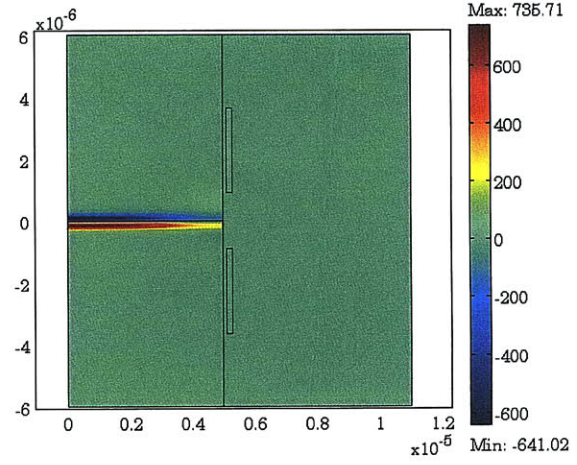


(b3) Charge Density [C/m³]

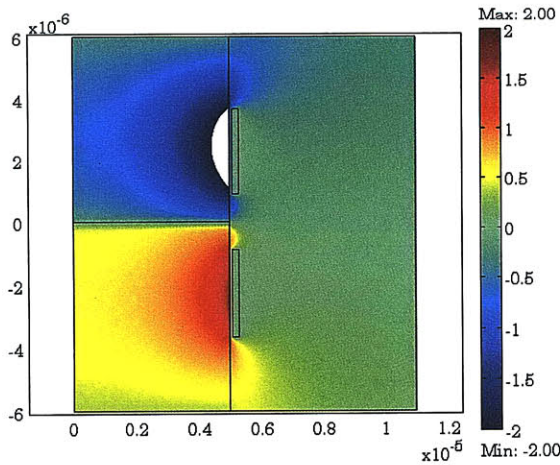


(a4) Potential [V]

$t = 4 \frac{T}{10}$

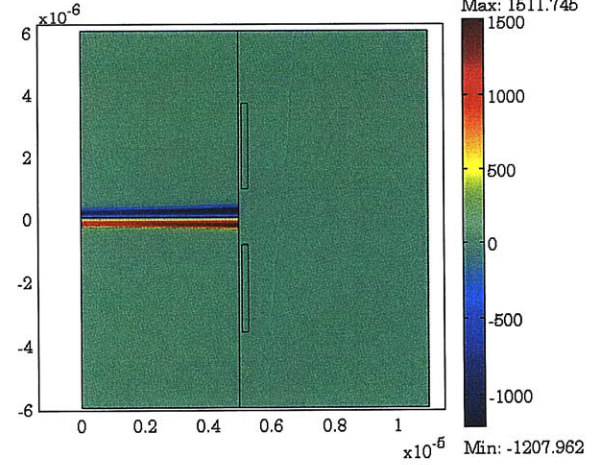


(b4) Charge Density [C/m³]

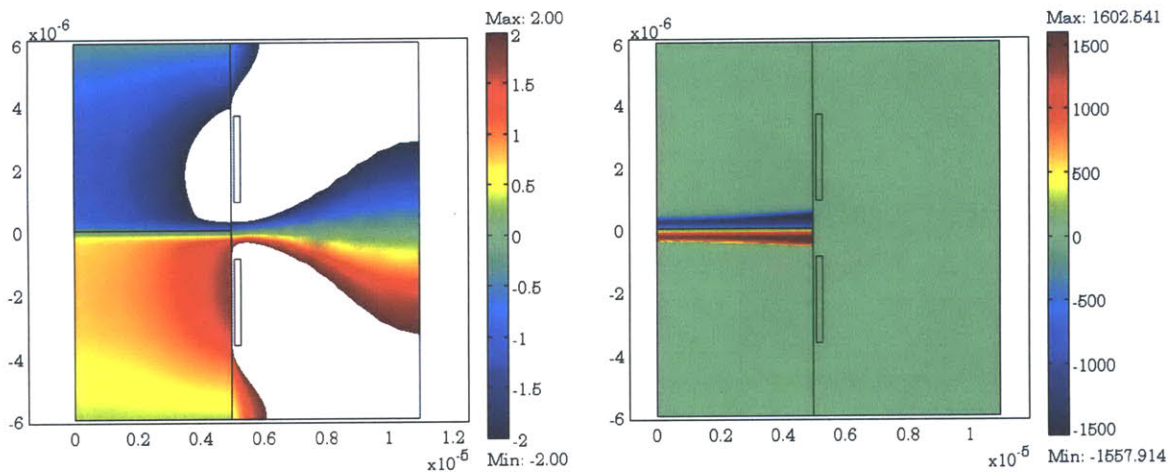


(a5) Potential [V]

$t = 5 \frac{T}{10}$



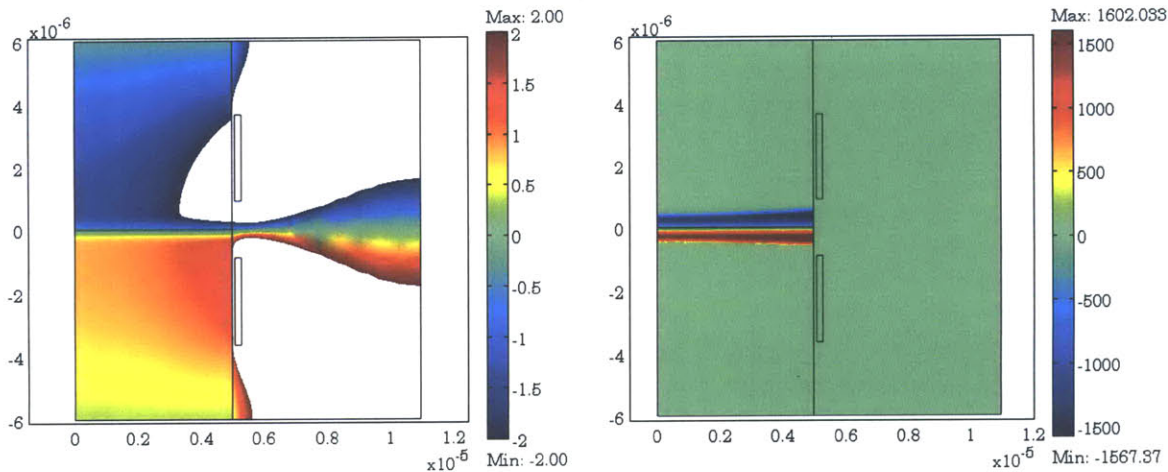
(b5) Charge Density [C/m³]



(a6) Potential [V]

$$t = 6 \frac{T}{10}$$

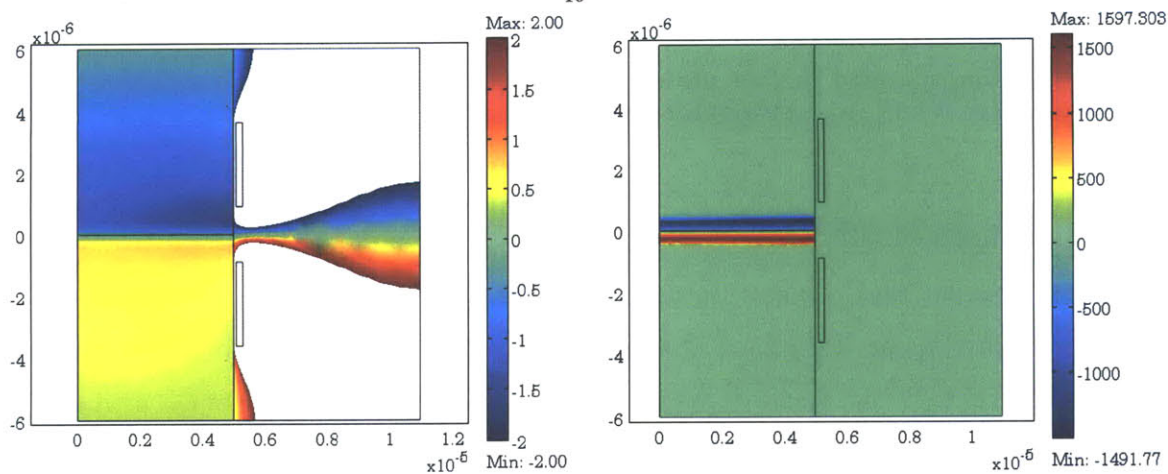
(b6) Charge Density [C/m³]



(a7) Potential [V]

$$t = 7 \frac{T}{10}$$

(b7) Charge Density [C/m³]



(a8) Potential [V]

$$t = 8 \frac{T}{10}$$

(b8) Charge Density [C/m³]

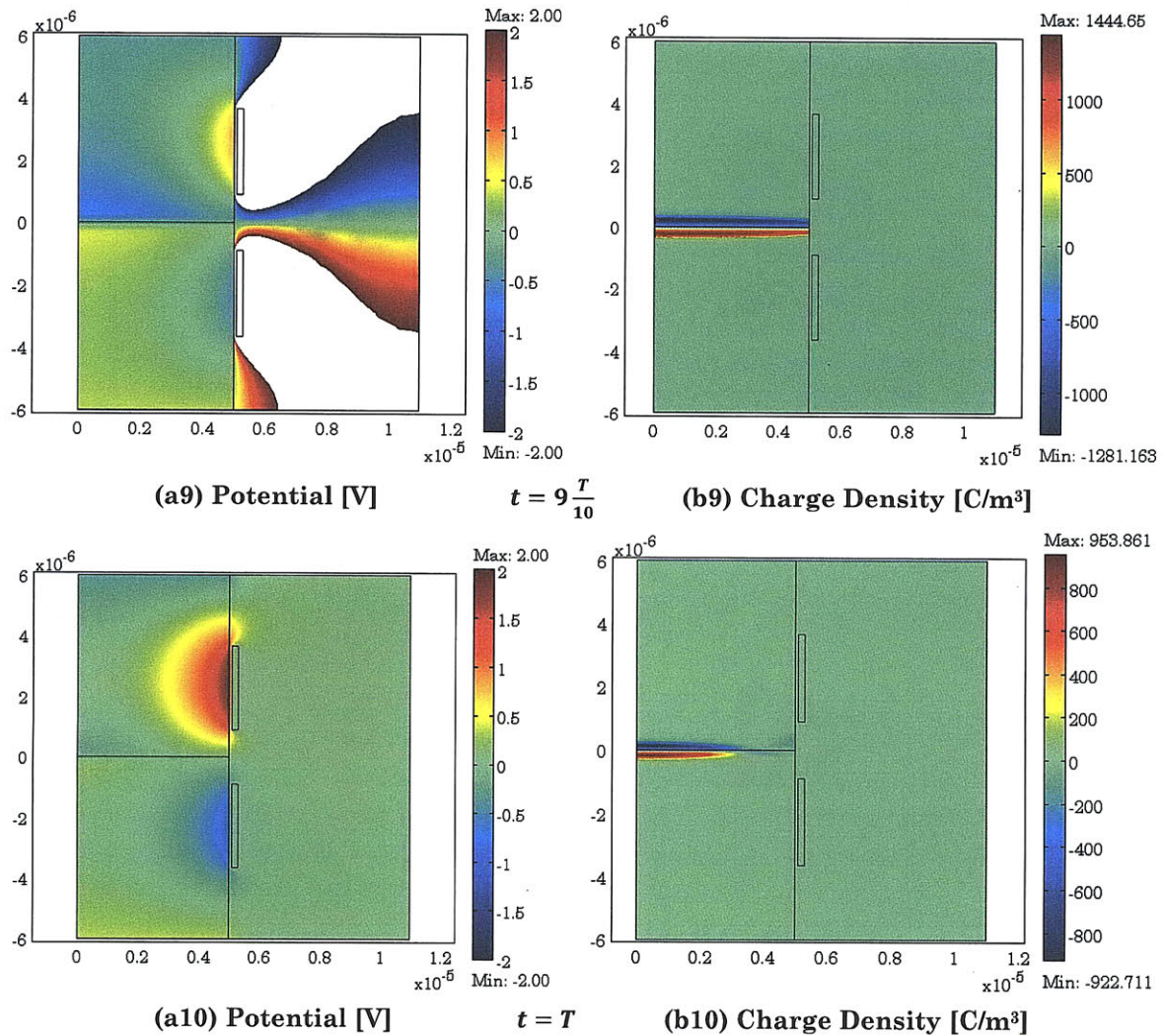


Figure 2-16: Colormapped surface plots of scalar potential [V] (a1—a10) and space charge density [C/m³] (b1—b10) at intervals of length $T/10$ for 10GHz excitation.

The space charge density plots of Figure 2-16 show the depth to which the junction conducts. Figure 2-17 helps to illustrate this by superimposing electric field streamlines on top of the space charge density plot in the silicon region at $t = T$ when the junction is forward biased. The junction conducts to a depth of approximately $2\mu\text{m}$. Below this depth, streamlines can be seen terminating on the space charge layer, forming a junction capacitance. Additionally, some streamlines

can be seen terminating on the upper and lower boundaries of the solution space that represent undriven electrical contacts.

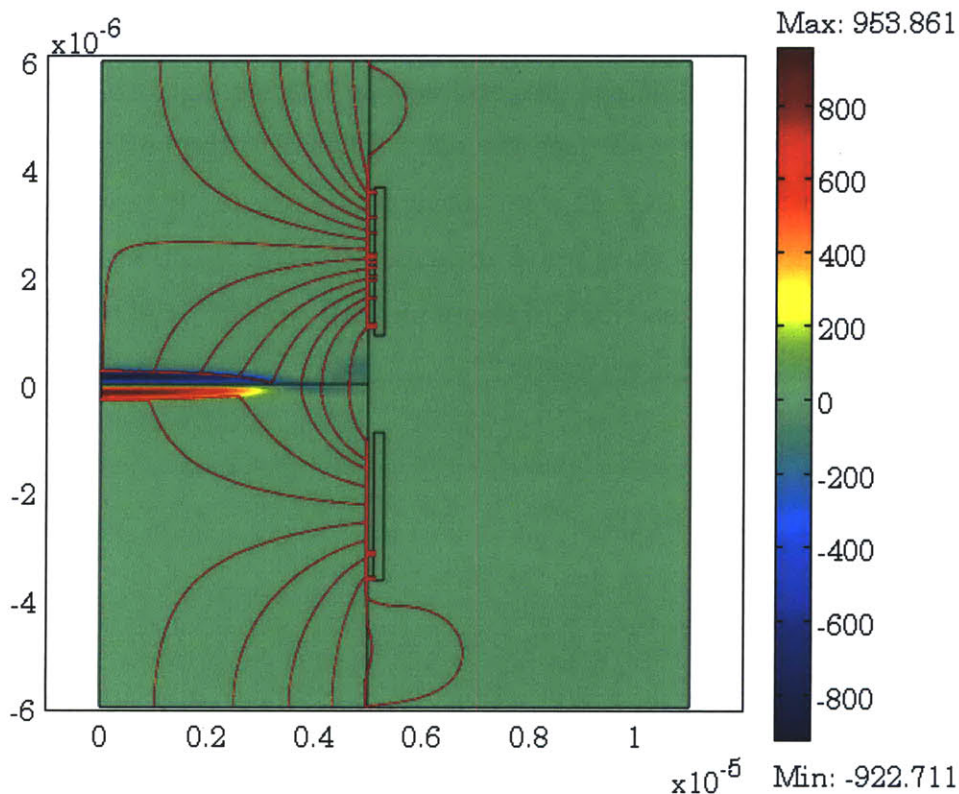


Figure 2-17: Electric field (streamlines) and space charge density [C/m³] (colormapped surface plot) when silicon region is under forward bias.

In the high frequency limit (100GHz), the harmonic distortion in the sensor current begins to diminish. This makes sense as this is likely due to junction capacitance beginning to short out the nonlinear diode. Since the high frequency behavior of a capacitor is to act as a short circuit, this linear path dominates the diode current. There is then no benefit in operating the sensors at such a high frequency. For this specific geometry, there is an apparent “sweet spot” between 10GHz and 50GHz where the junction is able to be detected. In this range the second harmonic current amplitude rises to over 4% of the fundamental (as shown in Figure 2-14).

2.5 FEM Model #2 Setup

A second model was drawn in COMSOL to simulate the more realistic geometry of a p-type well doped into an n-type substrate. In this case the p-type well is not in contact with a boundary that can directly source carriers into the p-type region; rather the well is “floating” and does not extend down to the bottom of the silicon region. Consequently, for free charge carriers to exist in this region they must either be initially doped in or migrate in across the p-n junction. The COMSOL setup for this geometry is described in Sections 2.5.1 – 2.5.3, and the results of the simulation are presented in Section 2.6.

2.5.1 Geometric Properties

The geometry under evaluation is shown in Figure 2-18. An array of three coplanar sensors is centered above a p-type well that is doped into an n-type silicon substrate. The sensors reside in an air-filled region above the surface of the silicon region at a fixed height. A zoomed-in version of the geometry is provided in Figure 2-19 and important dimensions are listed in Table 2-3. For this geometry, sensors are driven by an AC voltage with the outer two electrodes driven 180° out of phase with respect to the center electrode.

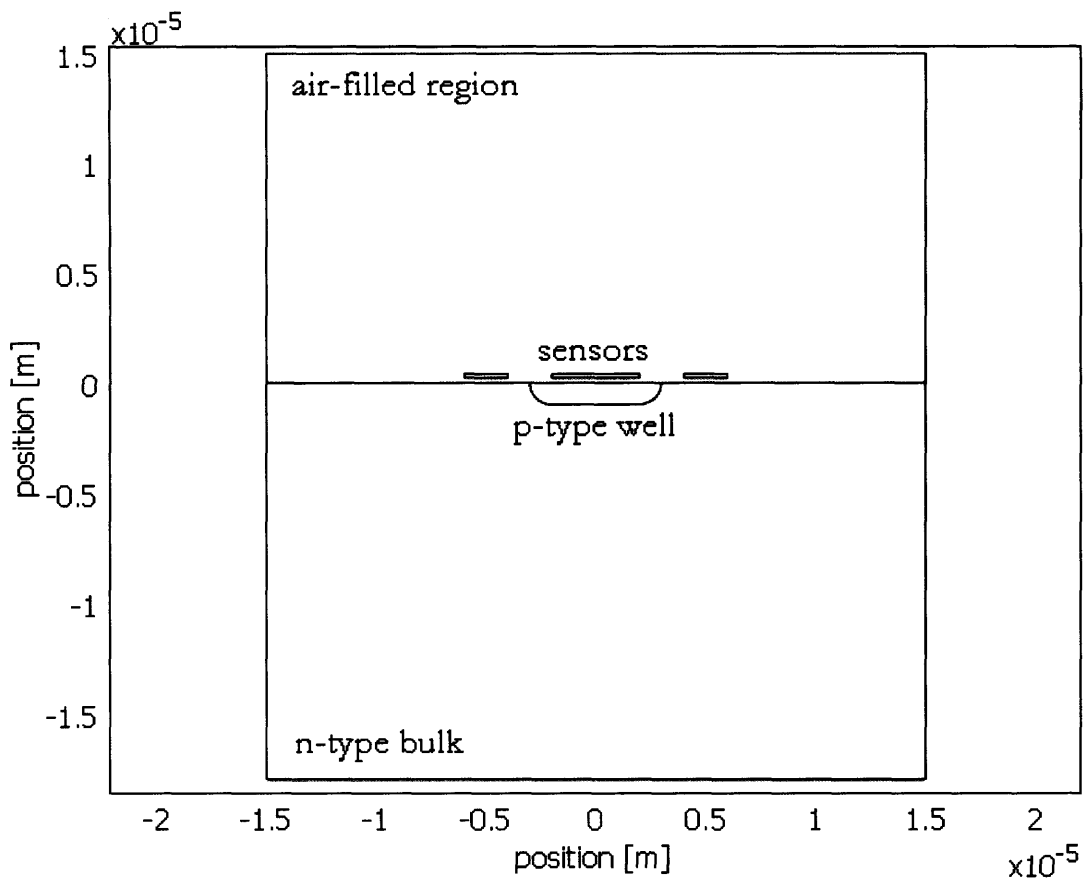


Figure 2-18: COMSOL geometry #2 to be analyzed.

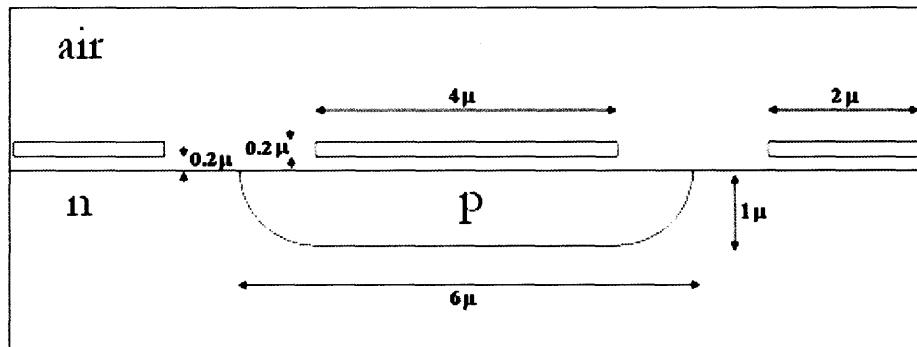


Figure 2-19: Zoomed-in version of COMSOL geometry #2 to show important geometric dimensions.

Table 2-3: Key geometric dimensions for geometry #2

Dimension	Length [μm]
p-well width	6
p-well depth	1
sensor-silicon air gap	0.2
sensor height	0.2
center sensor width	4
side sensor widths	2
sensor-sensor spacing	2

2.5.2 Physical Properties

The silicon region was doped to represent a p-type well floating in an n-type bulk. As was the case in Section 2.3.2—in the interest of achieving numerical convergence in COMSOL—an abrupt, discontinuous “step-junction” was not specified; rather, the dopant concentration function, N , was described using Gaussian functions with a drop-off constant c_d :

$$N = N_{Dn} + N_{Dnmax} e^{-\left(\frac{y+y'}{c_d}\right)^2} - N_{Apmax} e^{-\left(\frac{y}{c_d}\right)^2} \times \begin{cases} 1, & -x' < x < x' \\ e^{-\left(\frac{x-x'}{c_d}\right)^2}, & x \geq x' \\ e^{-\left(\frac{x+x'}{c_d}\right)^2}, & x \leq -x' \end{cases} \quad (2.24)$$

where N_{Dnmax} is the maximum donor (n-type) doping concentration, N_{Apmax} is the maximum acceptor (p-type) doping concentration, and N_{Dn} is the doping concentration of a majority of the n-type bulk representing an epitaxial layer. The parameter y' represents the depth at which the n-type doping function begins to

smoothly transition from N_{Dnmax} to N_{Dn} and has a value of $18\mu\text{m}$. The parameter x' represents the horizontal positions at which the doping function begins to smoothly transition from N_{Apmax} to N_{Dn} and has a value of $2\mu\text{m}$. A summary of the physical parameters assigned to the silicon region is provided in Table 2-4.

Table 2-4: Electrical parameters used in FEM simulation

Parameter	Value	Units
N_{Dnmax} : maximum n-type doping	10^{16}	$[\text{1}/\text{cm}^3]$
N_{Apmax} : maximum p-type doping	10^{16}	$[\text{1}/\text{cm}^3]$
N_{Dn} : n-type epitaxial layer doping	10^{15}	$[\text{1}/\text{cm}^3]$
n_i : intrinsic impurity concentration for Si	$1.46(10^{10})$	$[\text{1}/\text{cm}^3]$
μ_p : hole mobility	200	$[\text{cm}^2/\text{Vs}]$
μ_n : electron mobility	800	$[\text{cm}^2/\text{Vs}]$
k : Boltzmann's constant	$1.38(10^{-23})$	$[\text{J}/\text{K}]$
T : temperature	300	$[\text{K}]$
q : elementary electric charge	$1.602(10^{-19})$	$[\text{C}]$
ϵ_r : Si relative permittivity	11.8	--
c_d : doping fall-off constant	0.659	$[\mu\text{m}]$
y_1 : doping fall-off position	-0.3	$[\mu\text{m}]$

2.5.3 Solver Properties

The COMSOL geometry is solved using the same sets of equations provided in Section 2.3.3. The relevant boundary conditions are shown in Figure 2-20.

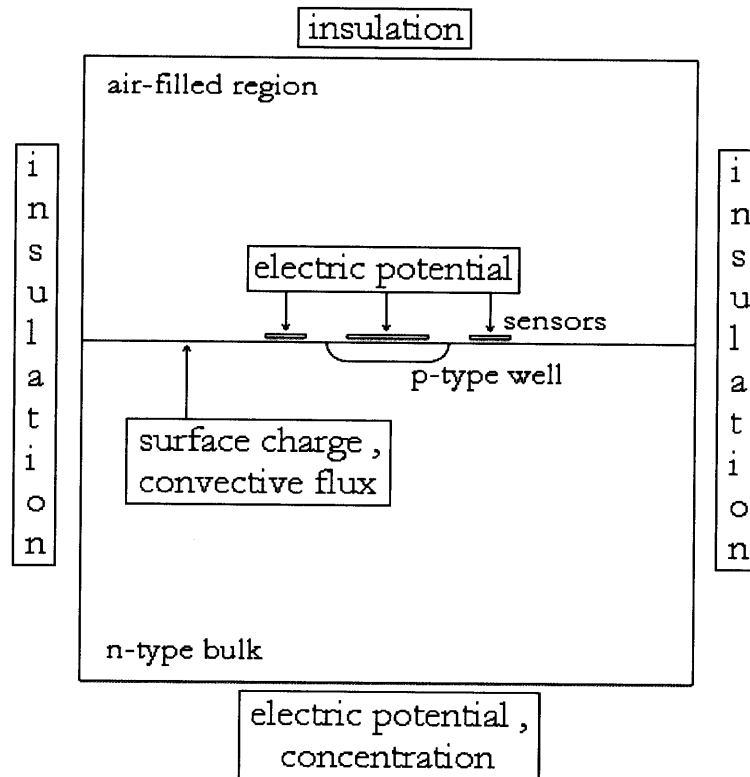


Figure 2-20: Boundary conditions for COMSOL geometry #2.

Additional details regarding the COMSOL model properties and solver settings for FEM Model #2 can be found in Appendix C.

2.6 FEM Model #2 Simulation Results

This section provides the results of several COMSOL simulations that were run with the parameters and settings described in Section 2.5. Figure 2-21 and Figure 2-22 show the initial distribution of free holes and free electron in the silicon region, respectively. The Gaussian-shaped roll-off of the large concentration of free holes in the p-well to the much lower concentration in the n-type bulk is evident in Figure 2-21; the same is true for the electron distribution in Figure 2-22. Figure 2-23 shows the initial scalar potential distribution. The figure shows a built-in

equilibrium potential of approximately 0.6 V across the p-n junction. The equilibrium space charge layers (depletion region) that sets up this built-in potential bias is shown in Figure 2-24.

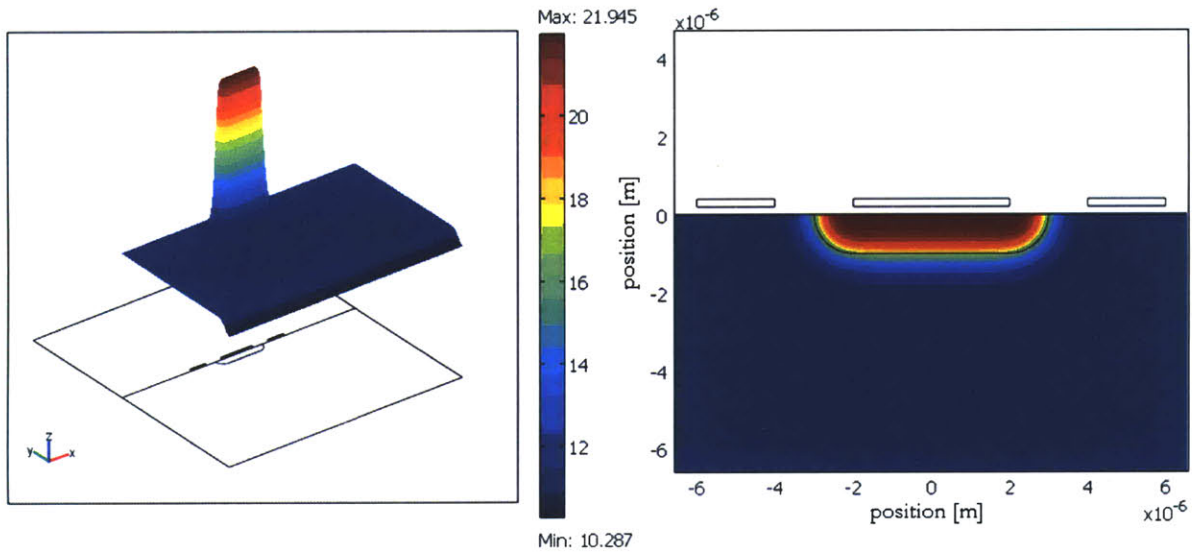


Figure 2-21: Log_{10} (initial concentration of holes) in $[1/\text{m}^3]$ displayed as a 3-D (left) and 2-D (right) colormap.

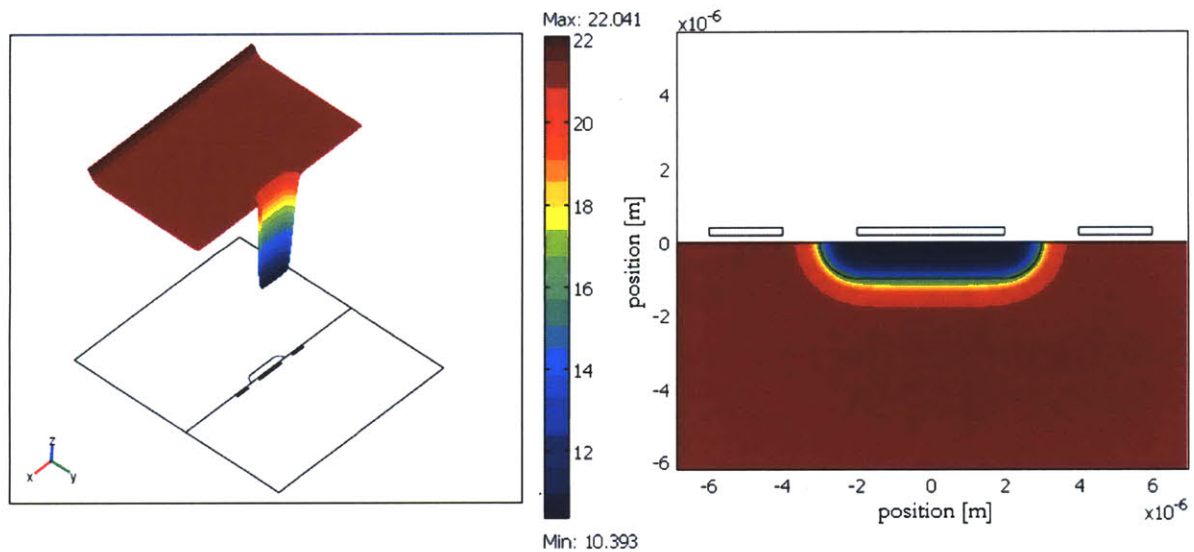


Figure 2-22: Log_{10} (initial concentration of electrons) in $[1/\text{m}^3]$ displayed as a 3-D (left) and 2-D (right) colormap (note: 3-D view is shown at a reverse angle of Figure 2-21).

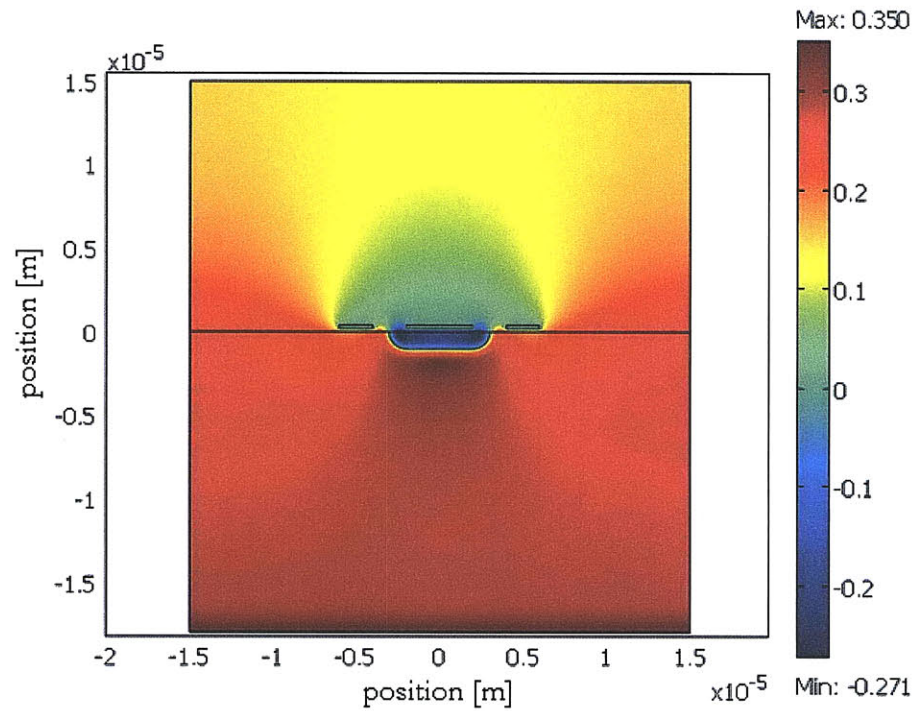


Figure 2-23: Initial scalar potential distribution [V]. There exists a built-in equilibrium potential of approximately 0.6 V across the p-n junction.

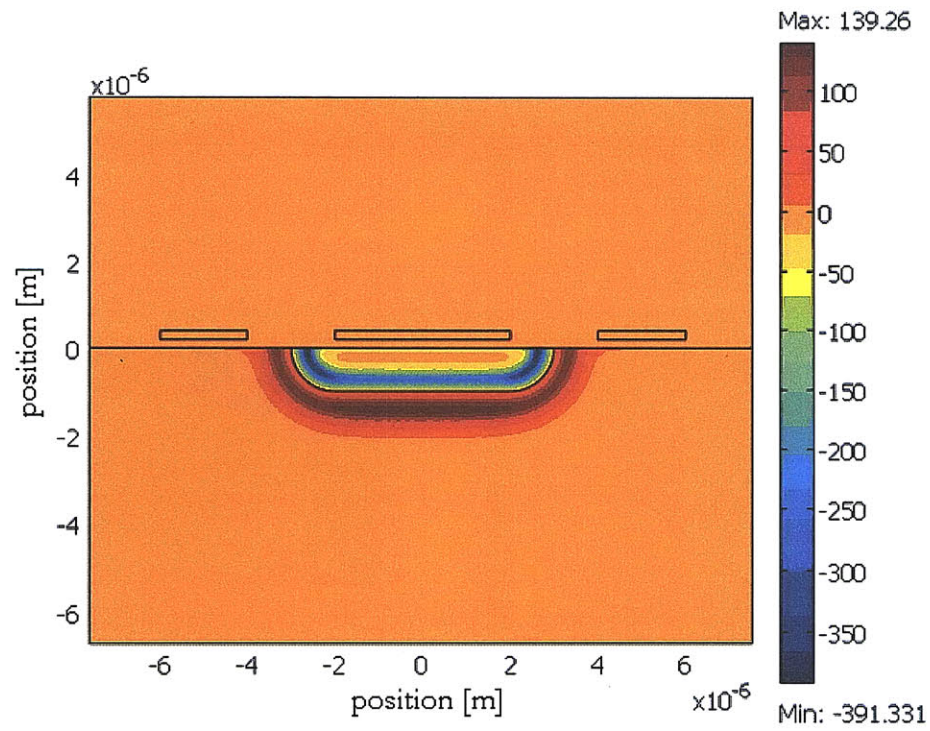


Figure 2-24: Initial space charge density [C/m³] zoomed in near p-well to illustrate the width of the depletion region.

Sensors were driven with an AC voltage such that the center electrode was 180° out of phase from the two outer electrodes:

$$V_{center} = 5 \sin (2\pi ft) \quad (2.25)$$

$$V_{outer} = -5 \sin (2\pi ft) \quad (2.26)$$

Simulations were run at operating frequencies of 500MHz, 1GHz, 5GHz, 10GHz, and 50GHz. This range was chosen for the same reasons described in Section 2.4.1, but the range is slightly lower in frequency than those chosen for FEM Model #1 because the hole mobility was reduced from 400 [cm²/Vs] to 200 [cm²/Vs] and the n-type region doping was reduced from 10¹⁶ [1/cm³] to 10¹⁵ [1/cm³]. These frequencies should then demonstrate the lower and upper frequency limits of the sensor operation with respect to charge relaxation in the silicon regions. For each of these cases, the center electrode's current was measured using the integration path shown in Figure 2-25. This integration path simulates top-side guarding of the center electrode and increases the sensitivity of the current response to the semiconductor region. Top-side guarding shunts the electric fields from the center electrode into the bulk and prevents them from fringing through the air-filled region above the sensors. An FFT was performed to determine if the junction's nonlinear dynamics were reflected in the sensor current. Figure 2-26 – Figure 2-30 provide the FFT results.

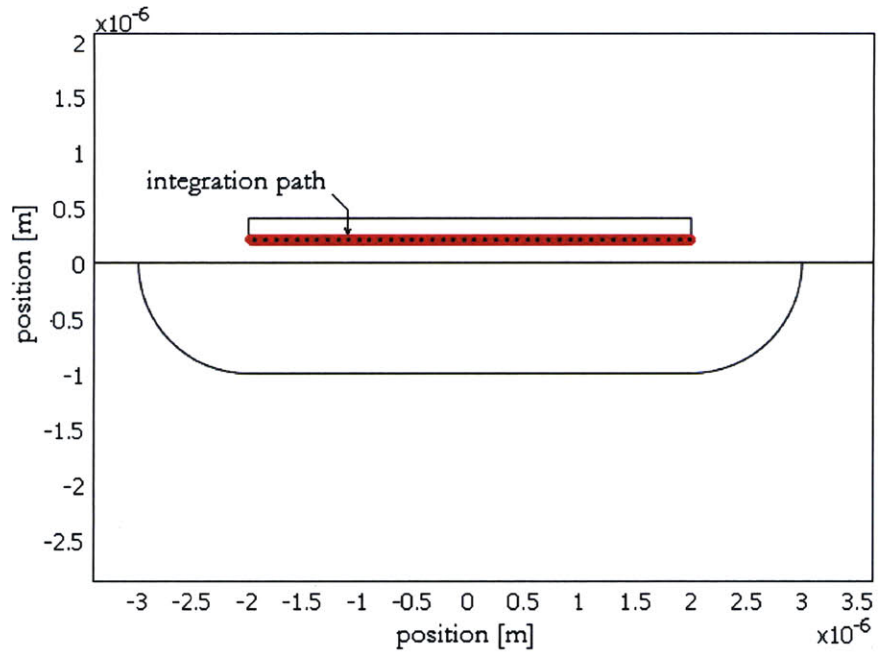


Figure 2-25: Integration path for simulating a guarded electrode.

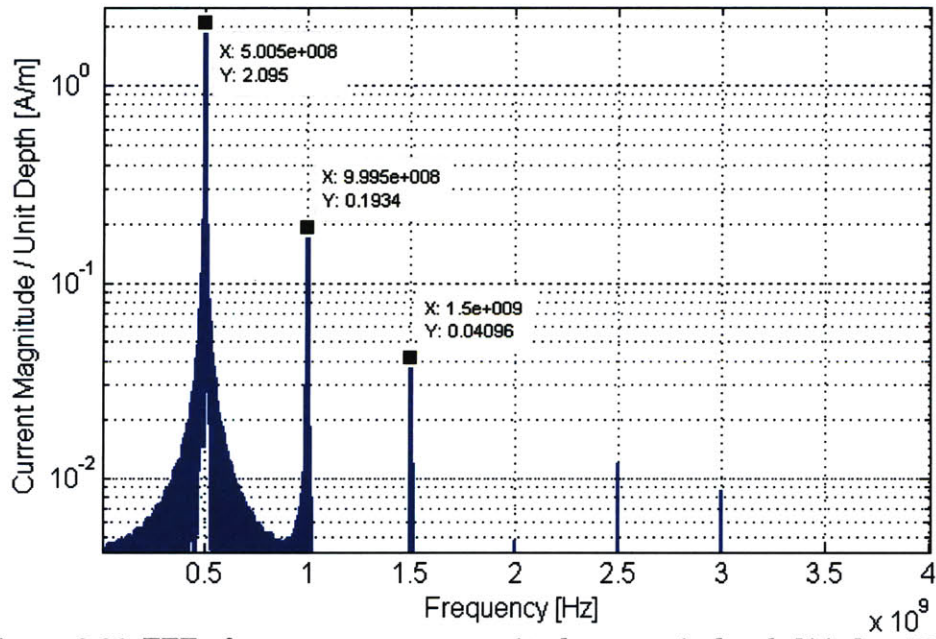


Figure 2-26: FFT of sensor current magnitude per unit depth [A/m] at 500MHz fundamental drive.

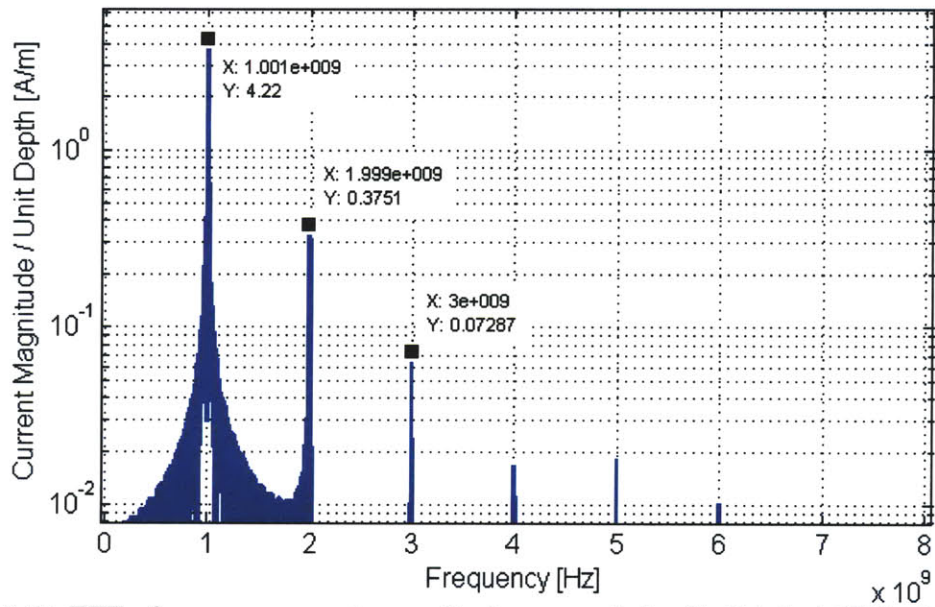


Figure 2-27: FFT of sensor current magnitude per unit depth [A/m] at 1GHz fundamental drive.

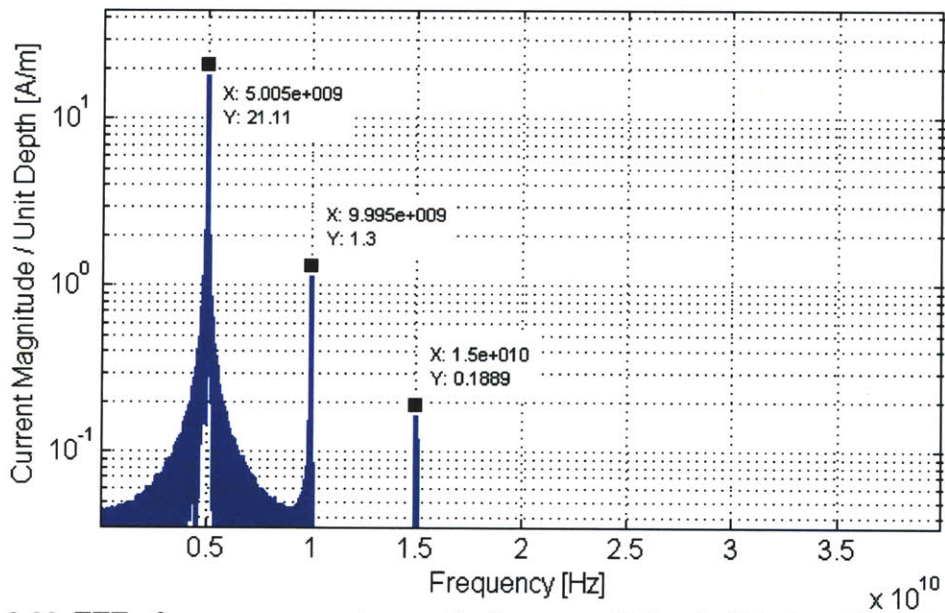


Figure 2-28: FFT of sensor current magnitude per unit depth [A/m] at 5GHz fundamental drive.

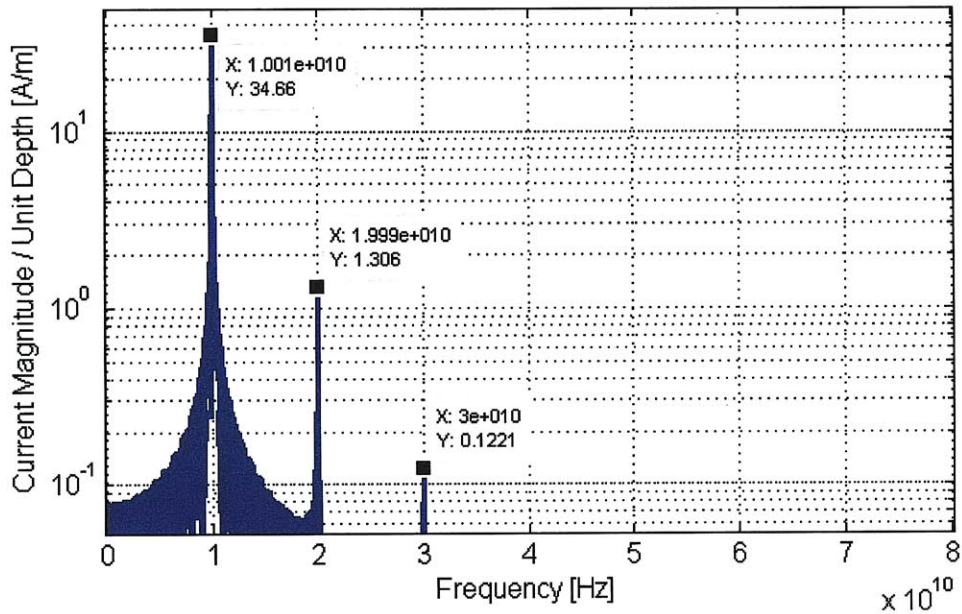


Figure 2-29: FFT of sensor current magnitude per unit depth [A/m] at 10GHz fundamental drive.

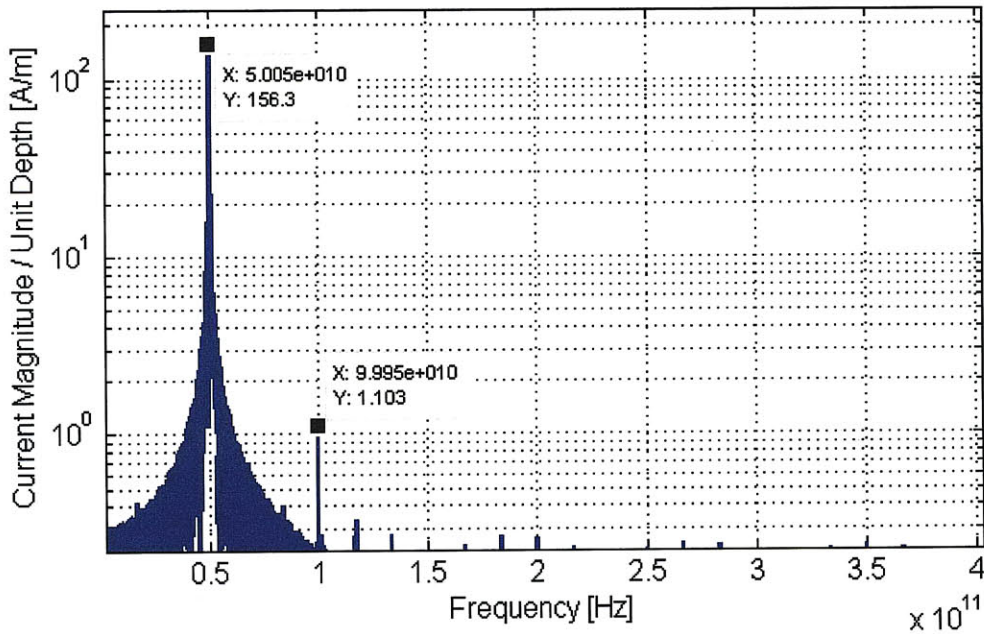


Figure 2-30: FFT of sensor current magnitude per unit depth [A/m] at 50GHz fundamental drive.

These results can be compared by examining the ratio of the second harmonic component of the current to the first harmonic component (as shown in Figure 2-31).

As was the case in Section 2.4.2, the junction capacitance appears to short out the diode at high frequencies, and the nonlinearity in the sensor current diminishes. In this case study, however, a low-frequency roll-off is not witnessed. This could be due to fact that the p-well is relatively shallow and presents the sensors with a much longer junction to turn on than did the first case study. Additionally some physical parameters were changed: the n-type region had a lower doping than the first case study (10^{15} [1/cm³] vs. 10^{16} [1/cm³]), and the hole mobility μ_p was lower (200 [cm²/V·s] vs. 400[cm²/V·s]). It may be the case that simulations were not run at a low enough frequency to see the low-frequency roll-off, but numerical convergence became difficult for such long time scales.

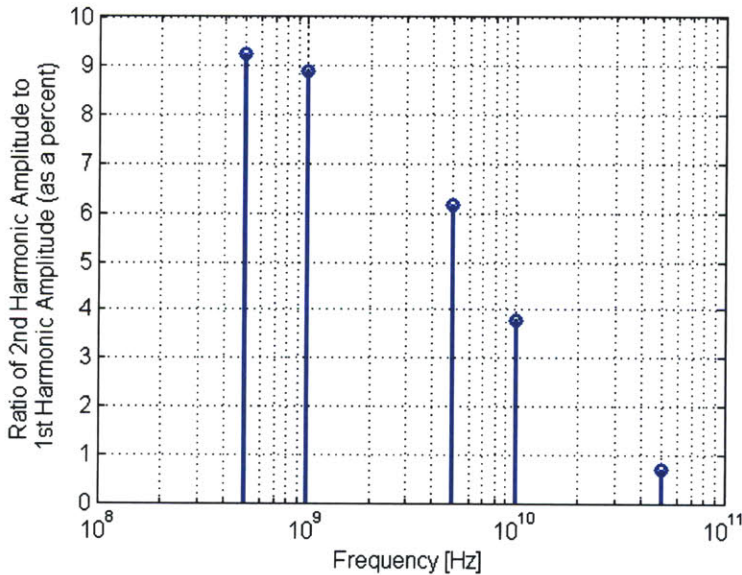


Figure 2-31: Ratio of 2nd harmonic amplitude to 1st harmonic amplitude of center sensor current per unit depth (expressed as a percentage) vs. fundamental drive frequency [Hz].

2.7 FEM Model #2 Sensor Scan Results

To this point, the sensors in both the FEM Model #1 and FEM Model #2 simulations have remained stationary. In both cases the sensors were positioned such that they straddled the p-n junctions and were proven to be capable of turning the junctions on and off. To demonstrate the sensors' ability to detect junctions for imaging purposes, sensors need to be scanned laterally over the surface of the silicon region while the frequency spectrum of the sensors' currents are monitored.

In this section, the sensors from FEM Model #2 are scanned laterally past the p-type well with the center sensor currents monitored at multiple positions in space. Figure 2-18 and Figure 2-19 show the geometry under evaluation when the sensors are centered over the p-type well. COMSOL Solver settings are identical to those described in Section 2.5, however, the sensor array is now free to move laterally over the surface of the silicon region at a fixed scan height of 200nm. Figure 2-32 illustrates how the array of three sensors is scanned horizontally over the surface of the silicon region. The sensor array is scanned from 8 μ m left-of-center to 8 μ m right-of-center (the position of the sensor head is taken to be the horizontal position of the center of the middle electrode relative to the center of the p-type well) in 2 μ m increments. For this scan, sensors are driven by an AC voltage at a fundamental frequency of 1GHz.

For each position in space, the frequency spectrum of the magnitude of the center sensor's current is monitored for harmonic distortion. To simulate a guarded electrode, only the charge on the bottom of the center electrode is considered (as shown in Figure 2-25). Again, this simulates top-side guarding of the center electrode and increases the sensitivity of the current response to the semiconductor region.

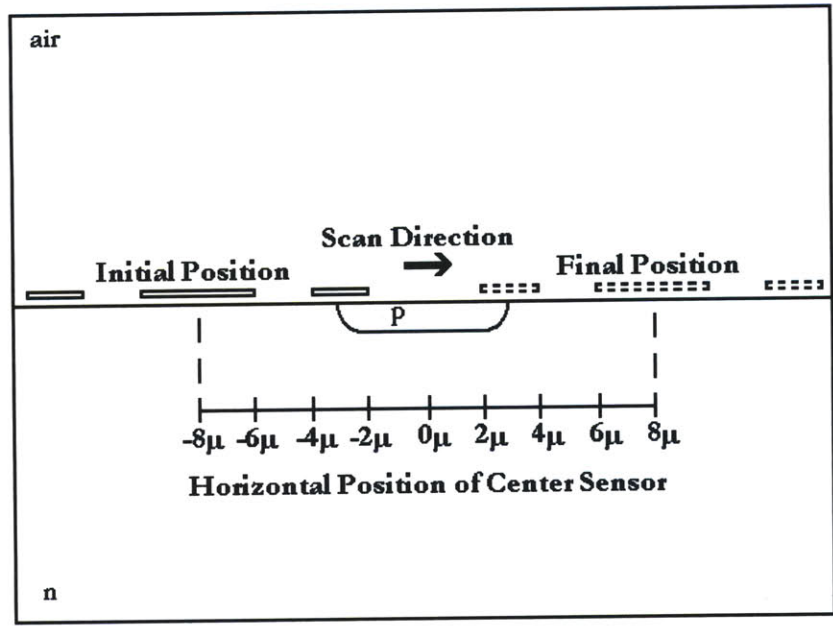


Figure 2-32: Horizontal scan of sensor array past a p-type well in an n-type bulk. The sensor array is scanned from $8\mu\text{m}$ left-of-center to $8\mu\text{m}$ right-of-center in $2\mu\text{m}$ increments (nine total positions). The sensor array is shown to be moving from its leftmost position (solid sensors) to its rightmost position (dashed sensors).

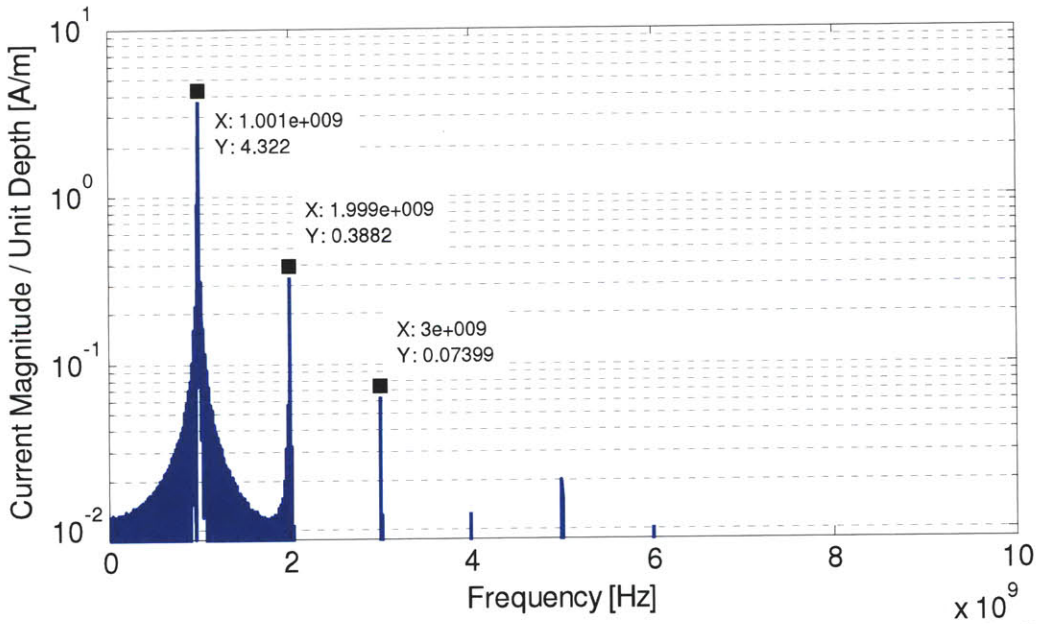


Figure 2-33: FFT of center sensor current magnitude per unit depth [A/m] when positioned $0\mu\text{m}$ left-of-center. 1GHz fundamental drive frequency.

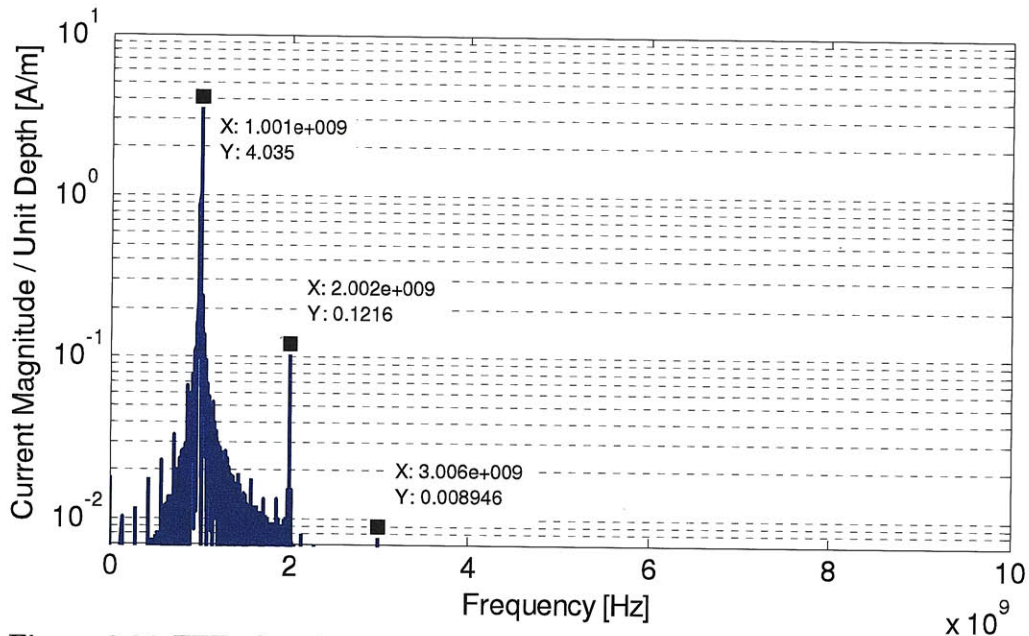


Figure 2-34: FFT of center sensor current magnitude per unit depth [A/m] when positioned $2\mu\text{m}$ left-of-center. 1GHz fundamental drive frequency. False subharmonics are present in the FFT because the sensor current did not reach perfect sinusoidal steady state in the COMSOL simulation. This creates a periodically modulated envelope on the waveform which causes unwanted spikes in the frequency spectrum.

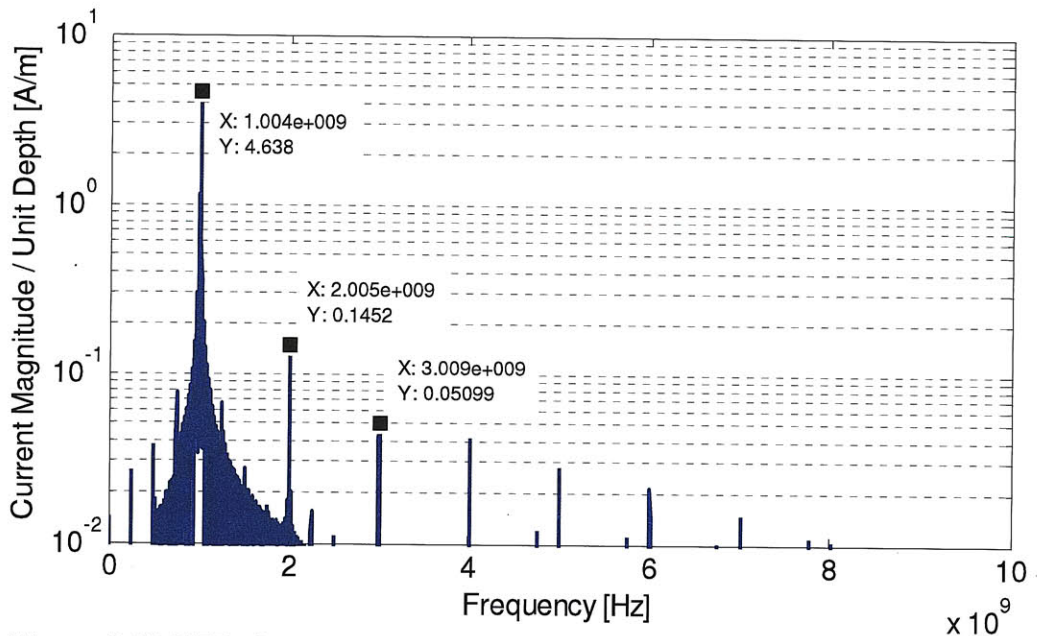


Figure 2-35: FFT of center sensor current magnitude per unit depth [A/m] when positioned $4\mu\text{m}$ left-of-center. 1GHz fundamental drive frequency. Again, false subharmonics are present in the FFT because the sensor current did not reach perfect sinusoidal steady state in the COMSOL simulation. This creates a periodically modulated envelope on the waveform which causes small, unwanted spikes in the frequency spectrum.

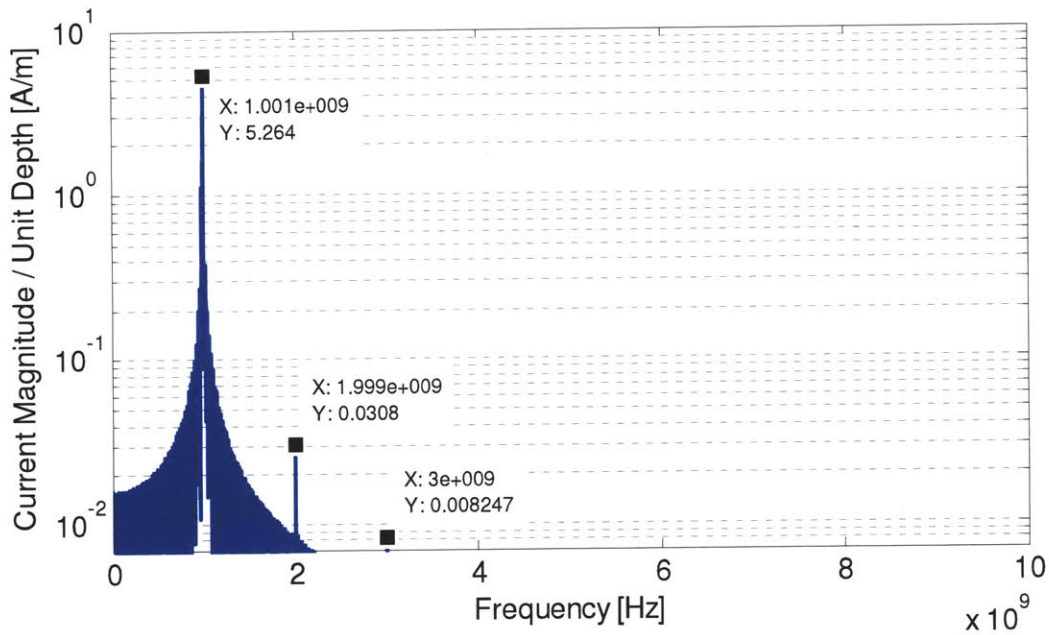


Figure 2-36: FFT of center sensor current magnitude per unit depth [A/m] when positioned $6\mu\text{m}$ left-of-center. 1GHz fundamental drive frequency.

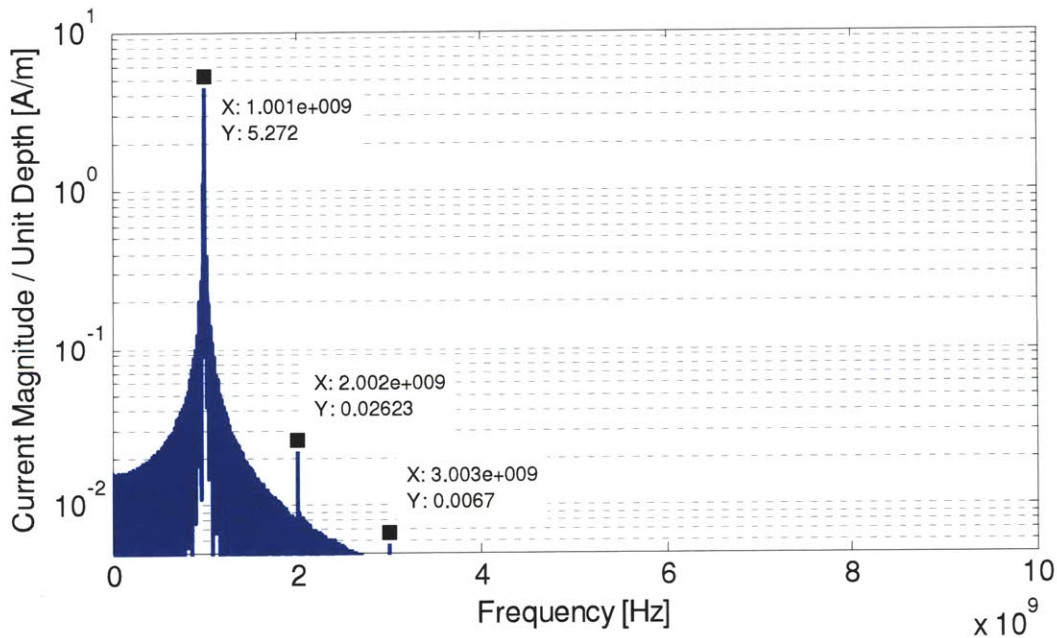


Figure 2-37: FFT of center sensor current magnitude per unit depth [A/m] when positioned $8\mu\text{m}$ left-of-center. 1GHz fundamental drive frequency.

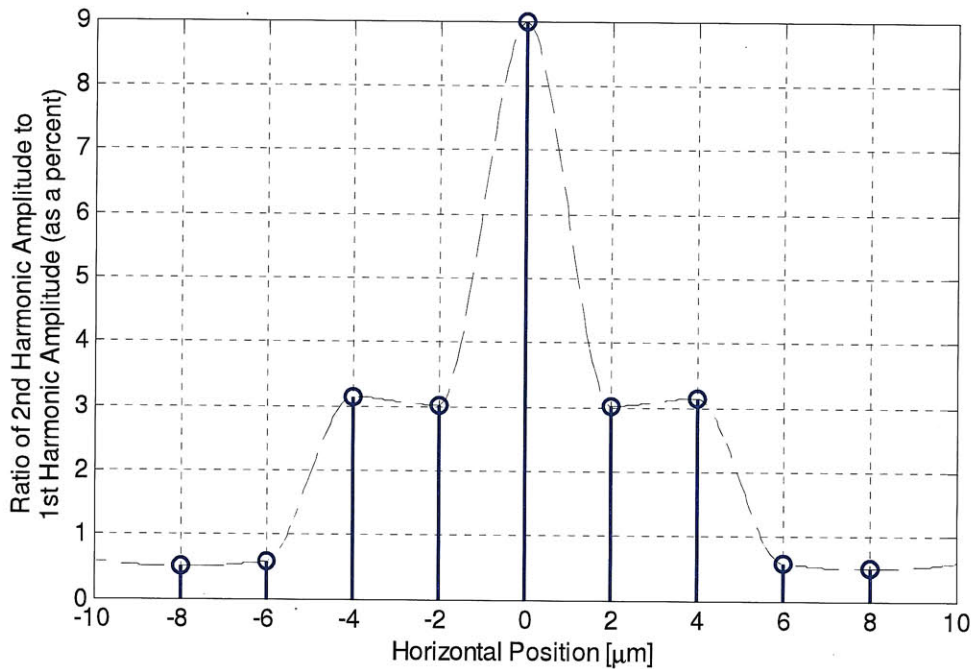


Figure 2-38: Ratio of 2nd harmonic amplitude to 1st harmonic amplitude of center sensor current per unit depth (expressed as a percentage) vs. horizontal position [μm] (relative to the center of the p-well).

The FFT results for the current on the center sensor are shown in Figure 2-33 – Figure 2-37 for the sensor positioned at 0 μm , 2 μm , 4 μm , 6 μm , and, 8 μm to the left of the center of the p-well. Due to the symmetry of the sensor head, results are identical and symmetric for when the array is positioned 2 μm , 4 μm , 6 μm , and, 8 μm to the right of the center of the p-well. In Figure 2-34 and Figure 2-35 false subharmonics are present in the FFTs because the sensor current did not reach perfect sinusoidal steady state in the COMSOL simulation. Since the FFT is fed concatenated copies of the time-domain waveform from COMSOL, this creates a periodically modulated envelope on the waveform which causes small, unwanted spikes in the frequency spectrum that should be ignored.

The results of the full scan from 8 μm to the left of the center of the p-well to 8 μm to the right of the center are summarized in Figure 2-38. In this figure the ratio of the second harmonic current amplitude to the fundamental current

amplitude is expressed as a percentage for each of the nine positions in space. At $\pm 6 \mu\text{m}$, with there is a surprisingly low (less than 1%) second harmonic contribution to the center sensor's current. This was initially unexpected because at these two positions, the center sensor straddles a p-n junction with one of the outer two electrodes. It is likely that the current on the center sensor is then dominated by the coupling to the other side electrode along a purely linear path. Though it is not shown, for the rightmost electrode when positioned at $-6 \mu\text{m}$ (or alternatively the leftmost electrode when positioned at $+6 \mu\text{m}$), is approximately a 3.25% second-to-first-harmonic ratio. This then makes sense that for these positions, the side electrode that is straddling the junction still experiences significant harmonic distortion, but the center sensor current is dominated by the linear path to the other side electrode.

When the array is perfectly centered over the p-well at $0 \mu\text{m}$, there is a strong spike in the harmonic distortion. This is a good quality for imaging purposes. It might then be desirable to design the sensor array to match the specific sizes and spacing of the doped wells to maximize the harmonic distortion experienced by the sensors.

Results from these case studies demonstrate how EQS sensors' fringing fields can couple into doped semiconducting substrates and detect a p-n junction. The first case study demonstrated a clear bandpass "sweet spot" for sensor operation while the second case study only showed a high frequency roll-off in sensor performance. In both cases, it is important to take away the fact that sensors should be operated at a frequency slightly lower than the charge relaxation break frequency (Equation (2.20)) of the silicon regions to achieve significant penetration of electric fields into the material, but not so high a frequency as to short out the junctions' nonlinear characteristics. Monitoring sensor currents for nonlinearity in this manner could potentially provide new methods for the imaging of integrated circuits.

3 Locating Surface Features and Contaminants

It was demonstrated in Chapter 2 that EQS sensors are capable of detecting features in the near-surface volume of a material. In the case that the material under evaluation is conducting (or semiconducting as was the case in Chapter 2), it is desirable for the sensors to operate at a frequency comparable to the charge relaxation break frequency (Equation (2.20)) of the material under evaluation to achieve significant penetration of electric fields into the material. In cases where the material under evaluation is highly conducting, sensors are often unable to operate at a high enough frequency to penetrate the materials bulk. For example, copper, which has an electrical conductivity of approximately $5.8 \times 10^6 [S/m]$ and a dielectric constant of $\epsilon_r = 1$, has a charge relaxation break frequency on the order of $10^{17} [Hz]$ [20]. In this limit, EQS sensors are only able to detect a material's surface topology or features, defects, and objects that might lie on that material's surface. If one needed to see features beneath the surface of a good conductor, MQS sensors could be used due to enhanced field penetration depths when operated at low frequencies [4]. This chapter focuses solely on using EQS sensors for detecting features/objects that lie on the surface of a material whose charge relaxation break frequency is much higher than the sensor's operating frequency.

3.1 Detecting Contaminants on a Photomask

One specific application which serves as the impetus for this chapter's research is locating and removing contaminant particles on photoreticles used in the mass production of integrated circuitry. Typically, photomasks are protected by a thin transparent membrane called a pellicle whose purpose is to catch contaminant particles, keeping them optically out of focus during photolithography. However, a heavily contaminated pellicle or a contaminated photomask might produce flawed devices, and it is thus desirable to know if a photomask and/or pellicle is contaminated. Figure 3-1 illustrates a contaminated photomask with a protective pellicle. As lithography methods continue to operate at smaller and smaller wavelengths, it is becoming more favorable to use pellicle-less masks thus increasing the risk of photomask contamination. As wavelengths become smaller, conventional scattering techniques for detecting contaminants becomes increasingly difficult. This chapter investigates the feasibility of using EQS sensors for detecting contaminants on pellicle-less photomasks.

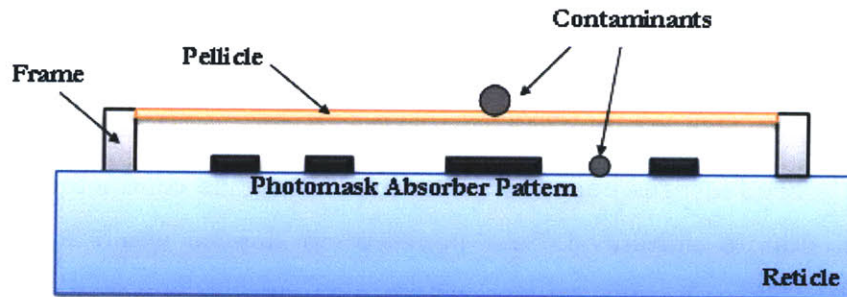


Figure 3-1: Illustration of contaminated photomask.

3.1.1 Contaminated Photomask Simulation Setup

A geometry was drawn in COMSOL (shown in Figure 3-2) to represent an array of EQS electrodes scanning laterally over the surface of an unprotected extreme ultraviolet lithography (EUVL) photomask. The purpose of setting up this geometry was to analyze how well the array could detect a contaminant particle stuck between two absorbers in an EUVL photomask pattern. Detecting a contaminant stuck in an absorber layer gap represents a worst-case scenario since it is as far away from the sensor head as possible. Key geometric and electrical parameters used in the simulation are summarized in Table 3-1 and Table 3-2 respectively. These parameters were chosen to represent those of a real EUVL photomask [21]. Additional details regarding the COMSOL model properties and solver settings for this geometry can be found in Appendix D.

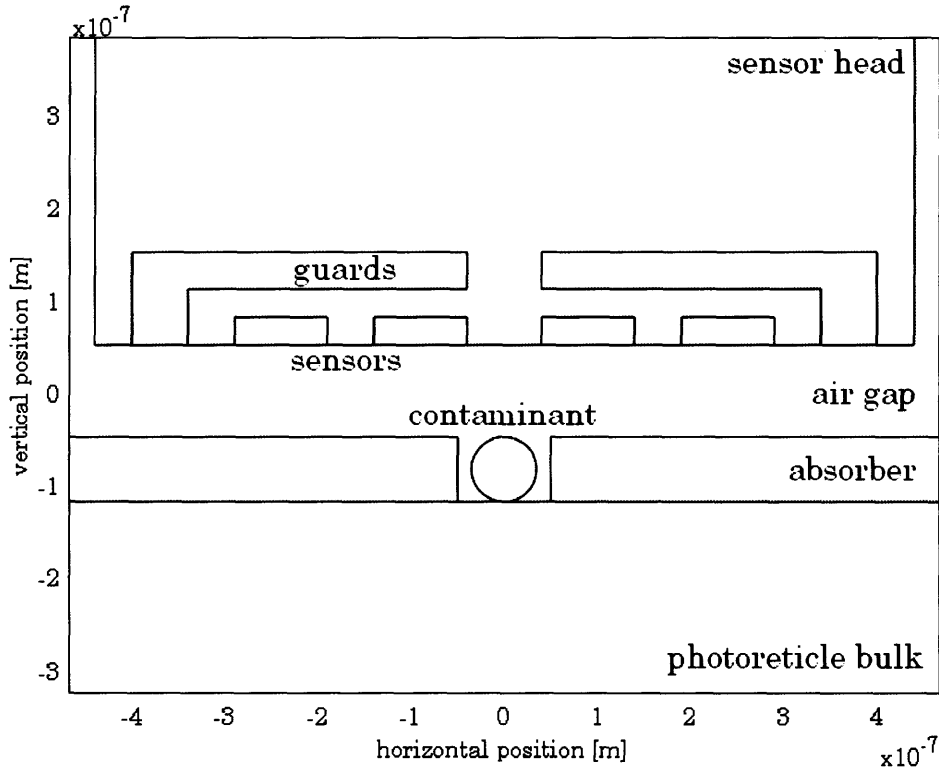


Figure 3-2: COMSOL geometry for contaminated EUVL photomask simulation. Since simulation is performed on 2D solvers, contaminant object is cylindrical.

Table 3-1: Key geometric dimensions for contaminated EUVL photomask simulation

Dimension	Length [nm]
air gap (sensor scan height)	100
absorber layer vertical thickness	70
individual sensor horizontal dimension	100
individual sensor vertical dimension	30
total sensor head horizontal width	880
absorber layer air gap horizontal width	100
contaminant particle radius	35
guard vertical thickness	40
sensor – sensor horizontal spacing (inner edge-to-edge)	50
Spacing between center two sensors (inner edge-to-edge)	80
sensor – guard horizontal spacing (inner edge-to-edge)	60
sensor – guard vertical spacing (inner edge-to-edge)	30

Table 3-2: Electrical Parameters used in contaminated EUVL photomask simulation

Parameter	Value
sensor head relative permittivity	3.9
absorber layer relative permittivity	2
absorber layer conductivity	10^6 [S/m]
photoreticle bulk conductivity	PEC
sensor conductivity	PEC
sensor frequency	1 [GHz]

Each sensor is driven by a 1GHz sinusoidally varying voltage source with a peak amplitude of 1V. The two rightmost sensors and guard shown in Figure 3-2 are driven 180° out of phase from the two leftmost sensors and guard so as to create a spatial square wave alternating in time.

Because each sensor/guard is treated as a perfect electrical conductor (PECs), we can assume there are no fields inside these regions and thus treat them as electric potential boundary conditions. The EUVL photoreticle bulk (which is a highly conducting EUV wavelength distributed Bragg reflective multilayer [21]) is also treated as a PEC. These boundaries are treated as “Port” boundary conditions in COMSOL which can be used to calculate lumped terminal parameters for the system. Since there are four voltage-driven sensors, two voltage-driven guards, and one floating potential boundary to represent the undriven photoreticle bulk, the EQS system can be represented by a 7×7 admittance matrix:

$$\begin{pmatrix} \hat{I}_{S1} \\ \hat{I}_{S2} \\ \hat{I}_{S3} \\ \hat{I}_{S4} \\ \hat{I}_{G1} \\ \hat{I}_{G2} \\ \hat{I}_B \end{pmatrix} = \begin{pmatrix} Y_{11} & Y_{12} & \dots & Y_{16} & Y_{17} \\ Y_{21} & Y_{22} & & Y_{26} & Y_{27} \\ \vdots & & \ddots & & \vdots \\ Y_{61} & Y_{62} & & Y_{66} & Y_{67} \\ Y_{71} & Y_{72} & \dots & Y_{76} & Y_{77} \end{pmatrix} \cdot \begin{pmatrix} \hat{V}_{S1} \\ \hat{V}_{S2} \\ \hat{V}_{S3} \\ \hat{V}_{S4} \\ \hat{V}_{G1} \\ \hat{V}_{G2} \\ \hat{V}_B \end{pmatrix} \quad (3.1)$$

where $\hat{V}_{S1} - \hat{V}_{S4}$ are the four sensor voltages (indexed from left to right), $\hat{V}_{G1} - \hat{V}_{G2}$ are the two guard voltages (indexed from left to right), and \hat{V}_B is the photoreticle bulk voltage. Each of the elements in the admittance matrix, Y_{ij} , represent a mutual admittance coefficient between two ports in the EQS system. By reciprocity, the matrix is symmetric about its main diagonal [22, 23]. Since the bulk is an undriven, floating potential, we do not know \hat{V}_B directly, but rather that $\hat{I}_B = 0$. We can then solve for \hat{V}_B in terms of the other six known voltages:

$$\hat{V}_B = -\frac{(Y_{71}\hat{V}_{S1} + Y_{72}\hat{V}_{S2} + Y_{73}\hat{V}_{S3} + Y_{74}\hat{V}_{S4} + Y_{75}\hat{V}_{G1} + Y_{76}\hat{V}_{G2})}{Y_{77}} \quad (3.2)$$

reduce \hat{V}_B from the system, and solve for the six unknown currents: \hat{I}_{S1} , \hat{I}_{S2} , \hat{I}_{S3} , \hat{I}_{S4} , \hat{I}_{G1} , and \hat{I}_{G2} .

3.1.2 Contaminated Photomask Results

The sensor head shown in Figure 3-2 was scanned laterally past the absorber layer gap at a fixed height of 100nm over the absorber layer's upper surface. Contaminant particles of various different conductivity and permittivity were placed in the absorber layer gap. The magnitude of each of the four sensor currents as a function of sensor head position were determined using the method described in Equations (3.1)—(3.2). The sensor head position is taken to be its horizontal position relative the center of the gap in the absorber layer.

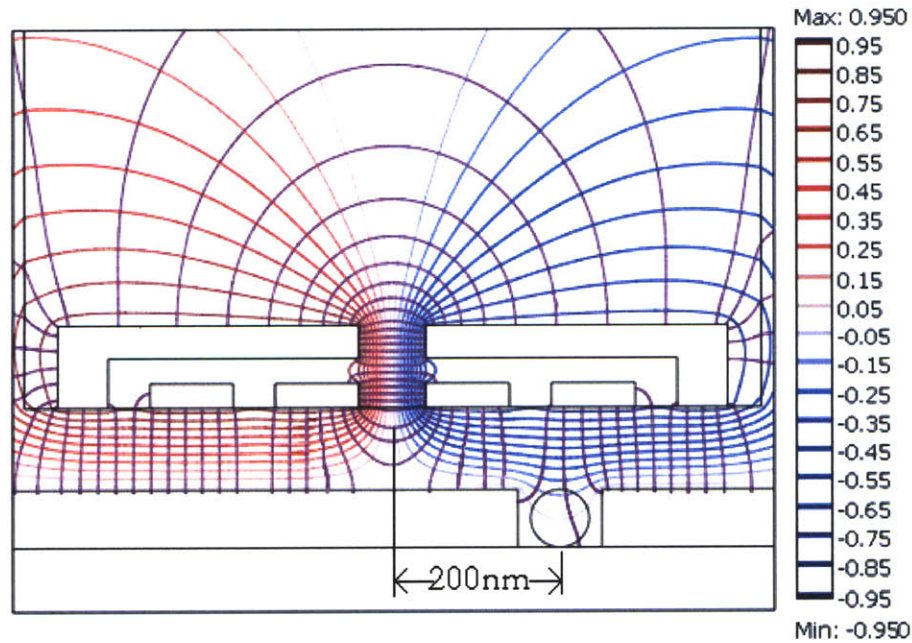
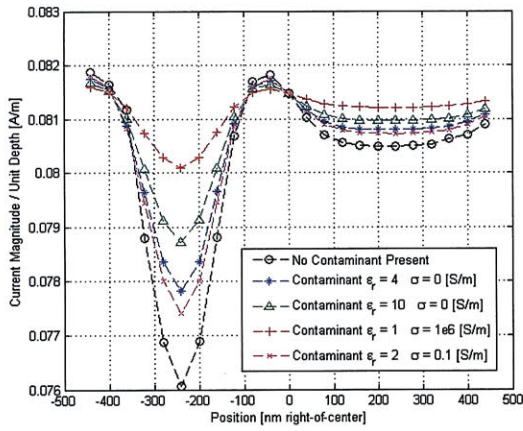


Figure 3-3: Two-dimensional COMSOL simulation results with cylindrical contaminant particle positioned 200nm right of center. In this case, the contaminant particle is characterized by a dielectric constant of $\epsilon_r = 4$. Purple streamlines are electric field lines and the colormapped contours represent equipotentials (lines of constant voltage [V]).

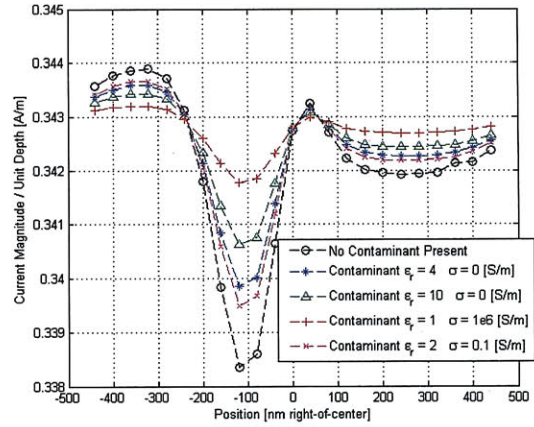
Figure 3-3 shows an electric field plot from COMSOL. In this case a dielectric contaminant with $\epsilon_r = 4$ is positioned in the absorber layer gap 200 nm to the right of the sensor head center, representing an insulating particle stuck in the gap. The electric field lines from sensor 1 are primarily vertical and terminate on the surface of the absorber layer; this is due to guarding effects caused by sensor 2 and the dedicated guard electrode which are driven at the same magnitude and phase as sensor 1. The high density of equipotentials located between sensor 2 and sensor 3 show they are strongly coupled to each other in this region. Consequently, we can expect these two sensors to be poor at detecting the contaminant particle when stuck in the absorber layer gap. Only a small portion of these sensors' fringing fields will couple to the contaminant particle; this should manifest itself as only a weak change in current when these two sensors scan past the contaminant. Some of the fields from sensor 4 are shown to pass through the dielectric contaminant, while others bend and terminate on the sidewalls of the absorber.

Each of the sensor current magnitude responses are plotted (Figure 3-4) for contaminants of various ϵ_r and σ . Because of the symmetry of the sensor head geometry, the results for sensor 1 and sensor 2 will be identical (but mirror images) of the results for sensor 4 and sensor 3, respectively.

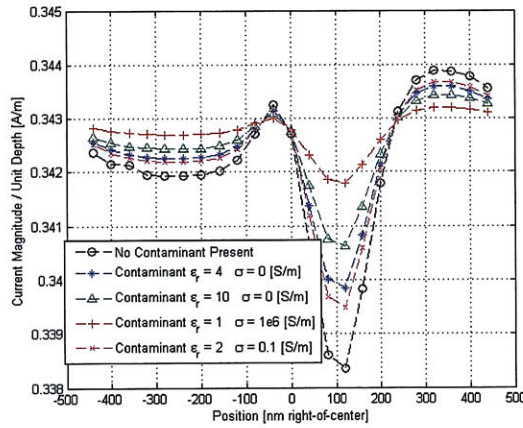
As expected, sensors 1 and 4 react more strongly to the absorber layer gap than sensors 2 and 3. With no contaminant present sensor 1 sees about a 7% change in signal magnitude from the baseline value of 0.083 [A/m] while sensor 2 yields only about a 1.5% change in signal magnitude. In cases where the contaminant particle is a strong dielectric ($\epsilon_r = 10$) or highly conducting ($\sigma = 1e6$ [S/m]) the sensors can distinguish between a contaminated and clean gap with a difference in signal magnitude of 4% or more from what is expected for a clean gap. In the cases where the contaminant is a poor dielectric or weakly conducting, it becomes increasingly more difficult for the sensors to distinguish between a contaminated and clean photomask.



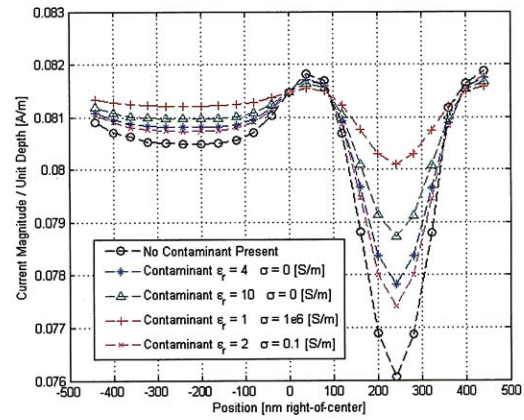
(a) Sensor 1



(b) Sensor 2



(c) Sensor 3



(d) Sensor 4

Figure 3-4: Sensors 1, 2, 3, and 4 current magnitudes per-unit-depth [A/m] vs. horizontal position [nm] relative to center of absorber layer gap.

The widths of the sensors were reduced to 50 nm in attempt to improve sensitivity in detecting contaminant particles. Figure 3-5 shows an electric field plot from COMSOL for the reduced sensor size with a dielectric contaminant particle of $\epsilon_r = 4$ in the absorber layer gap. Some field lines from sensor 4 can still be seen terminating on the sidewalls and sharp corners of the absorber layer; however, the decrease in sensor size should increase lateral resolution and possibly increase sensitivity to the presence of a contaminant.

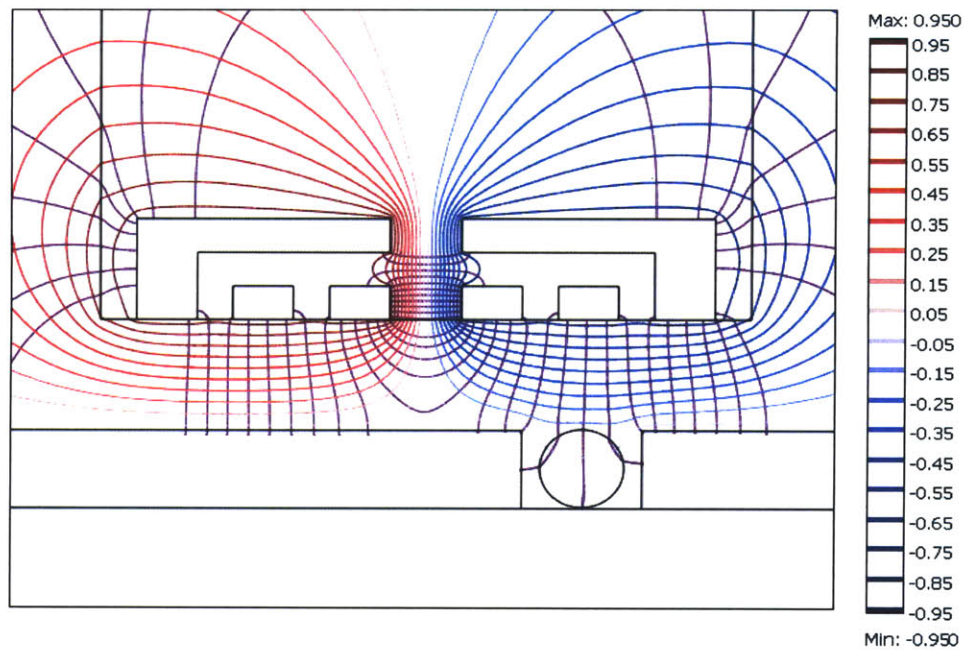


Figure 3-5: COMSOL simulation results for reduced sensor size (50nm width) with contaminant particle positioned 130nm right-of-center. Contaminant particle is characterized by dielectric constant of $\epsilon_r = 4$. Purple streamlines are electric field lines and the colormapped contours represent equipotentials (lines of constant voltage [V]).

The magnitude of current per-unit-depth for sensor 3 and sensor 4 are plotted in Figure 3-6 (again, sensor 1 and sensor 2 have identical, mirror-image responses to sensor 4 and sensor 3, respectively). As expected the sensor 3 current changes very weakly (less than 1%) as it scans past the absorber layer gap. Sensitivity for sensor 4 remains relatively constant compared to the previous case when sensors were 100 nm wide; however, there does exist an improvement in lateral resolution. There is approximately a 7% change in signal magnitude from the baseline value for the case that the gap is clean. In cases where the contaminant particle is a strong dielectric ($\epsilon_r = 10$) or highly conducting ($\sigma = 1e6$ [S/m]), the sensors can distinguish between a contaminated and clean gap with a difference in signal magnitude of 4% or more from what is expected for a clean gap.

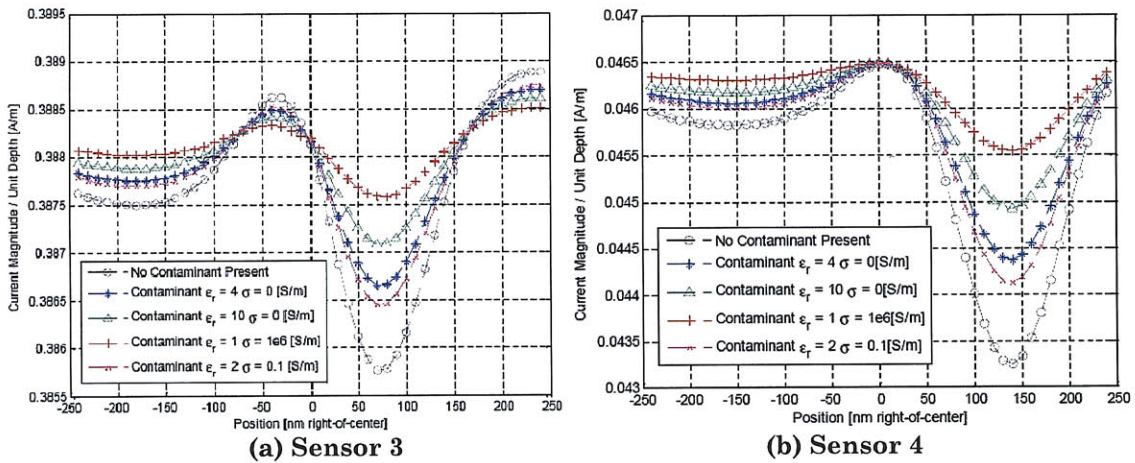


Figure 3-6: Sensor 3 and Sensor 4 current magnitudes per-unit-depth [A/m] vs. position [nm].

Unlike what was presented in Chapter 2, the contaminated EUVL photomask COMSOL simulations demonstrated that direct fringing field coupling between sensors was not the mechanism for detecting contaminant objects stuck in the absorber layer gap. Rather, it was the variations in the vertically dominant fields from guarded sensors coupling to the highly conducting photomask showing up in the individual sensor currents that made detection possible. For the specific differential drive scheme used in this example, highly conducting bulk floats near zero potential and the circuit essentially reduces to two “half-circuits” separated by an approximate virtual ground. This is again due to EQS sensors’ inherent lack of ability to penetrate the surface of a good conductor due to charge relaxation.

An array of MQS sensors operated at a low excitation frequency would indeed be able to penetrate the surface of the highly conducting absorber layer, which may prove advantageous in features detection; however, the MQS sensor array would not be able to detect dielectric contaminants.

3.2 Laboratory Experiment

A macro-scale laboratory experiment was set up to further investigate the performance of the EQS sensors in detecting contaminants stuck in an absorber layer trench. Sensors and samples were fabricated with material properties and aspect ratios so as to mimic those sensors simulated in the Section 3.1. The goal of the experiment is to confirm simulation results. Due to the scalability of Maxwell's Equations, it is expected that sensors fabricated at the millimeter size scale will be able to detect and distinguish objects with the same ability as those simulated at submicron sizes assuming dimensions are scaled equally.

Unlike the simulation shown in Figure 3-2 which did not have any direct electrical contact with the sample, the experiments in this section utilize a ground plane beneath conducting samples. As stated previously, this type of configuration is an excellent "half-circuit" approximation to the differentially driven sensor array show in Figure 3-2. Again, this is because the highly conducting sample floats near zero potential in the previous simulation.

3.2.1 Laboratory Setup

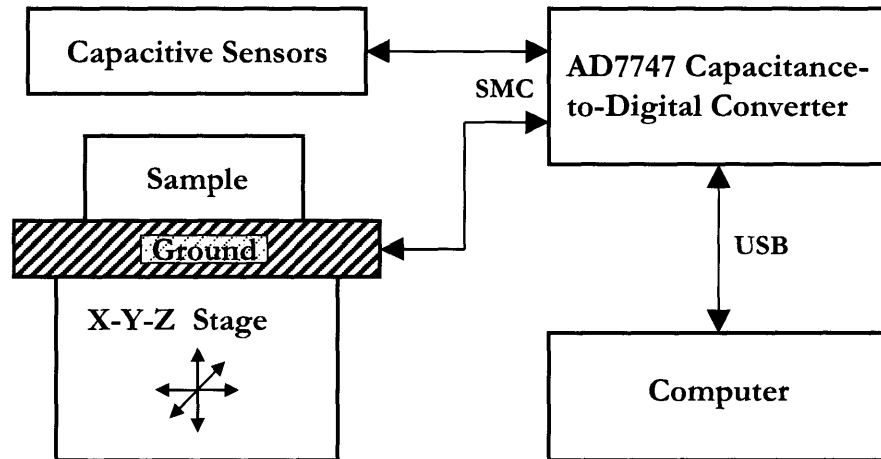


Figure 3-7: Experiment block diagram.

The experimental setup is summarized by the block diagram in Figure 3-7. Capacitive sensors were fabricated on a printed circuit board (PCB). These sensors interface with an Analog Devices AD7747 24-bit capacitance-to-digital converter [24]. The AD7747 has a dynamic input range of $\pm 8\text{pF}$ with 10fF precision and can measure a static capacitance of up to 17pF . The AD7747 interfaces with a computer through a USB port. Figure 3-8 is a photograph of the PCB capacitive sensors with one of the sensors connected to the AD7747 (shown to the left) through a SubMiniature Version C (SMC) cable. Shown in the figure are the top sides of six difference capacitive sensors. The bottom of the sensor board is shown in Figure 3-9.

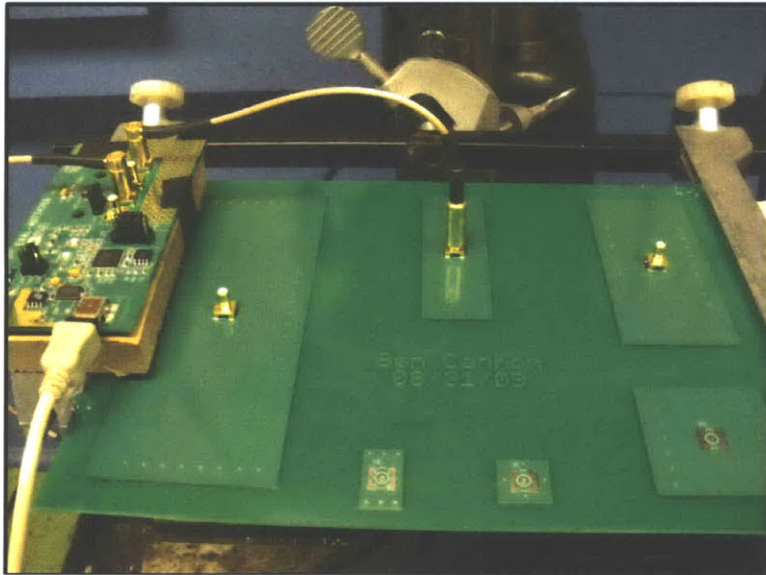


Figure 3-8: Capacitance detection electronics (top view). AD7747 capacitance-to-digital converter is shown to the left.

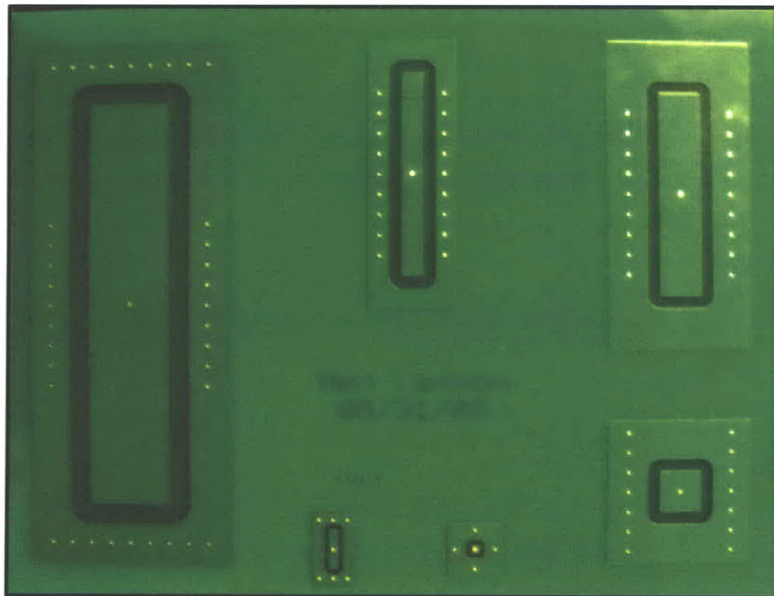


Figure 3-9: Various capacitive sensors (bottom view).

Each capacitive sensor is comprised of three electrodes: a sensor plate, a guard ring, and a top-side guard plate. The top-side guard plate is electrically connected to the guard ring by plated vias. The guard electrodes are driven at the

same voltage as the sensor plate to block stray fields from fringing off the top or sides of the sensor plate and to shunt the fields down toward the sample under evaluation. Figure 3-10 illustrates a side view of a capacitive sensor over a sample; plated vias are shown connecting the guard electrodes on the top and bottom layers of the FR-4 PCB substrate. The AD7747 measures changes in capacitance between the A—B terminal pair show in Figure 3-10 below as the sensor board is scanned laterally over the surface of the sample.

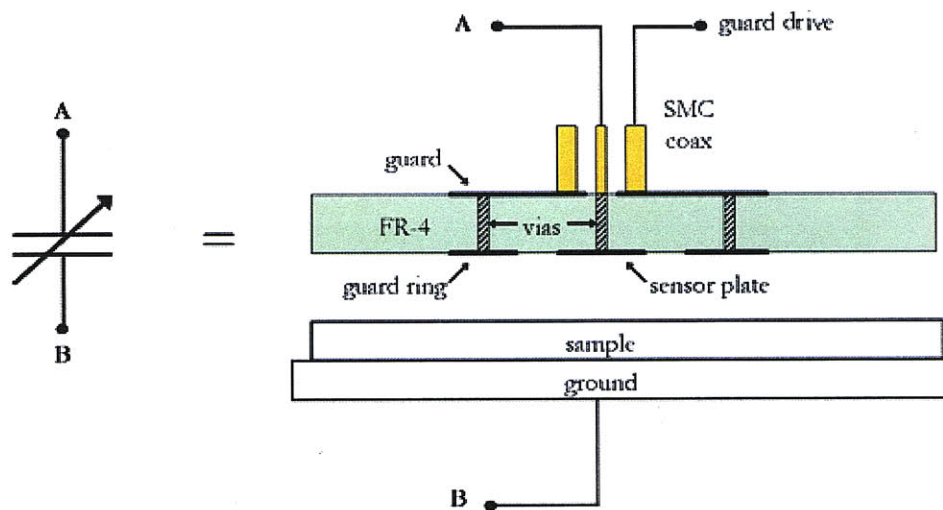


Figure 3-10: Capacitive sensor (side view).

Referring back to Figure 3-7, the grounded sample rests on an X-Y-Z stage. A milling machine stage with a motor-driven X-axis table feed and an absolute digital X-Y positioner accurate to 0.01mm was used to maintain X-Y precision. A fixed scan height was maintained by a manually-tuned Z-axis jack and set of digital Vernier calipers accurate to 0.01mm.

Samples were prepared to mimic the absorber layer trenches from the photomask that was simulated in the previous section. Aluminum was chosen as the sample material's substrate because it has an excellent electrical conductivity (approximately 10^7 [S/m]), it is low cost, and it is easily milled. Trenches of various

cross-sections were milled out of an aluminum bar with a cross-section of 13mm×102mm. Figure 3-11 shows photographs of the milled trench samples.

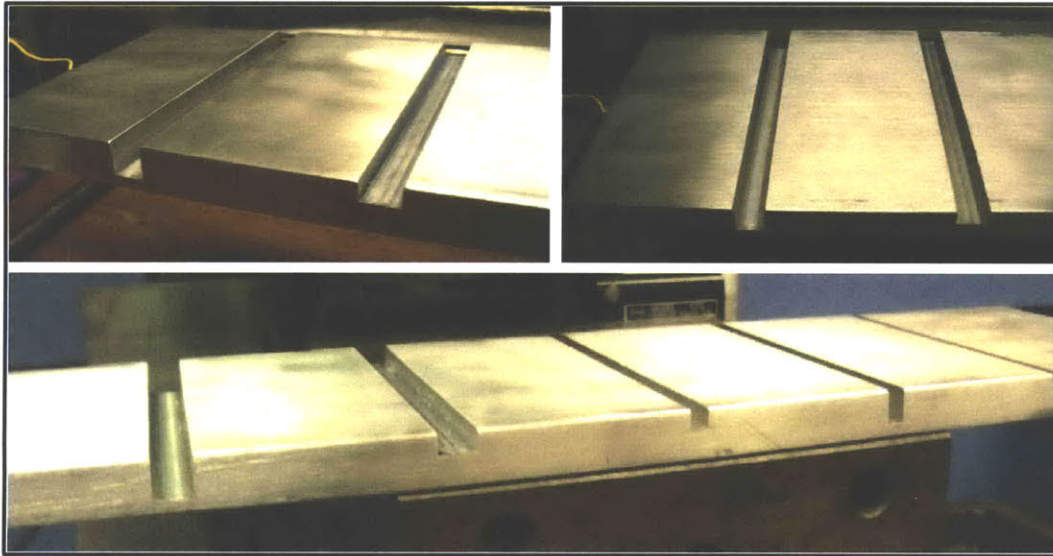


Figure 3-11: Trenches milled out of aluminum bar to represent absorber layer gaps of various depths and widths.

Sensors were mounted above the sample by clamping a PCB holder onto a vertical rod extending down from the mill spindle. Photographs of the entire experimental setup are shown in Figure 3-12 and Figure 3-13.

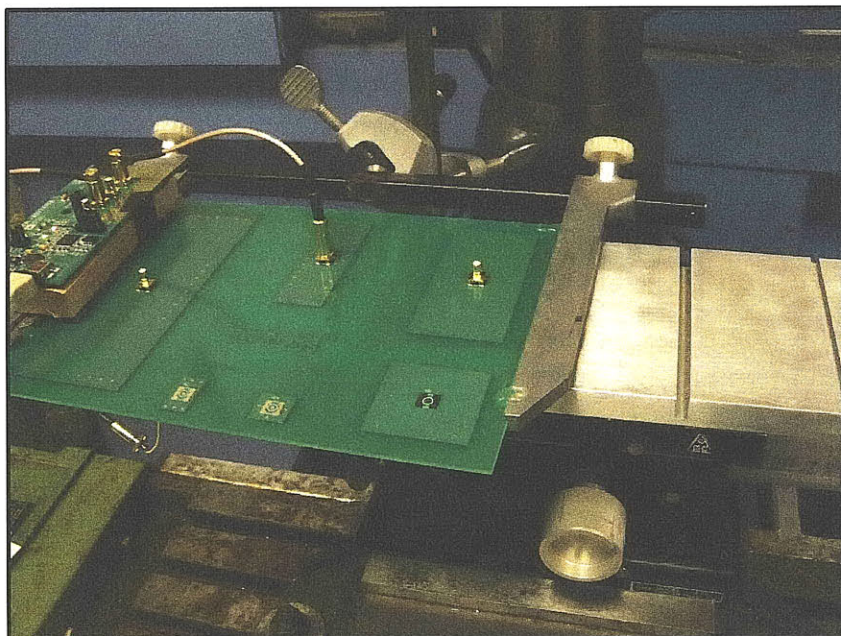


Figure 3-12: Laboratory setup (top view).

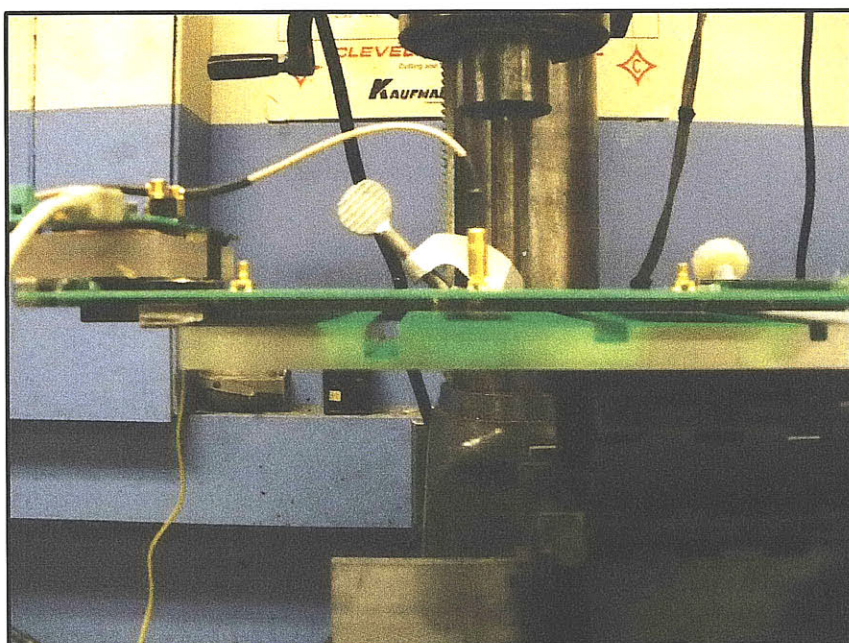


Figure 3-13: Laboratory setup (side view).

3.2.2 Experimental Results

Objects of various sizes, cross-sections, and material properties were placed in the trenches to see if a capacitive sensor would be capable of detecting the presence of the objects. These objects ran the length of the trench, and the sensor board was scanned at a fixed height over the surface of the aluminum in a direction perpendicular to the trench. Figure 3-14 illustrates a capacitive sensor scanning over a contaminant filled trench. Figure 3-15 shows photographs of the trench containing six different “contaminant” objects tested in the lab. The six objects that were tested included: a copper rod with square cross-section, a copper cylindrical rod, a stainless steel cylindrical rod, an aluminum cylindrical rod, a styrene plastic cylindrical rod, and polymer modeling clay rolled into a cylindrical rod. The trench, object, and sensor dimensions are summarized in Table 3-3.

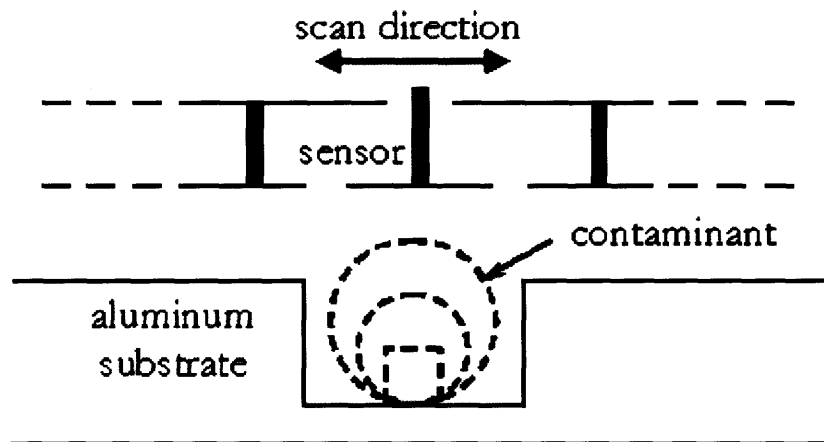


Figure 3-14: Capacitive sensor over contaminant filled trench. Contaminants of various shapes, sizes, and material properties were used.

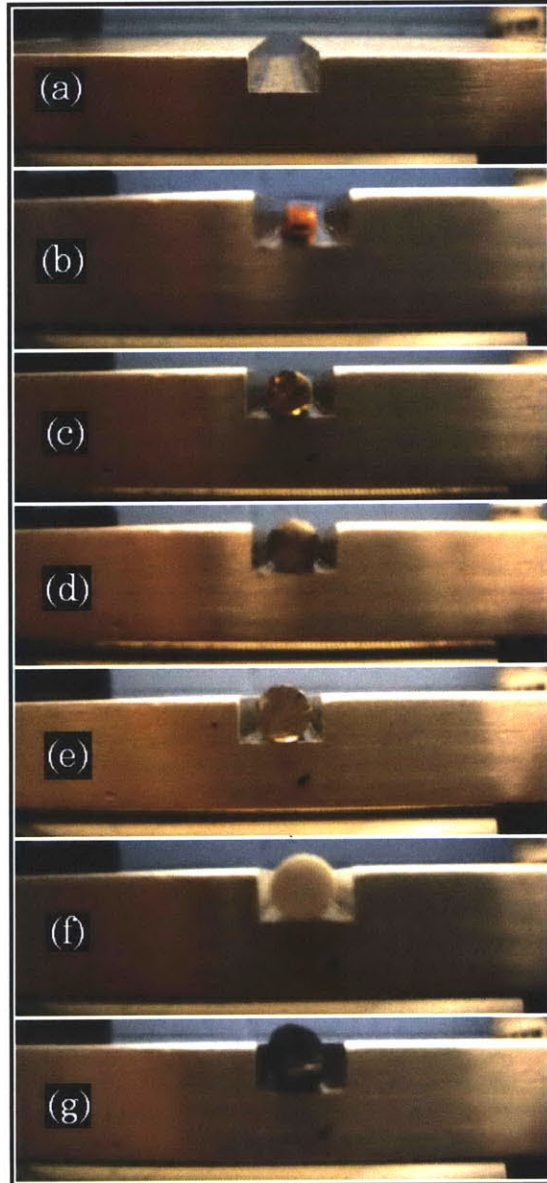


Figure 3-15: Cross-sections of various “contaminant” objects in 5.15mm×9.13mm trench. An empty trench is shown in (a) and the six objects that were tested include: (b) copper rod with square cross-section, (c) copper cylindrical rod, (d) stainless steel cylindrical rod, (e) aluminum cylindrical rod, (f) styrene plastic cylindrical rod, and (g) polymer modeling clay rolled into a cylindrical rod.

Table 3-3: Key geometric dimensions for laboratory experiment

Dimension	Length [mm]
trench depth	5.15
trench width	9.13
copper square rod side length	3.20
copper rod diameter	4.76
stainless steel rod diameter	5.57
aluminum rod diameter	6.36
plastic rod diameter	6.36
polymer clay rod diameter	6.90
sensor width	5.75
sensor length	50.5
sensor - guard ring spacing	3.15
guard ring width	5.25

The sensor board was scanned at two different fixed scan heights: 5.75mm and 7.75mm. The capacitance between the sensor and grounded aluminum sample vs. the sensor's horizontal position for each type of contaminant is shown in Figure 3-16 and Figure 3-17. For the highly conducting objects (copper, stainless steel, and aluminum), the family of curves clearly show that the larger the object is, the easier it is to detect. For the case that the sensor scans over the aluminum rod sample, the rod diameter is larger than the trench depth and the capacitance actually rises above its baseline values. For the insulating objects (styrene plastic and polymer modeling clay), both size and dielectric strength determine the sensor's ability to detect the object. The styrene plastic rod (whose dielectric constant is approximately 2.4) is the same diameter as the aluminum rod, but is much more

difficult for the sensor to detect. The polymer clay rod is only slightly larger than the plastic rod and is well-detected by the sensor. It is likely that the polymer modeling clay has a higher dielectric constant than the styrene plastic.

Comparing Figure 3-16 to Figure 3-17 shows how the sensor's ability to detect the objects degrades when the scan height is increased. For example, for the case that the trench is clean, and the sensors are scanned at a height of 5.75mm, there is a maximum change in the capacitance signal magnitude of 24% of the baseline value; however, when the scan height is increased to 7.75mm, the maximum change in capacitance signal magnitude drops to only 11% of the baseline value.

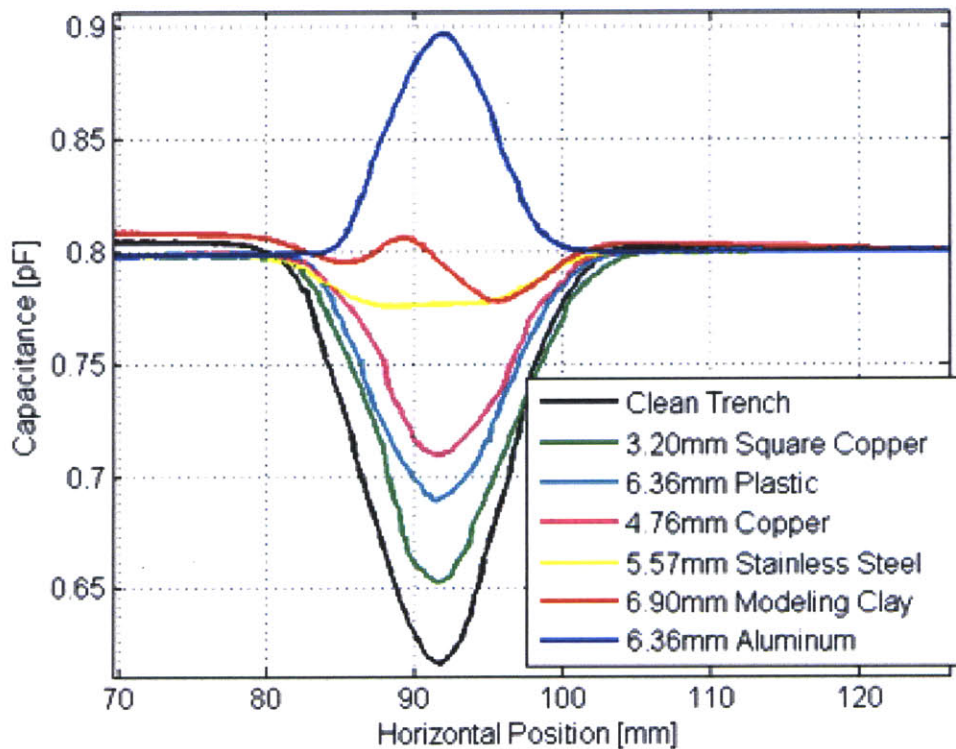


Figure 3-16: Sensor-Sample capacitance [pF] vs. horizontal position [mm] for 5.75mm scan height.

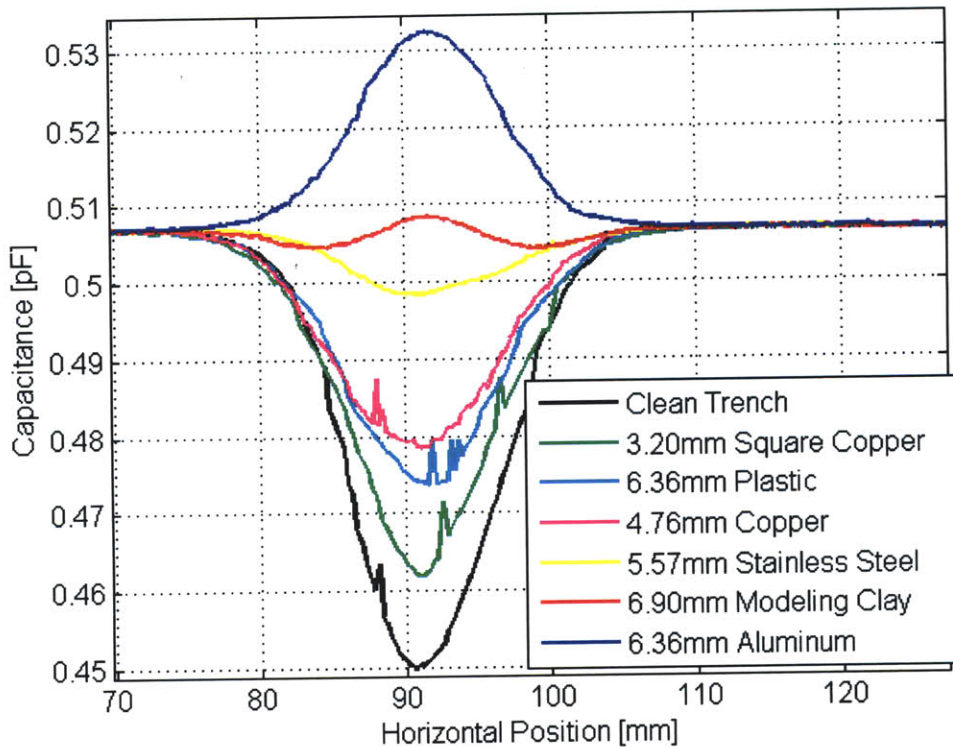


Figure 3-17: Sensor-Sample capacitance [pF] vs. horizontal position [mm] for 7.75mm scan height.

The same set of six different “contaminant” objects were then placed in a different trench with dimensions 9.1mm×8.8mm (depth × width). This deeper, narrower trench is expected to make it more difficult for the capacitive sensor to detect and distinguish the objects since a large portion of the electric field lines from the sensor will couple to the corners and upper sidewalls of the trench without detecting the objects; moreover, a much smaller fraction of the field lines will couple to ground through the object sitting in the bottom of the trench. Figure 3-18 provides photographs of the new set of samples. It is shown how the objects reside much deeper in the trench than in the previous case shown in Figure 3-15.

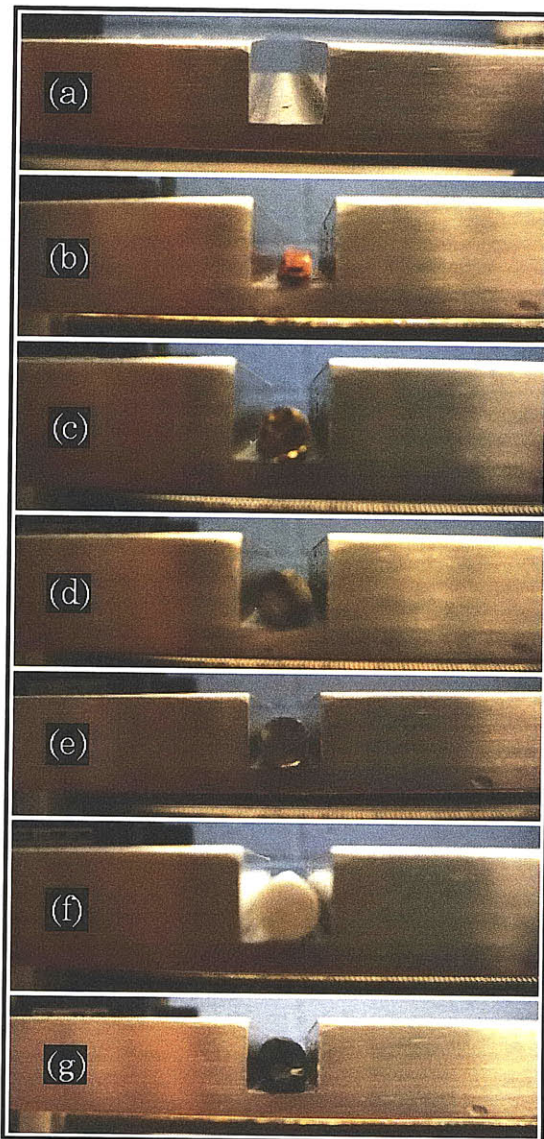


Figure 3-18: Cross-sections of various “contaminant” objects in 9.1mm×8.8mm trench. A empty trench is shown in (a) and the six objects that were tested include: (b) copper rod with square cross-section, (c) copper cylindrical rod, (d) stainless steel cylindrical rod, (e) aluminum cylindrical rod, (f) styrene plastic cylindrical rod, and (g) polymer modeling clay rolled into a cylindrical rod.

For the same fixed scan heights as before (5.75mm and 7.75mm), the capacitance between the sensor and grounded aluminum sample vs. the sensor’s horizontal position is plotted for each type of contaminant; results are summarized in Figure 3-19 and Figure 3-20. As expected, it is much more difficult for the sensor to locate and distinguish the contaminant objects in the deep trench. For example,

for the case that the object is a 6.36mm aluminum rod and the scan height is 5.75mm (shown in Figure 3-19(b)), the capacitance signal magnitude is only approximately 2.4% different than that of the clean trench; increasing the scan height to 7.75mm (Figure 3-20(b)) reduces this same percent difference in signal to about 1.2%.

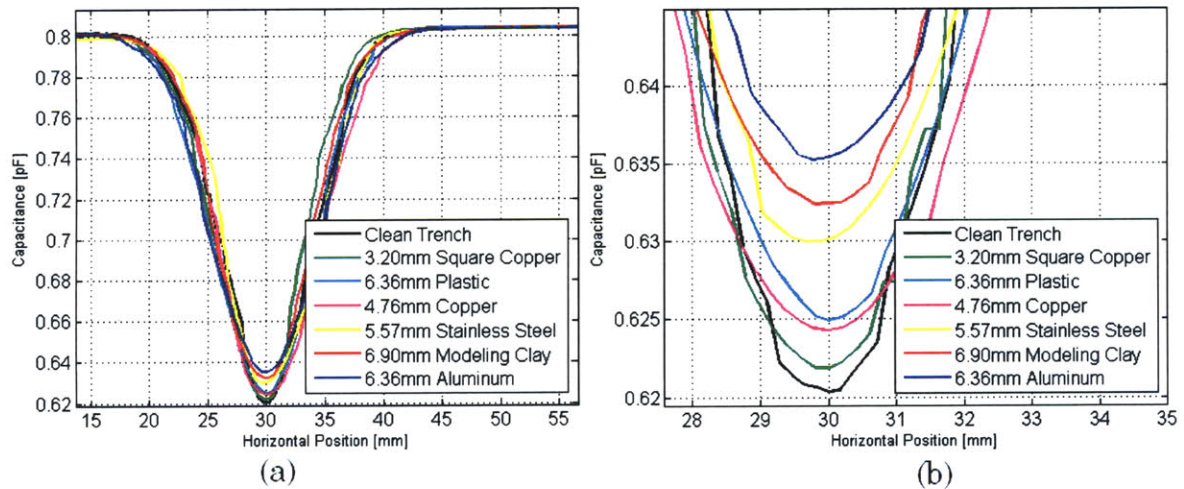


Figure 3-19: Sensor-Sample capacitance [pF] vs. horizontal position [mm] for 5.75mm scan height. Figure (b) is a zoomed-in version of the trough in Figure (a).

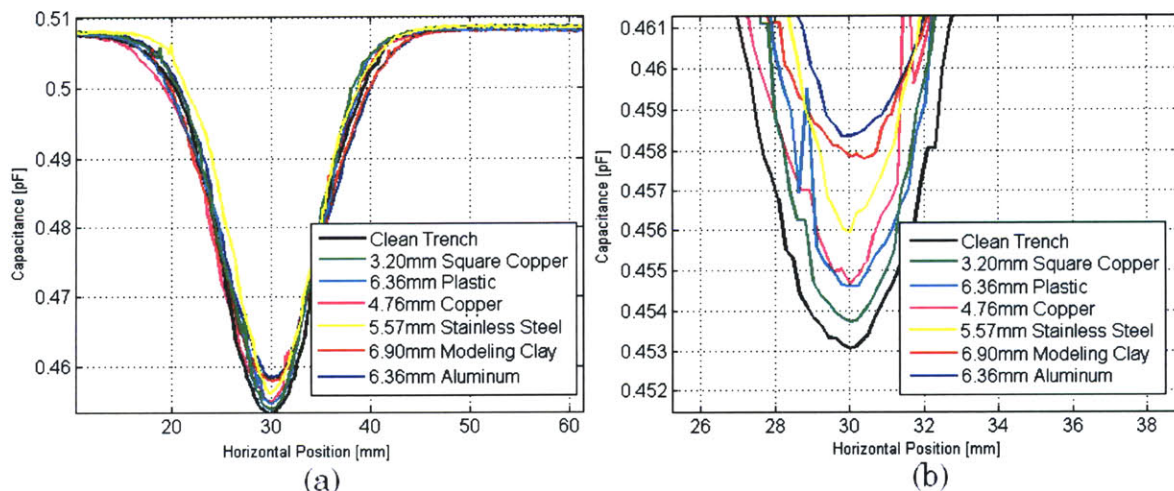


Figure 3-20: Sensor-Sample capacitance [pF] vs. horizontal position [mm] for 7.75mm scan height. Figure (b) is a zoomed-in version of the trough in Figure (a).

While the experiments in this section were not perfectly scaled replicas of the simulations from Section 3.1, they served to qualitatively confirm the results quite well. For example, in the COMSOL simulation shown in Figure 3-5, sensors are 50 nm wide and scanned at a fixed height of 100 nm over a gap that is 70nm×100 nm (depth × width). In the case where the sensors scan past an empty trench, the signal magnitude on sensor 1 drops to approximately 7% of its baseline value. The experiment that is most similar to this simulation is the case where the 5.75 mm wide sensor is scanned at a fixed scan height of 7.75 mm past a trench that is 5.15 mm×9.13 mm. For the case where the trench is empty, the signal magnitude on the sensor drops to approximately 11% of its baseline value. This is confirmation that when the simulation and experiment are run with similar aspect ratios, the changes in signal magnitudes are likely to be very similar.

The experiment is also capable of quickly providing insights to the limitations of EQS sensors for detecting objects in a deep trench. It was shown that when the six different contaminant objects were placed in a 9.1 mm×8.8 mm (depth × width) trench the sensors' ability to detect and distinguish the objects degraded severely compared to the case when the trench was 5.15 mm×9.13 mm. This is because a large portion of the electric field lines from the sensor couple to the corners and upper sidewalls of the deeper trench without passing through the contaminant objects. With a much smaller fraction of the field lines coupling to ground through the object in the bottom of the trench, it becomes very difficult to distinguish between different objects.

3.3 Low-Noise Pickup Circuitry

The results from the previous two sections demonstrate a clear need for low-noise circuitry to interface with the sensors. If a typical capacitive current signal fluctuates in response to features at a level that is smaller than the inherent noise levels present in the detection system, then detecting a feature through these signal variations is a lost cause. It is the goal of this section to demonstrate the need for low-noise pickup circuitry through a simple numerical example. The results of this chapter should provide the reader with a basic understanding of thermal noise issues when attempting to detect and amplify weak sensor signals.

Until this point, the COMSOL simulations for the detection of a contaminant particle stuck in an absorber layer gap (Section 3.1) have not considered noise of any sort. This section takes a look at the noise levels that might be encountered from two distinct sources:

- 1.) Noise due to the absorber layer resistance
- 2.) Noise due to the pickup circuitry required to monitor variations in sensor currents

This analysis is based on the same geometry that was evaluated in Section 3.1. The geometry is repeated below in Figure 3-21 for the reader's convenience, and key geometric and electrical properties are listed in Table 3-1 and Table 3-2.

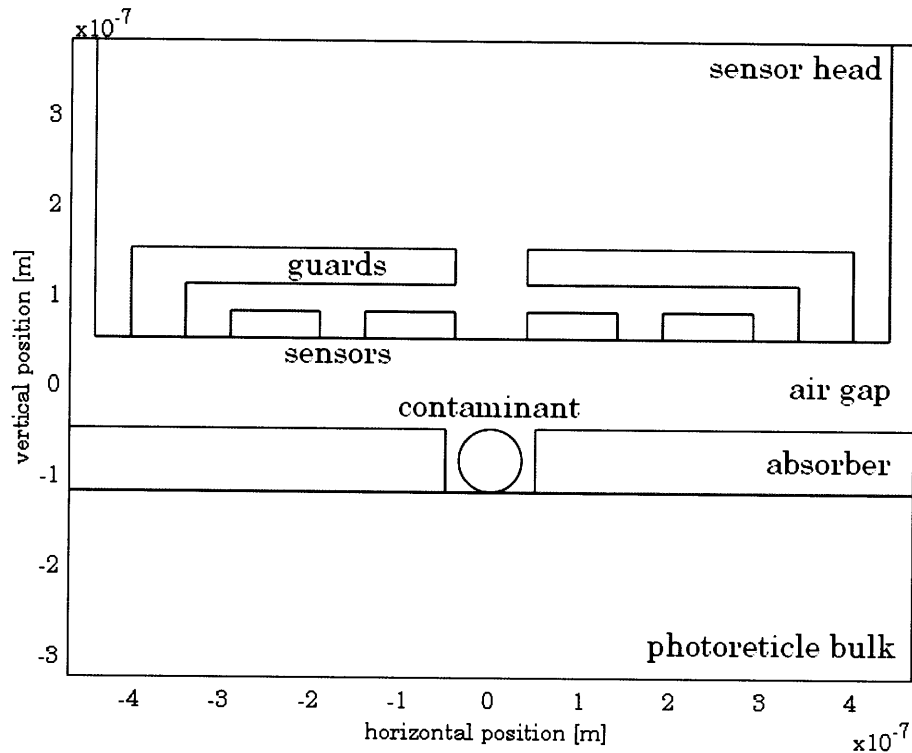


Figure 3-21: COMSOL geometry for contaminated EUVL photomask simulation.

The previous figure shows the sensor array at a height of 100nm above the absorber layer of the photomask. In this section, we will only consider the leftmost sensor (referred to as “sensor 1” in Section 3.1). As a reminder, each sensor is driven by a 1GHz sinusoidally varying voltage source with a peak amplitude of 1V. The two rightmost sensors and guard are driven 180° out of phase from the two leftmost sensors and guard so as to create a spatial square wave alternating in time. Since the sensor we are considering is guarded on the top and both sides by electrodes that are driven by a voltage at the same magnitude and phase, its electric field lines will be primarily vertical and couple to the absorber surface directly below it. This is illustrated in Figure 3-3.

We can then assume that the sensor-substrate interaction can be accurately modeled as a lumped air-gap capacitance, C_{air} , in series with an absorber layer resistance, R_{absorb} . In order to determine values for these parameters we first plot

the electric potential along the upper surface of the absorber layer. As shown in Figure 3-23, the magnitude of the potential at the absorber layer's upper surface under the sensor we are considering is approximately 0.6×10^{-14} [V]. Additionally, Figure 3-4 shows that the magnitude of the steady-state current per-unit-depth on sensor 1 is approximately 0.082 [A/m]

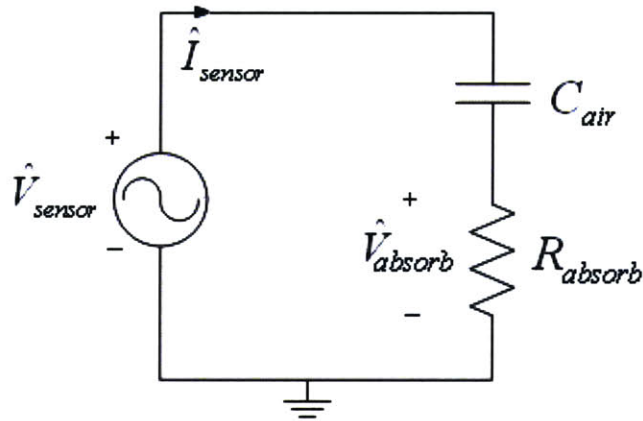


Figure 3-22: Lumped circuit model of EQS sensor-substrate interaction.

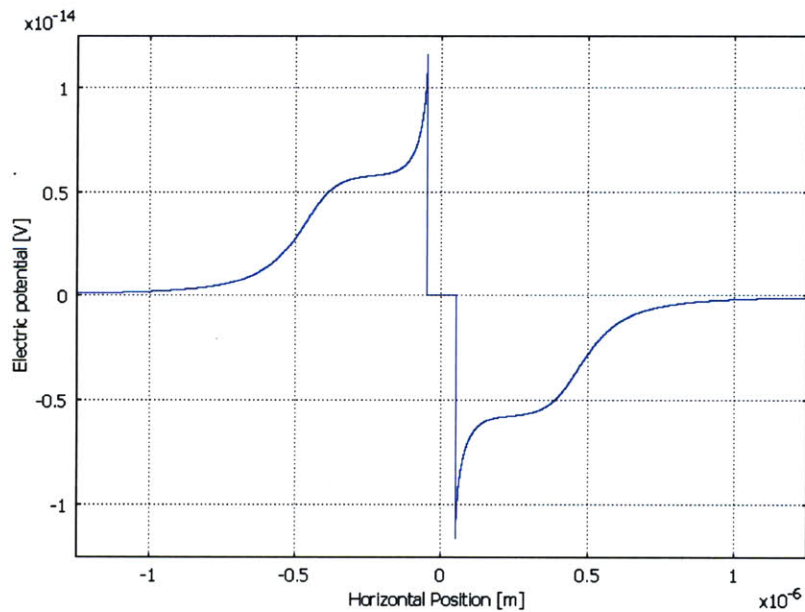


Figure 3-23: Electric potential [V] along absorber layer surface vs. horizontal position [nm] with sensor head centered over absorber layer gap.

Using lumped Port boundary conditions in COMSOL, we can get a value for the air-gap capacitance per-unit-depth C'_{air} :

$$Z'_{air} = -j12.3 [\Omega \cdot m] \quad (3.3)$$

$$C'_{air} = \frac{1}{j2\pi f Z'_{air}} = 1.29 \times 10^{-11} [\text{F}/m] \quad (3.4)$$

We can confirm this with:

$$\frac{\hat{V}_{sensor} - \hat{V}_{absorb}}{\hat{I}_{sensor}} = Z'_{air} = -j12.3 [\Omega \cdot m] \quad (3.5)$$

We then approximate the substrate resistivity as:

$$R'_{absorb} \approx \frac{\hat{V}_{absorb}}{\hat{I}_{sensor}} = 7.35 \times 10^{-14} [\Omega \cdot m] \quad (3.6)$$

The “primed” variables above represent parameters that are per-unit-depth. From this point on, a depth of 100nm is assumed to eliminate the “per-unit-depth” units from the parameters so that one can get realistic noise levels for the sensors. The sensor-substrate interaction then has the following numerical values:

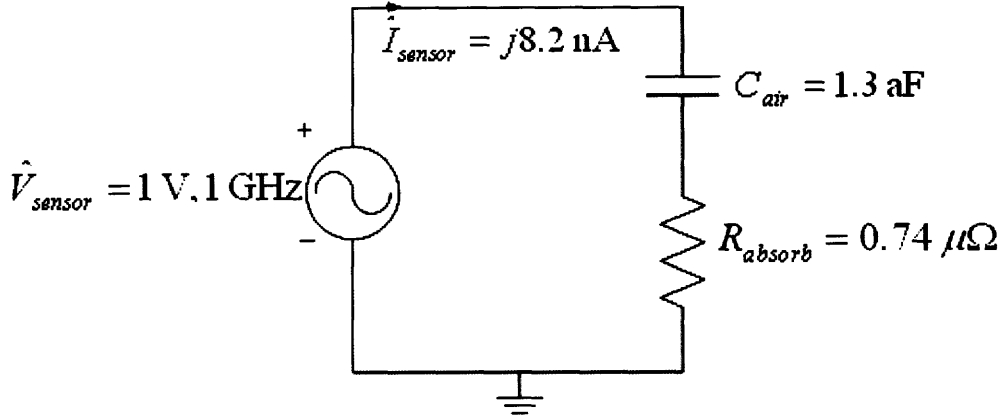


Figure 3-24: Sensor-substrate interaction parameters for depth of 100nm.

At 1GHz, the absorber layer resistance is *extremely* small compared to the capacitive air-gap impedance; consequently, the sensor current leads the sensor voltage by approximately 90° . Given this extremely small value for R_{absorb} , it can be considered negligible and is not likely to contribute an appreciable amount of thermal noise. For completeness, though, analysis will be carried out with R_{absorb} , included, and it will be shown that thermal noise from the absorber layer losses are negligible.

From this point on we will consider only the magnitudes of the complex current and voltage when compared to RMS noise levels. Therefore, the complex “hats” will be dropped off the current and voltage variables, and it will be assumed that we’re dealing strictly with the magnitudes of these complex quantities.

As it stands in the circuit of Figure 3-24, we have no mechanism for detecting changes in the sensor current magnitude, ΔI_{sensor} , as it scans past a feature. One possible solution is to couple to the sensor current with a current-step-up transformer (# primary windings > # secondary windings) and then feed this into some type of current-to-voltage amplifier. We ultimately want to detect changes in the magnitude, or envelope, of our sensor current. Since our sensor excitation is at 1GHz, we need to demodulate our waveform by this carrier frequency and then low-

pass filter the signal over some bandwidth, Δf [14]. By low-pass filtering, we allow ourselves to scan the sensors as slowly as we'd like, and as quickly as the corner frequency of the LPF passband will permit. In this analysis, we'll assume a bandwidth of 1MHz. Figure 3-25 provides a schematic view of this sensor current detection circuit.

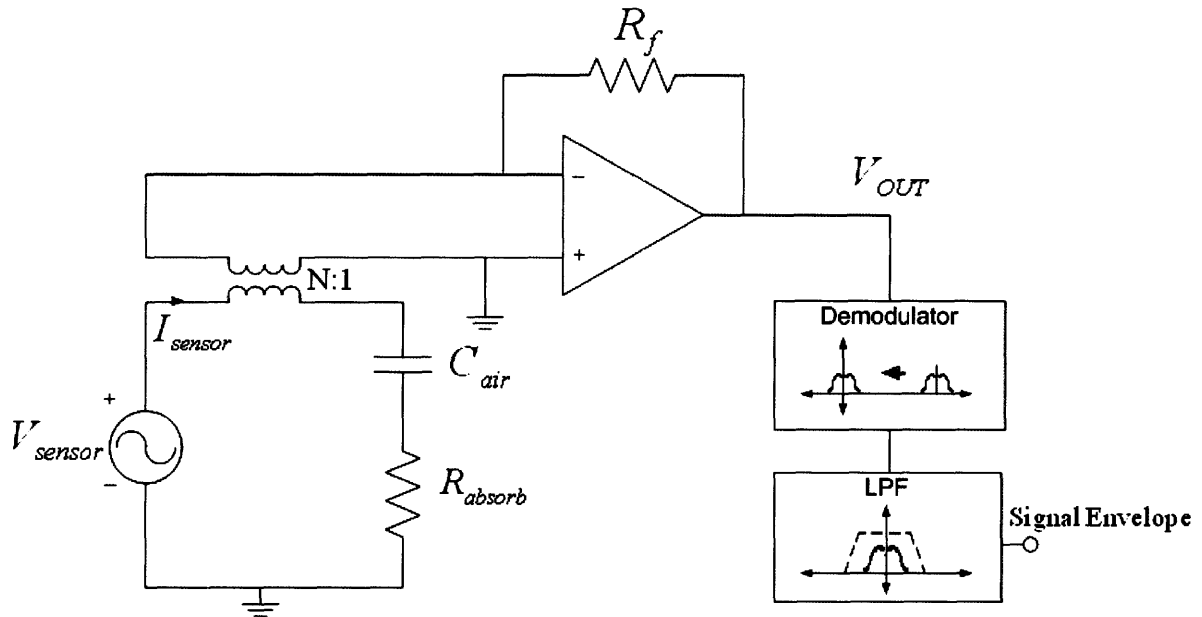


Figure 3-25: Sensor signal detection circuit.

We are now in a position to begin evaluating the noise in our circuit. Rather than considering the noise at the output of the LPF stage, we should first consider the signal-to-noise ratio (SNR) at V_{OUT} . We need a reasonable SNR at V_{OUT} if we are ever going to detect signal fluctuations at the output of the LPF.

As a first step in the noise analysis, it is assumed that the transformer and op-amp are both ideal. This allows for a “best case” SNR at the output, where the noise considered is only the thermal noise due to resistors in the circuit. The thermal noise due to a resistor is white, meaning its power spectrum is flat over all frequencies [25, 26]. When performing noise analysis we can replace the ideal

resistors in Figure 3-25 with ones that contain thermal noise generators, as seen in Figure 3-26,

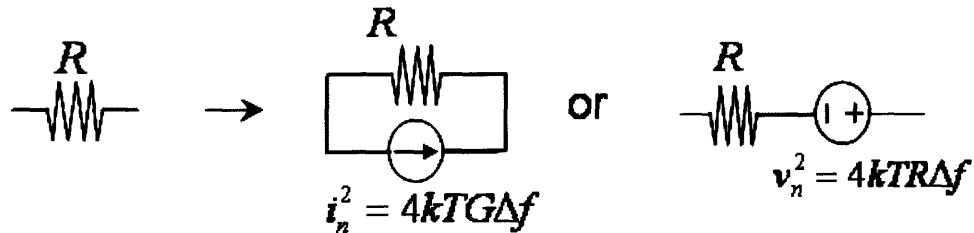


Figure 3-26: Resistor thermal noise model [26].

where $G = 1/R$. $\frac{\bar{i}_n^2}{\Delta f}$ and $\frac{\bar{v}_n^2}{\Delta f}$ are the current and voltage variances (mean square) per hertz bandwidth representing the power spectral density (PSD) of the noise ($4kTG$ and $4kTR$ have units of $[A^2/Hz]$ and $[V^2/Hz]$, respectively). All noise analysis in this document is performed at a temperature of 300K.

We can get a total RMS noise level at V_{OUT} by the linear superposition of the two uncorrelated noise generators due to R_{absorb} and R_f . We'll first turn off the R_f noise generator and find \bar{v}_{OUT1}^2 , the contribution to the output noise from R_{absorb} . The schematic for this circuit is shown in Figure 3-27.

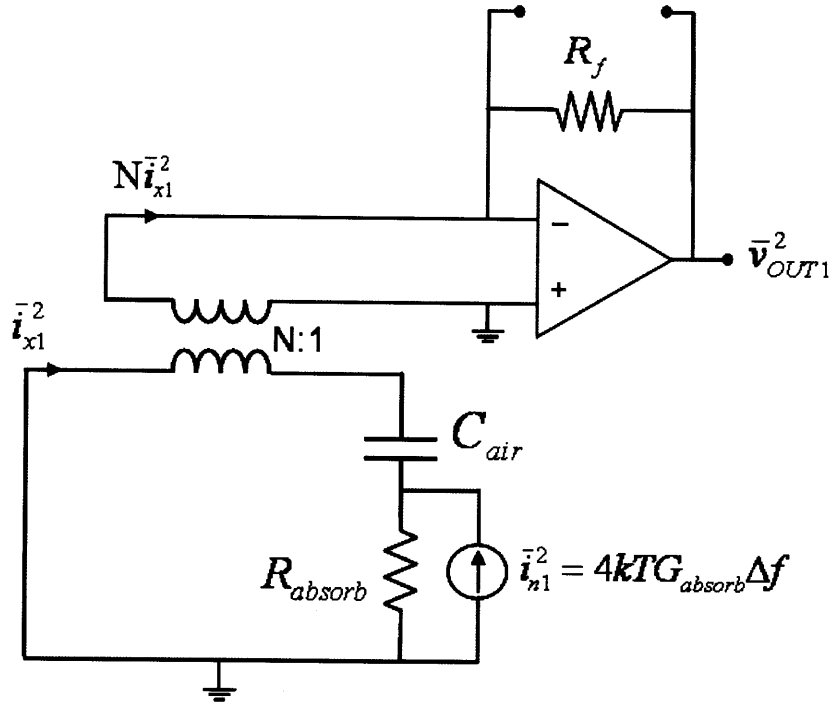


Figure 3-27: Circuit for evaluating output noise due to R_{abbrev} only.

In this case, the output is given by:

$$\bar{v}_{OUT1}^2 = \left| -N(\bar{i}_{n1}) \left(\frac{R_{abbrev}}{R_{abbrev} + \frac{1}{j\omega C_{air}}} \right) R_f \right|^2 \quad (3.7)$$

$$\bar{v}_{OUT1}^2 = \left| -N^2(4kTR_{abbrev}\Delta f) \left(\frac{j\omega C_{air}}{1 + j\omega C_{air}R_{abbrev}} \right)^2 R_f^2 \right|^2 \quad (3.8)$$

Next, we turn off the R_{abbrev} noise generator and find \bar{v}_{OUT2}^2 , the contribution to the output noise from R_f . This is shown in Figure 3-28. Here, R_{abbrev} and C_{air} get reflected across the transformer by the square of the turns ratio into a lumped impedance Z_{in} . This is shown in Figure 3-29.

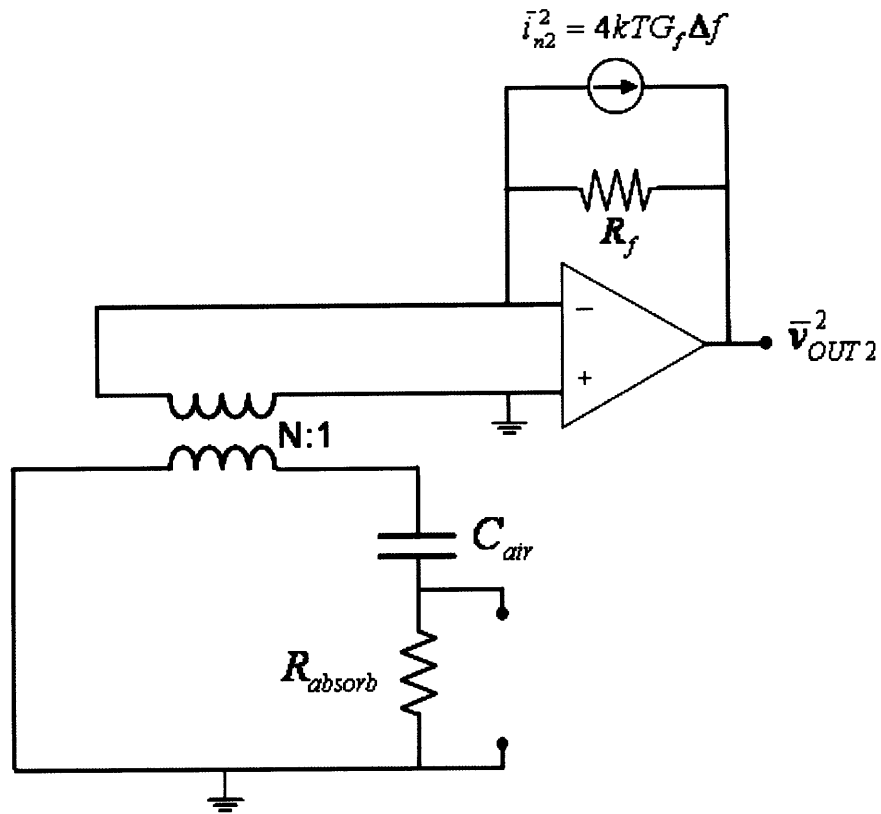


Figure 3-28: Circuit for evaluating output noise due to R_f only.

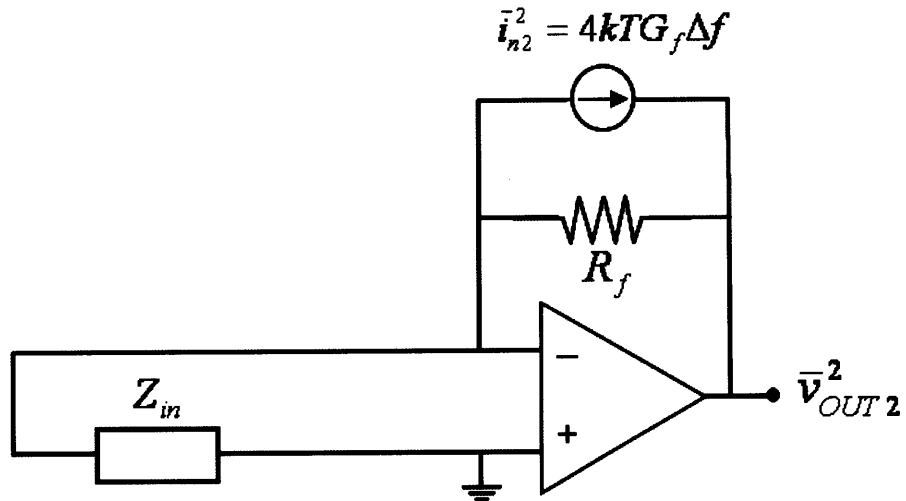


Figure 3-29: R_{absorb} and C_{air} transformed into impedance Z_{in} .

In this case the equivalent transformed impedance is given by:

$$Z_{in} = N^2 \left(\frac{1 + j\omega C_{air} R_{absorb}}{j\omega C_{air}} \right) \quad (3.9)$$

Assuming the op-amp is ideal:

$$\bar{v}_{n2} = -\frac{v_-}{Z_{in}} + \frac{-Av_- - v_-}{R_f} \approx \frac{\bar{v}_{OUT2}}{A} \left(\frac{1}{Z_{in}} + \frac{A}{R_f} \right) \quad (3.10)$$

In this limit we can assume $A \rightarrow \infty$ and thus:

$$\frac{A}{R_f} \gg \frac{1}{Z_{in}} \quad (3.11)$$

In this limit then:

$$\bar{v}_{OUT2} = \bar{v}_{n2} R_f \quad (3.12)$$

$$\bar{v}_{OUT2}^2 = |4kTG_f \Delta f R_f^2| \quad (3.13)$$

$$\bar{v}_{OUT2}^2 = |4kTR_f \Delta f| \quad (3.14)$$

Applying superposition to the two uncorrelated noise sources:

$$\frac{\bar{v}_{OUT-NOISE}^2}{\Delta f} = \frac{\bar{v}_{OUT1}^2}{\Delta f} + \frac{\bar{v}_{OUT2}^2}{\Delta f} \quad (3.15)$$

$$\frac{\bar{v}_{OUT-NOISE}^2}{\Delta f} = \left| -N^2(4kTR_{absorb}) \left(\frac{j\omega C_{air}}{1 + j\omega C_{air} R_{absorb}} \right)^2 R_f^2 \right| + |4kTR_f| \quad (3.16)$$

Let's assume that $R_f = 10k\Omega$ so that we can plot and compare the output noise PSDs due to R_{absorb} and R_f .

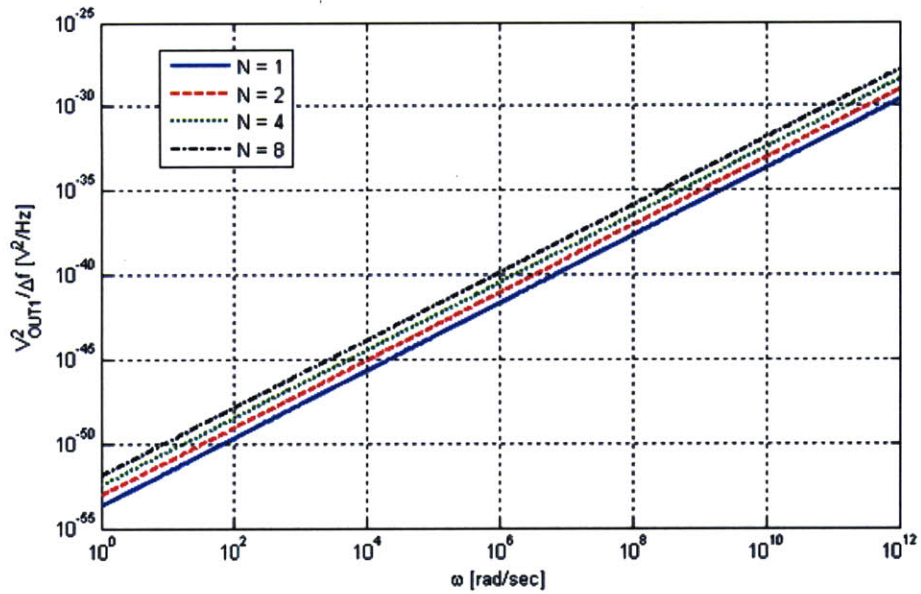


Figure 3-30: Output voltage noise PSD due to R_{absorb} vs. ω for various turns ratios N .

As shown previously, the noise contribution from the feedback resistor is independent of N .

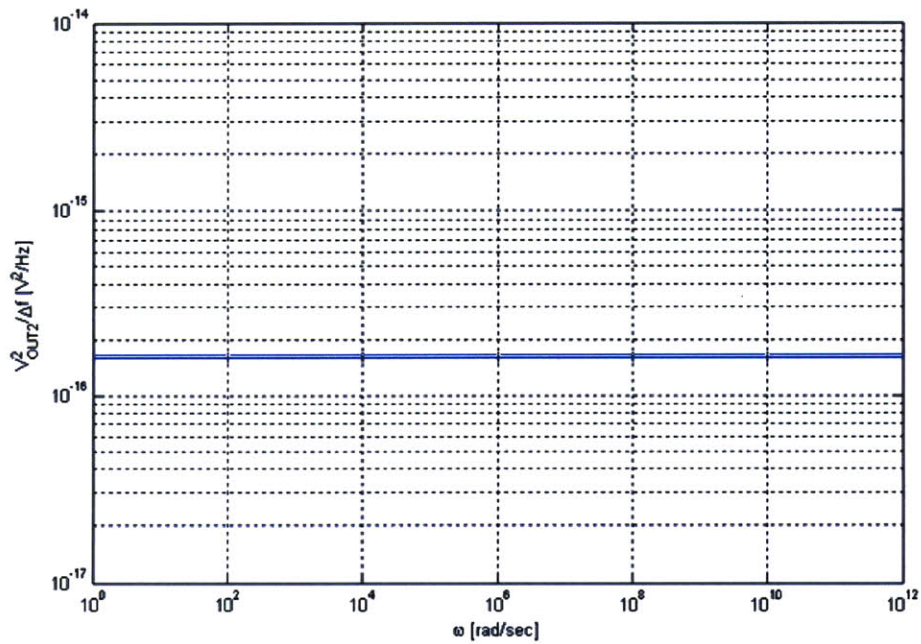


Figure 3-31: Output voltage noise PSD due to R_f vs. ω (independent of N).

As was expected, it is clear that the output noise comes primarily from the feedback resistor, and the noise due to R_{absorb} is negligible by several orders of magnitude. This makes sense because R_{absorb} is extremely small compared to R_f . There is then no inherent battle with noise from the absorber layer resistance. If we considered the voltage noise due to R_{absorb} over 1MHz bandwidth *in the drive circuit alone*, we would get an RMS voltage noise level of 1.38×10^{-10} [V]. With a voltage drive level of 1V, the signal would be approximately 7×10^9 times larger than the noise.

We are now in a position to evaluate a SNR at V_{OUT} . Integrating the total noise PSD at V_{OUT} over 1MHz bandwidth (assuming first-order roll off after the 1MHz corner) gives a total RMS voltage noise level of:

$$\bar{v}_{OUT-NOISE} = \sqrt{4kTR_f \cdot 1MHz \cdot \frac{\pi}{2}} = 16.1 [\mu V] \quad (3.17)$$

We know that variations in the output signal ΔV_{OUT} go as follows:

$$|\Delta V_{OUT}| = |-N(\Delta I_{sensor})R_f| \quad (3.18)$$

where ΔI_{sensor} is the magnitude of the fluctuation in the sensor current magnitude as it scans past a feature. Looking back at the current response for s (Figure 3-4)—in the event that it scans over an empty trench in the absorber pattern—the signal will fluctuate on the order of $\Delta I_{sensor} \approx 0.6$ [nA]. Consequently the signal magnitude at V_{OUT} is:

$$|\Delta V_{OUT}| = 6 \cdot N [\mu V] \quad (3.19)$$

We express a signal-to-noise ration in the 1MHz passband as:

$$SNR = \frac{|\Delta V_{OUT}|}{\bar{v}_{OUT-NOISE}} \quad (3.20)$$

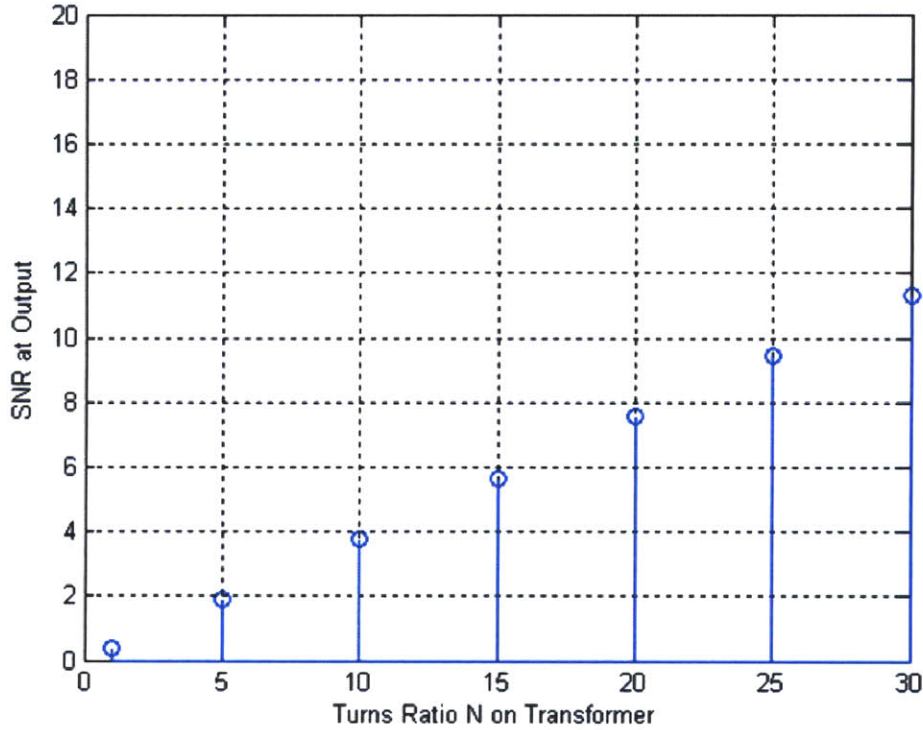


Figure 3-32: SNR at output for various turns ratios.

It is clear from Figure 3-32 that we need an appreciable amount of turns on the transformer primary to overcome the thermal noise caused by R_f ($N = 10$ turns gives an SNR of approximately 4:1). It should be noted that driving the sensors at 1V zero-to-peak amplitude can be considered conservative with regards to breakdown and field emissions. For a 100nm air gap, it is likely that field emissions will occur far before electric breakdown [27, 28]. Electron field emissions in pure metals occur at 10^9 [V/m], whereas our sensors are driven at 1V across a 100nm gap [27, 28]. It should be possible to drive the sensors at 10V across this 100nm gap and still be a factor of 10 away from FE. Increasing the drive level will increase the signal magnitude linearly without affecting the noise level (again,

assuming the transformer is ideal). Figure 3-33 shows SNR vs. turns ratio for various drive levels.

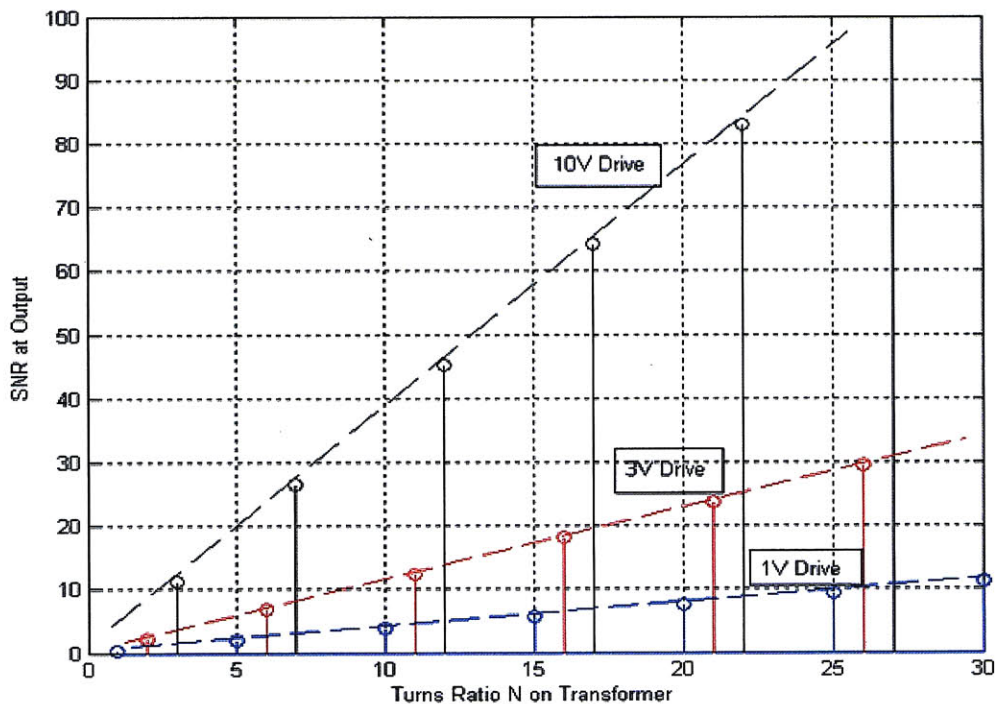


Figure 3-33: SNR at output for various turns ratios for 1V, 5V, and 10V sensor drive at 1GHz drive frequency.

Another way to increase the SNR linearly is to increase the drive frequency. Since the sensor current is dominated by the air-gap capacitance, C_{air} , the sensor current is approximately:

$$\hat{i}_{sensor} \approx j\omega C_{air} \hat{V}_{sensor} \quad (3.21)$$

Figure 3-34 is the same plot as Figure 3-33 but at an increased drive frequency of 5GHz. As expected, a 5× increase in SNR is observed.

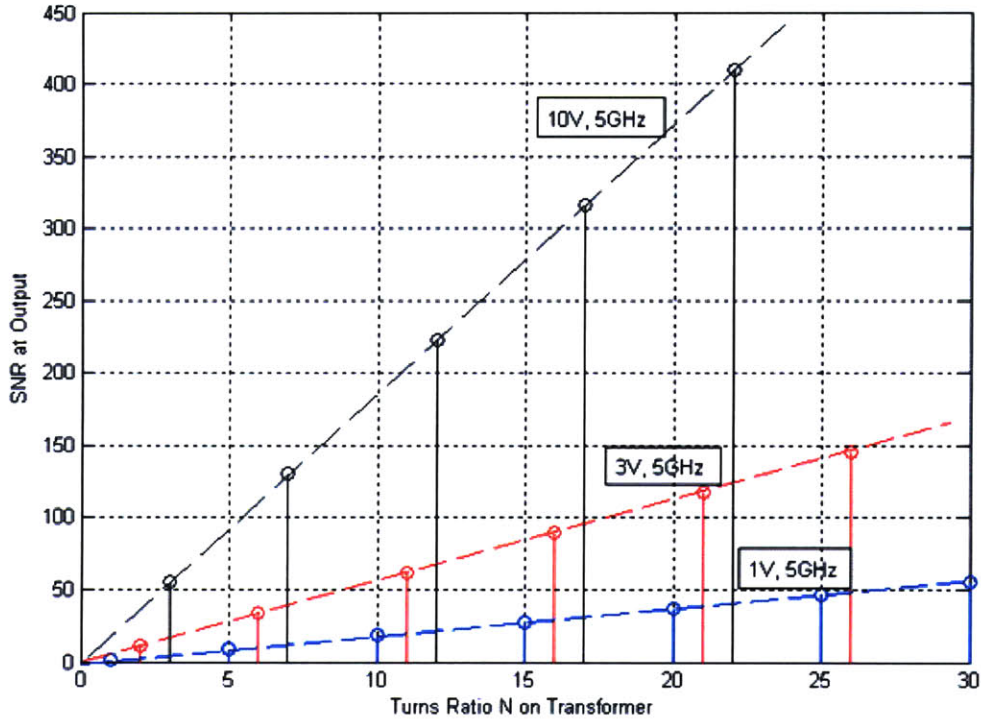


Figure 3-34: SNR at output for various turns ratios for 1V, 5V, and 10V sensor drive at 5GHz drive frequency.

It is important to reiterate that this analysis only takes into account the thermal noise due to R_{absorb} and R_f . A more complete analysis of this topology would take into account a non-ideal transformer and a non-ideal op-amp. This analysis does not take into account the noise in the demodulation and filtering circuitry. Such an analysis should indeed be performed when more quantitative details are known about the transformer and low-noise amplifier to be implemented. One should also realize this is only one possible (and rather unlikely due to its wideband nature) circuit topology for detecting the sensor current response. Nonetheless, it demonstrates the extreme importance of having low-noise pickup circuitry to interface with the sensor array. An investigation into other possible low-noise pickup circuits could serve as a topic of future research for this research project. In the example presented in the chapter, variations in the sensor current in response to features were on the order of less than 1 nA. Detecting such a small current

require a very narrowband, ultra-low-noise amplification circuit interfacing with the sensors. For a deeper understanding of the operation of narrowband low-noise amplifiers, [29] is a suggested reading.

Additionally, this analysis assumes that the sensor head scans at a fixed height of 100 nm. One should consider the noise that is introduced by mechanical vibrations that might cause the sensor's scan height to fluctuate relative to the sample. Such vibrations need to be bounded to enable good imaging.

4 Sensor Signal Inversion through a Radial Basis Function Artificial Neural Network

This chapter concerns the inversion of EQS sensor signal response data for the purpose of predicting feature/defect profiles. To this point, only the forward problem of determining sensor signal responses for a given feature/defect have been considered. These forward problems are well-posed in that for a given geometry there exists a unique EQS solution that depends continuously on the physical and electrical properties of the geometry. The inverse problem is then to infer information about a geometry (material properties, feature sizes/locations, etc.) that caused a measured sensor signal[12]. Inverse problems are in general ill-posed in that, for a given measured sensor signal, there does not necessarily exist a unique solution that depends continuously on the physical and electrical properties of the network.

The goal of this chapter is to predict the dimensions (depth and width) of a sub-micrometer scale trench in doped silicon based upon a measured transimpedance between two sensors in a coplanar array that is scanned laterally over the surface of the silicon. This is an example of the type of inverse problem that might be encountered in an EQS array microscope and one possible approach to its solution. To solve the inverse problem, a radial basis function artificial neural network is trained with a small database of COMSOL simulation results to perform

the forward function of mapping trench dimensions into a measurable transimpedance between two sensors in the array. Once the artificial neural network is trained, it can be used in an iterative error-minimizing inversion routine. The chapter describes how the inverse EQS problem is solved in this manner.

4.1 Simulating the Forward Problem

The evaluated geometry is shown in Figure 4-1 with key geometric and electrical parameters provided in Table 4-1 and Table 4-2. Figure 4-1 shows a sensor head containing six sensors and two guards at a fixed height of 50 nm over a doped silicon bulk. In the doped silicon bulk there exists an air-filled trench that can take on a variety of widths and depths.

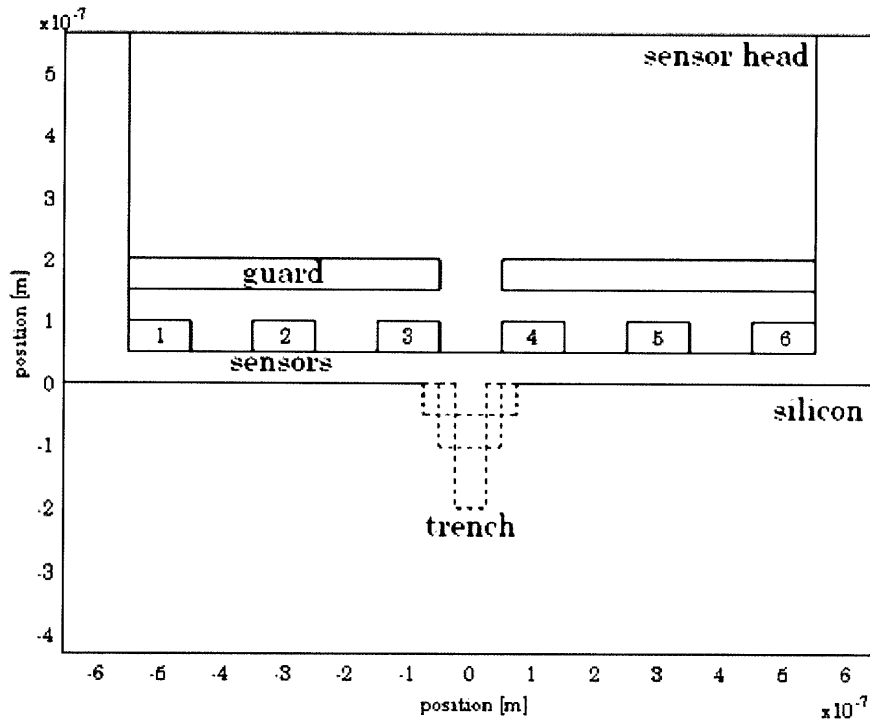


Figure 4-1: COMSOL geometry for locating trenches of various dimensions (depth and width) in doped silicon with an array of coplanar EQS electrodes.

Table 4-1: Key geometric dimensions for trench simulations

Dimension	Length [nm]
air gap (sensor scan height)	50
sensor width	100
sensor height	50
total sensor head width	1100
trench depth	50 – 200
trench width	40 – 120

Table 4-2: Electrical parameters used in FEM simulation

Parameter	Value
sensor head relative permittivity (SiO ₂)	3.9
silicon relative permittivity	11.8
silicon conductivity	0.005 [S/m]
sensor conductivity	PEC
sensor frequency	7.62 [MHz]

Electrodes on the left half of the sensor head are driven by a 7.62MHz sinusoidal voltage source with peak amplitude of 1V. This frequency was chosen because it is on the order of the charge relaxation break frequency of the semiconducting silicon bulk. Although this analysis only considers the magnitude of the impedance between sensors in the array, choosing a drive frequency on the order of the charge relaxation time of the bulk can provide interesting phase information as well. With the intrinsic conductivity of silicon being approximately

4.3×10^{-4} [S/m], the silicon in the simulation with conductivity of 5×10^{-3} [S/m] represents a weakly doped substrate. Electrodes on the right half of the sensor head are short-circuited to ground. Because each sensor/guard is treated as a perfect electrical conductor (PEC), we can assume there are no fields inside these regions and thus treat them as electric potential boundary conditions. “Port” boundary conditions are used in COMSOL to calculate lumped terminal parameters for the system. The particular parameter of interest is the mutual transimpedance between sensor 2 and sensor 5 (sensor indices shown in Figure 4-1).

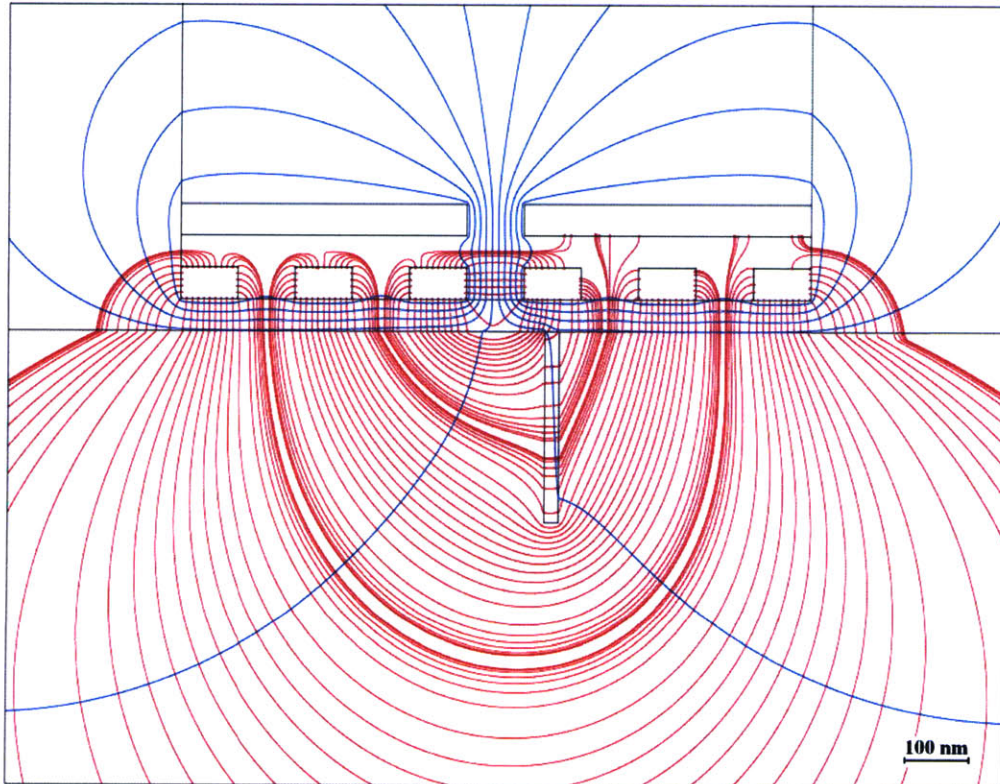


Figure 4-2: COMSOL simulation results with 300nm×25nm trench positioned 100nm right of center. Red streamlines are electric field lines and the blue contours represent equipotentials (lines of constant voltage). For simplicity, fields from guard electrodes are not shown.

Figure 4-2 shows an electric field streamline plot from COMSOL reacting to a high aspect ratio trench (300nm×25nm) in the silicon bulk. Electric fields from

sensor 2 are shunted into the silicon bulk by guarding effects from sensor 1, sensor 3, and the top-side guard. These field lines can be seen bending and reacting to the presence of the air-filled trench. The presence of the air-filled trench shows up as variations in both the magnitude and phase of the mutual transimpedance between sensor 2 and sensor 5 as the sensor head scans past the trench. Figure 4-3 provides families of transimpedance responses vs. sensor head position for trenches of various depths and widths. Figure 4-3(a) shows a family of responses for trenches of varying depths with width fixed at 50nm, and Figure 3-4(b) shows a family of responses for trenches of varying widths with depth fixed at 100nm.

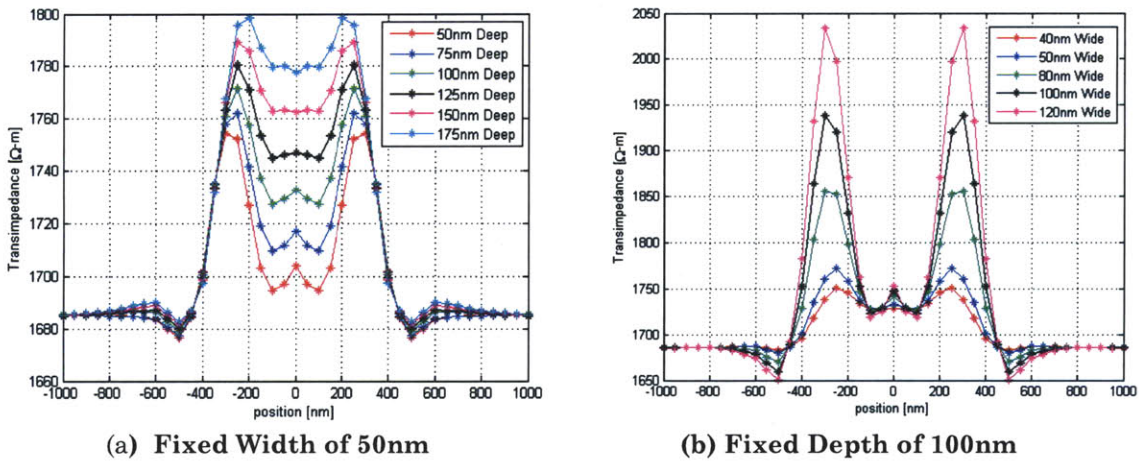


Figure 4-3: Sensor 2 – Sensor 5 transimpedance [$\Omega \cdot m$] vs. sensor head position [nm] for trenches of various depths and widths. In this case impedance has units of [$\Omega \cdot m$] because the simulation is performed on a 2D solver. Figure (a) shows a family of responses for trenches of varying depths with width fixed at 50nm, Figure (b) shows a family of responses for trenches of varying widths with depth fixed at 100nm.

4.2 Solving the Inverse Problem

Looking at the curves in Figure 4-3, one can see that there exists some monotonic dependencies of impedance on trench depth and impedance on trench width. For example, qualitatively speaking, it's clear in Figure 4-3(a) that the impedance

increases with trench depth and that the trenches are most easily distinguished from one another when they are nearly centered under the sensor head.

To solve the inverse problem of predicting trench depth and width based on a given impedance curve like those shown in Figure 4-3, one can imagine building a giant database of the results for many different trenches and traversing that database for a match based on some error minimization function. A more efficient method would be to train a function-approximation device to predict the forward model through some type of functional mapping from input space (trench dimensions) to output space (impedance response) [30, 31]. This device can then be used to replace the large database of results. This is the method that will be used in this chapter to solve the inverse trench problem.

The specific algorithm that was chosen to invert the measured sensor data into predicted trench dimensions is illustrated in the block diagram in Figure 4-4. A radial basis function artificial neural network (RBF-ANN) is trained to accurately predict the forward function of mapping trench dimensions into a measurable sensor transimpedance [31]. This RBF-ANN is then fed an initial guess for the trench dimensions, compares the results to the measured transimpedance response, and then iterates through a sum of squares error minimization routine. This iterative routine then converges to a value for trench dimensions that minimizes the error between the RBF-ANN forward model and the measured data. The training database is built using COMSOL simulation results.

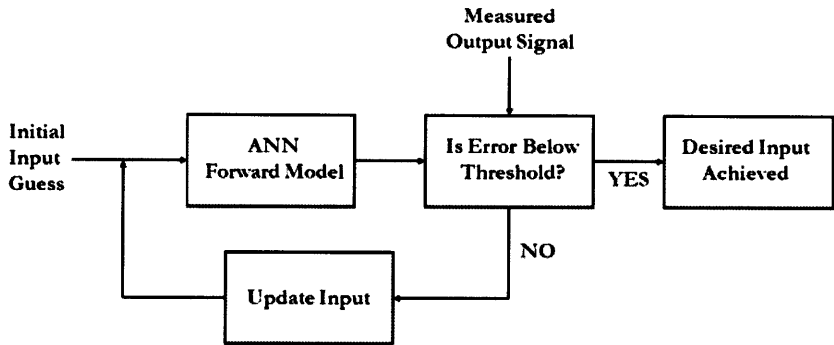


Figure 4-4: Iterative signal inversion block diagram [31].

4.2.1 Artificial Neural Networks (ANNs): Training and Operation

An artificial neural network is a mathematical model consisting of an interconnected cluster of “neurons,” or nodes, that attempt to approximate a function through weighted combinations of the neurons’ activation functions. In the case of an RBF-ANN, the neuron activation function is a radial basis function, or a function whose value depends only on distance from some center point. The classic example of an RBF is the zero-centered Gaussian function, which takes the form:

$$f(x) = ae^{-bx^2} ; a, b > 0 \tag{4.1}$$

The general structure of an RBF-ANN is below. The input layer contains “R” inputs that interface with a hidden layer of “S¹” neurons through an “S¹ × R” matrix of weighted connections “W_{S¹,R}”. These weights determine the level to which each of the neurons “fire,” or contribute, to the output for a given input. The output vector has a length “S²” whose elements are formed through a weighted, linear summation of each neuron’s basis function (via the “L_{S²,S¹}” branches).

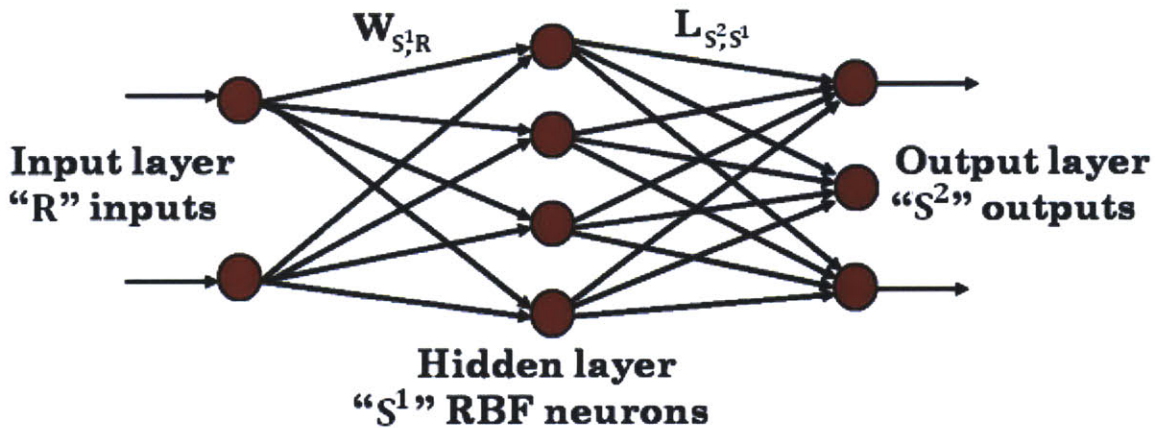


Figure 4-5: RBF-ANN basic architecture.

The MATLAB Neural Network Toolbox has built-in capabilities for quickly training and implementing an RBF-ANN with the architecture shown above [32]. The detailed inner working of each layer is shown in Figure 4-6. In this case, the network is described as having “ R ” inputs, “ S^1 ” RBF neurons in the hidden layer, and the output vector has length “ S^2 .”

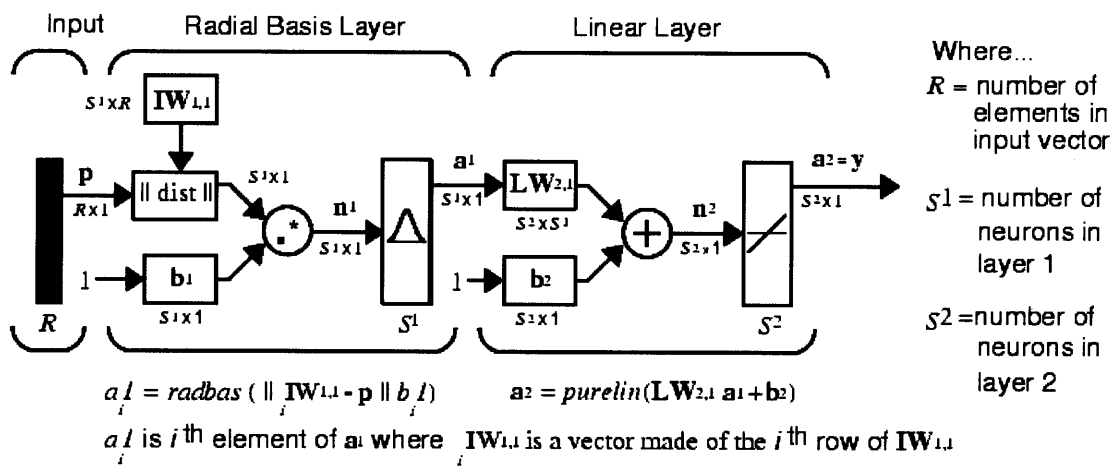


Figure 4-6: MATLAB RBF-ANN architecture details [32].

The above network is best understood by tracing the flow of an input vector through the network of Figure 4-6. Each input element in “ R ” is compared to an “ $S^1 \times R$ ” matrix of weights “ $\text{IW}_{1,1}$ ” producing an “ $S^1 \times 1$ ” vector of Euclidean distances between the input vector and each row of the weight matrix. The Euclidean distance is taken to be the square root of the sum of the individual distances squared. For example if an input vector is $\begin{bmatrix} 1 \\ 2 \end{bmatrix}$ and weight matrix “ $\text{IW}_{1,1}$ ” is $\begin{bmatrix} 3 & 3 \\ 1 & 2 \end{bmatrix}$, then the 2×1 vector of Euclidean distances would be $\begin{bmatrix} \sqrt{5} \\ 0 \end{bmatrix}$. The vector “ b_1 ” is a vector of spread biases for each neuron’s Gaussian basis function corresponding to the distance from the origin at which the amplitude of the Gaussian drops to one-half its center amplitude. If the distance between “ R ” and a neuron’s weight is

relatively small, that neuron will “fire” or activate, while if the distance is relatively large it will not. The larger the spread bias the more likely the neuron is to fire for inputs that are not very close to the weights. On the other hand, a small spread bias means that the neuron is extremely selective [32]. The output of the Radial Basis Layer “a¹” is then an “S¹ × I” vector of values determined by the MATLAB function *radbas*(), where:

$$radbas(n) = e^{-n^2} \tag{4.2}$$

Where *n* is the spread bias times the distance. Continuing along with the same numerical example, with the Euclidian distance vector $\begin{bmatrix} \sqrt{5} \\ 0 \end{bmatrix}$, and a spread bias constant of 0.8326 (corresponding to the standard unit Gaussian), then the “a¹” vector would be $\begin{bmatrix} 0.0312 \\ 1.0000 \end{bmatrix}$. This means that lower neuron in the vector is fully firing, while the upper neuron is only weakly firing due to its relatively large Euclidean distance for the given spread. The values in “a¹” are then weighted by “LW_{2,1}” and level-shifted by “b²” in the Linear Layer. The resultant output “a²” is an “S² × I” vector of values which represents the RBF-ANN’s predicted output for an input “R.”

MATLAB has two built in algorithms for instantiating and training an RBF-ANN [32]. One method uses exact design and produces a network with zero error on the training data. This method takes in a matrix of input vectors, a matrix of output vectors, and a spread constant then sets the weight matrices such that the function has zero error for any of these training inputs. Consequently, this method produces a network with as many neurons in the hidden layer as there are input vectors in the training matrix. A second, potentially more efficient, design iteratively adds neurons one at a time and adjusts weights until a sum-squared error goal is met. This training algorithm can result in a network that accurately performs its function with fewer neurons than the exact design training algorithm. In this chapter, RBF-ANNs implementing both training algorithms are used and compared.

4.2.2 Training Results

A training database of 30 input-output relations was created using COMSOL simulation. The 30 inputs (trench dimensions) used for training are listed in Figure 4-7 (the 100nm×80nm case was excluded from the training database and is used later as one of the test cases).

Depth: 50nm Width: 40nm	50nm 50nm	50nm 80nm	50nm 100nm	50nm 120nm
75nm 40nm	75nm 50nm	75nm 80nm	75nm 100nm	75nm 100nm
100nm 40nm	100nm 50nm		100nm 100nm	100nm 120nm
125nm 40nm	125nm 50nm	125nm 80nm	125nm 100nm	
150nm 40nm	150nm 50nm	150nm 80nm	150nm 100nm	
175nm 40nm	175nm 50nm	175nm 80nm	175nm 100nm	
200nm 40nm	200nm 50nm	200nm 80nm	200nm 100nm	

Figure 4-7: Training data inputs.

Networks were trained using both the exact and iterative methods described earlier. In each case a spread constant of 100 is specified [32]. Figure 4-8 provides a screenshot of the progress of the iterative training method. The network reaches a sum-squared error goal of 1×10^{-6} after adding 29 RBF neurons to the hidden layer. Because there are 30 sets of training data, the exact network has 30 RBF neurons in the hidden layer, and the iteratively-trained network ended up with one less neuron; however, the iteratively-trained network ended up converging to a network that is almost identical to the exact-trained network. The 29 neurons in the iteratively-trained network were nearly the same as 29 out of 30 of the neurons in the exact-trained network with differences in the “ $LW_{2,1}$ ” matrix of less than 1%. For this reason, we can expect the two networks to perform nearly the same.

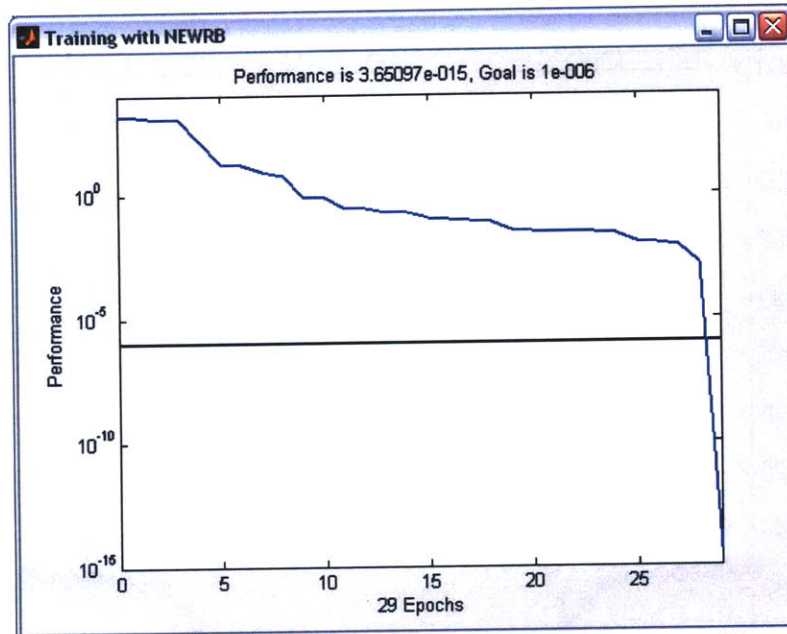


Figure 4-8: Screenshot of iterative RBF network training progress. The network reaches its sum-squared error goal of 1×10^{-6} after adding 29 neurons.

Several test cases were used to evaluate the performance of each network in predicting the forward model. The networks output prediction is compared against COMSOL simulation results. Sample results for a $100\text{nm} \times 80\text{nm}$ trench and a $120\text{nm} \times 60\text{nm}$ trench (depth \times width) are shown in Figure 4-9 and Figure 4-10, respectively. These trenches were not part of the training database. With only 30 sets of training data, it's clear that the RBF-ANN is excellent at mapping the forward model for trenches whose dimensions are on the order of those used in the training database. The performance of the iteratively-trained network is further demonstrated in Figure 4-11.

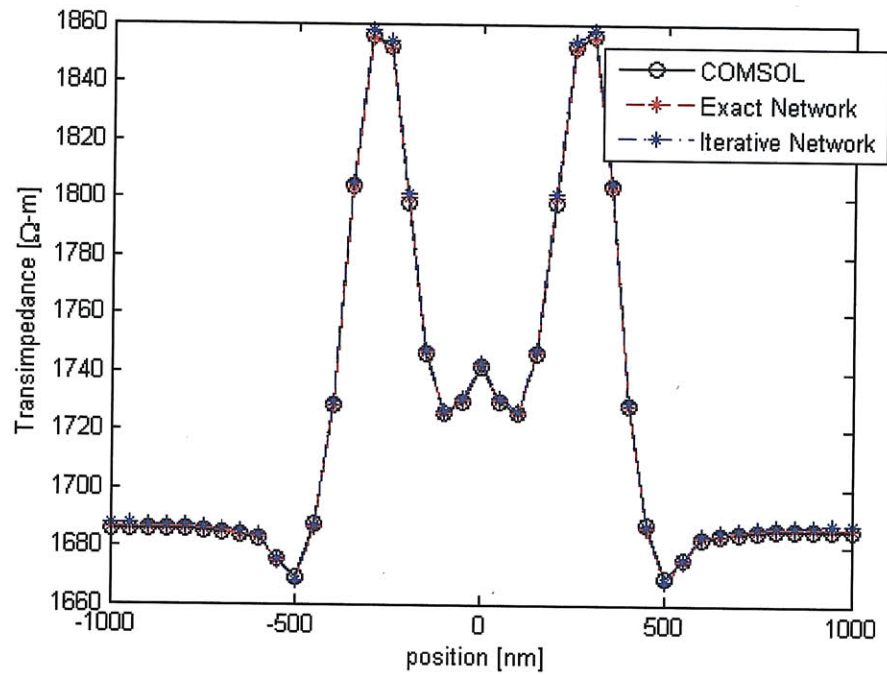


Figure 4-9: Forward model prediction performance for exact-trained and iteratively-trained RBF networks. Results are for a trench that is 100nm deep and 80nm wide.

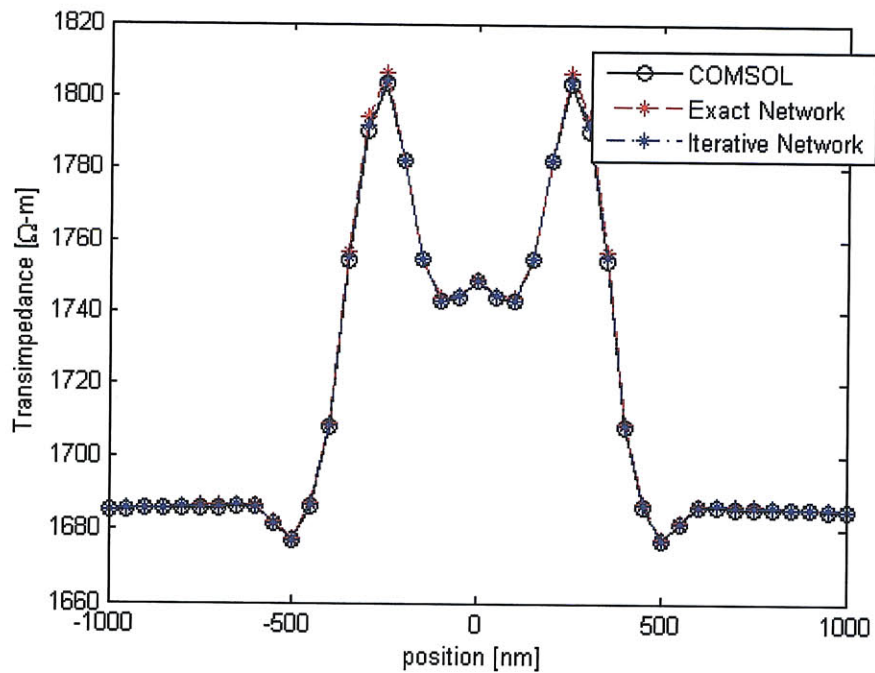


Figure 4-10: Forward model prediction performance for exact-trained and iteratively-trained RBF networks. Results are for a trench that is 120nm deep and 60nm wide.

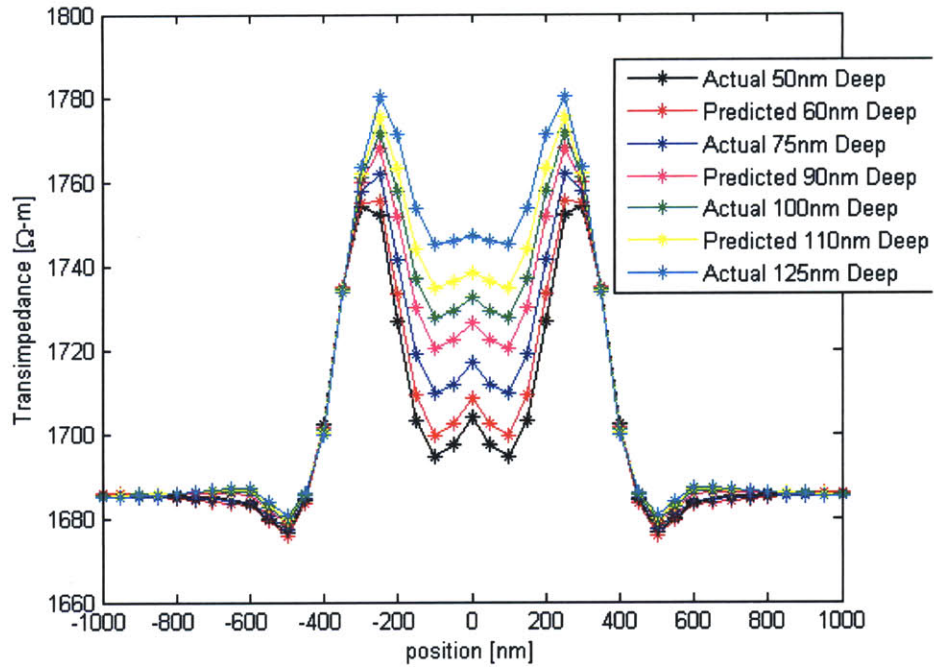


Figure 4-11: Demonstration of iteratively-trained RBF network performance. For a fixed trench width of 50nm, both network-predicted and actual outputs are plotted for various trench depths. The family of curves shows the accuracy of the RBF network compared to actual COMSOL results.

4.2.3 Signal Inversion Results

With confidence that the RBF network is well-trained for predicting the forward model through function approximation, it can now be used in an iterative signal inversion routine. The routine illustrated in Figure 4-4 is repeated below for the reader's convenience [31].

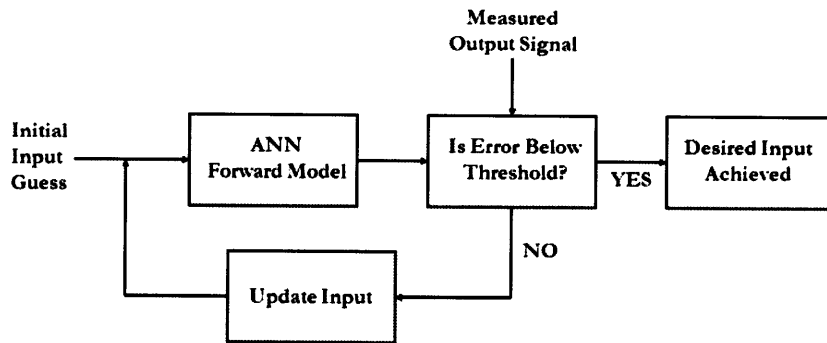


Figure 4-12: Iterative signal inversion block diagram [31].

The iterative error minimization routine is implemented using MATLAB’s built in function *fminsearch()*. This multivariable, nonlinear error minimization function takes in an initial guess for the trench dimensions and attempts to converge to a local minimum in this input space. MATLAB code for the signal inversion routine can be found in Appendix A.

The signal inversion routine was tested using measured trench data that did not belong to the network training database. Both the exact-trained and iteratively-trained networks were used in the routine. The performance of the routine is demonstrated in Figure 4-13 – Figure 4-16 for two different test cases implementing each of the two networks. The first two figures show the results for a 120nm×60nm trench—which is not part of the training database—using an exact-trained network and an iteratively-trained network, respectively. In each case an initial guess of 50nm×50nm is used. Figure 4-13 and Figure 4-14 indicate that each network type converges with almost identical performance (as expected) to predicted trench dimensions of 119.9nm×59.61nm—well within 1% of the actual values. Figure 4-15 and Figure 4-16 show the results for a 100nm×80nm trench with an initial guess of 200nm×200nm. The predicted dimensions are again within approximately 1% of the actual dimensions.

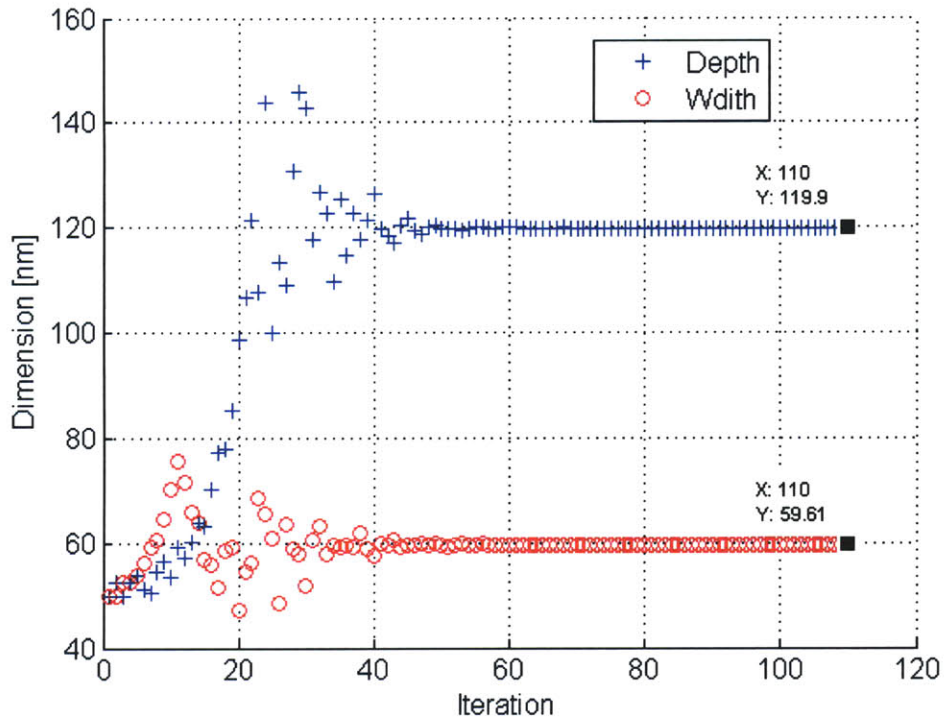


Figure 4-13: Signal inversion routine convergence for 120nm×60nm trench with initial guess of 50nm×50nm for exact-trained ANN.

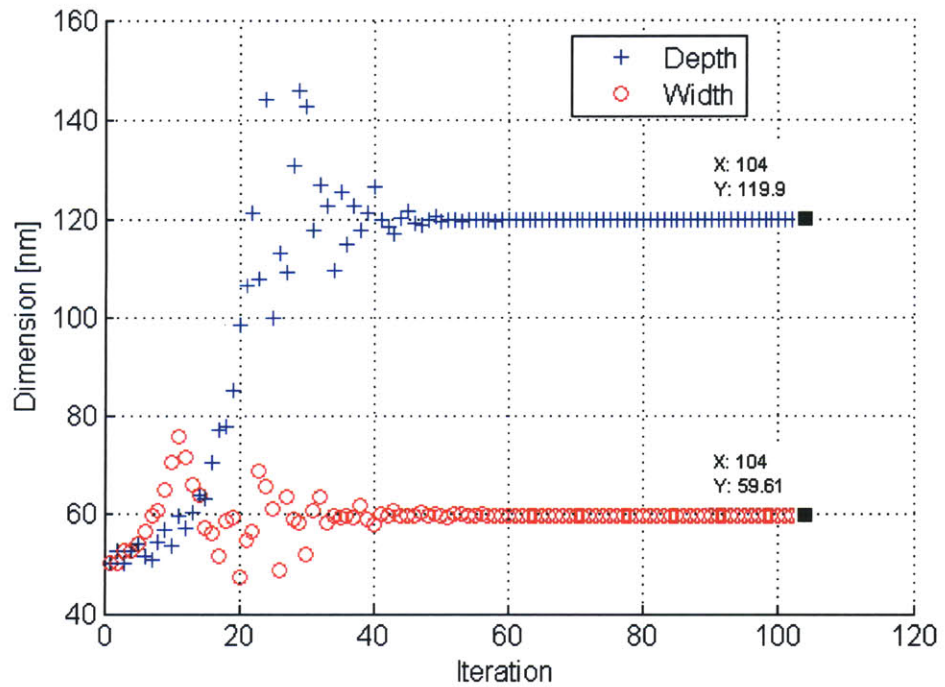


Figure 4-14: Signal inversion routine convergence for 120nm×60nm trench with initial guess of 50nm×50nm for iteratively-trained ANN.

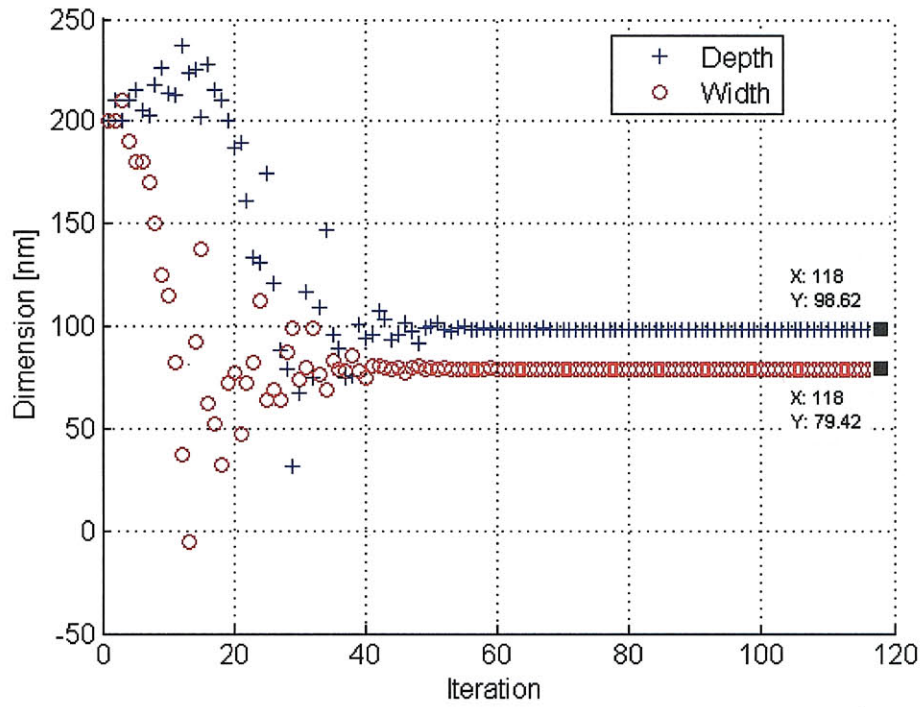


Figure 4-15: Signal inversion routine convergence for 100nm×80nm trench with initial guess of 200nm×200nm for exact-trained ANN.

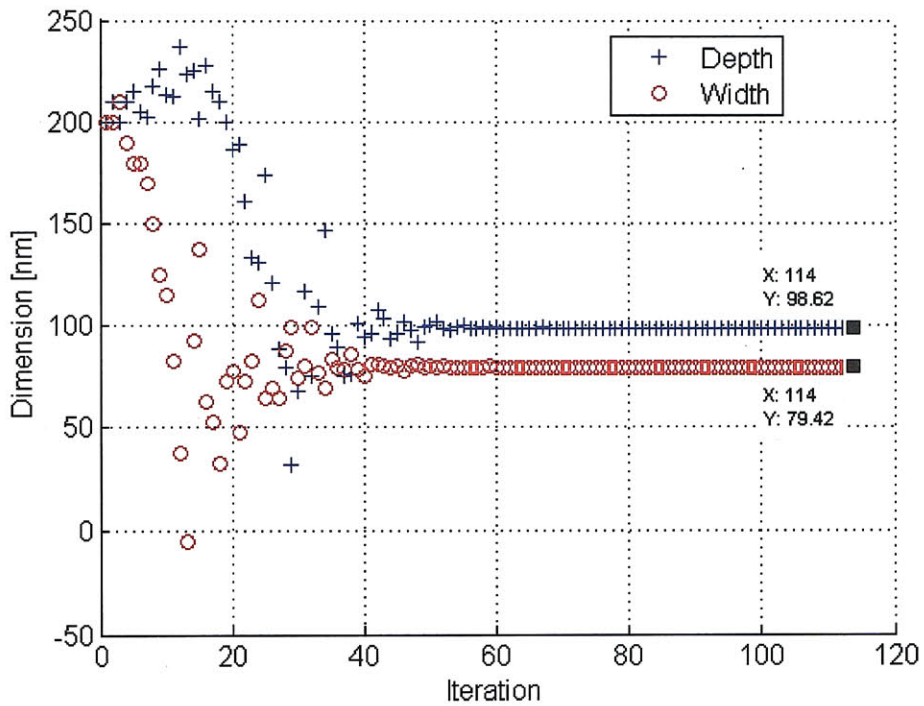


Figure 4-16: Signal inversion routine convergence for 100nm×80nm trench with initial guess of 200nm×200nm for iteratively-trained ANN.

It's clear that the networks are capable of accurately predicting the forward model, given a relatively small set of training data. It was demonstrated that these networks can be plugged into an iterative signal inversion routine to accurately predict an unknown trench's dimensions (within 1%), given a measured output signal. These specific networks were capable of performing forward functional mapping for two input parameters: trench depth and trench width. One can imagine extending the networks capabilities to more geometric and/or material input parameters (*e.g.* depth, width, length, conductivity, permittivity, pitch, radius, etc.) As one increases the number of inputs, though, the complexity of the network grows and a larger training database is required to achieve accurate forward functional mapping.

5 Conclusions and Suggestions for Future Work

The work presented in this thesis summarizes the results of several different case studies solving both forward and inverse electromagnetic sensor problems with a focus on capacitive sensors that operate in the electroquasistatic approximate. The capabilities and limitations of EQS sensors in detecting both surface features/objects and subsurface features were demonstrated. One of the largest limiting factors for EQS sensors in detecting subsurface features is charge relaxation. It was shown in this thesis how the charge relaxation (Equation (2.20)) determines whether a material will appear insulating or conducting to the sensors, depending on their operating frequency. For detecting subsurface features in relatively highly conducting materials, sensors operating in the magnetoquasistatic regime often prove to be a more effective solution due to induced eddy currents and enhanced field penetration depth when operated at low frequencies [1, 3-5, 16]. One possible area for future research in the field of sub-micron-scale imaging and detection via quasistatic sensors is an investigation into the scalability of EQS sensors vs. MQS sensors and the difficulties of fabricating nano-scale MQS sensor coils.

Chapter 2 presented a promising new method for mapping out the semiconducting layers of an integrated circuit. It was demonstrated through finite element method simulations how p-n junctions in a substrate can be located by monitoring steady-state sensor currents for harmonic distortion. . With sensors located over a p-n junction at a scan height of 200 nm and driven at 1GHz, the ratio

of the second harmonic current to the fundamental current on a sensor was shown exceed 9%. By coupling into p-n junctions through an air gap, non-contact, non-destructive methods for quickly imaging integrated circuits may be possible. Such an IC imaging technique could prove to be useful for verification and detection of fabrication errors as well as detecting hidden Trojan circuits that might be present on die. Advanced 3D FEM simulations of sensor scans over wells of various dimensions are suggested to extend the simulation work presented in this thesis. In addition to more simulation-based analysis, laboratory experiments would prove invaluable in confirming simulation results.

Chapter 3 demonstrated the sensitivity of EQS sensors to contaminant objects on the surface of a photomask. FEM simulation results showed the capability of capacitive EQS sensors in detecting various contaminant particles located in a 100nm wide by 70nm deep gap in the absorber layer of an EUVL photomask. With variations in the sensor currents on the order of 1 nA, these results motivate the need for the development of low-noise pickup circuitry to interface with the sensors. A brief discussion of thermal noise considerations was presented. An investigation into possible narrow band, low-noise circuits could serve as a topic of future research.

Chapter 4 solved an inverse electromagnetic sensor problem by training a radial basis function artificial neural network to accurately approximate the forward mapping of a feature's physical dimensions into a sensor's impedance response as it scans past the feature. This function-approximation network was then inserted into an iterative signal inversion routine. The RBF-ANN was capable of accurately predicting an unknown trench's dimensions to within 1%, given a measured output signal. These specific networks were capable of performing forward functional mapping for two input parameters: trench depth and trench width. Extending the network capabilities to more geometric and/or material input parameters (*e.g.* conductivity, permittivity, pitch, radius, etc.) could serve as a topic of future research on this project. Furthermore, while this specific algorithm proved

to solve the inverse problem quite successfully, it was performed strictly as a post-processing exercise. A suggested area for future research would be the integration of the signal inversion routine into the real-time operation of the sensor array. It would indeed be an interesting case-study to investigate the operation of the signal inverter in real-time and its potential limitations on scan speed.

One final suggestion for future work is rooted in the idea of massive parallelism. Present-day scanning imaging techniques (SCM, AFM, SMM, etc.) rely on the raster-scanning of a single probe/electrode [13-15, 33]. Large arrays of EQS/QMS electrodes could potentially provide the integrated circuit industry with inspection tools that can quickly scan photolithography equipment, ICs, and other IC fabrication equipment for features, defects, and contaminants at speeds far above the capabilities of current, single-probe technologies.

Bibliography

- [1] N. J. Goldfine, *et al.*, "High-resolution inductive array imaging of buried objects," in *SPIE AeroSense*, Orlando, FL, 2000, pp. 56-65.
- [2] J. E. Lenz, "A review of Magnetic Sensors," *Proceedings of the IEEE*, vol. 78, June 1990.
- [3] A. V. Mamishev, *et al.*, "Interdigital sensors and transducers," *Proceedings of the IEEE*, vol. 92, pp. 808-845, 2004.
- [4] Y. Sheiretov, "Deep Penetration Magnetoquasistatic Sensors," Ph.D., Department of Electrical Engineering and Computer Science, Massachusetts Institute of Technology, Cambridge, MA, 2001.
- [5] V. Zilberstein, *et al.*, "MWM eddy-current arrays for crack initiation and growth monitoring," *International Journal of Fatigue*, vol. 25, pp. 1147-1155.
- [6] N. J. Goldfine, *et al.*, "Segmented Field Dielectrometer," United States Patent 6,486,673, 2000.
- [7] J. M. Papazian, *et al.*, "Sensors for monitoring early stage fatigue cracking," *International Journal of Fatigue*, vol. 29, pp. 1668-1680.
- [8] J. Cooley, *et al.*, "Proximity Detection and Ranging Using a Modified Fluorescent Lamp for Security Applications," in *Carnahan Conferences Security Technology, Proceedings 2006 40th Annual IEEE International*, 2006, pp. 1-8.
- [9] J. R. Melcher, "Aparatus and Methods for Measuring Permeability and Conductivity in Materials Using Multiple Wavelength Interrogations," United States Patent 5,015,951, 1991.
- [10] A. V. Mamishev, "Interdigital Dielectrometry Sensor Design and Parameter Estimation Algorithms for Non-Destructive Materials Evaluation," Ph.D., Department of Electrical Engineering and Computer Science, Massachusetts Institute of Technology, Cambridge, MA, 1999.
- [11] D. Schlicker, "Imaging of Absolute Electrical Properties Using Electroquasistatic and Magnetoquasistatic Sensor Arrays," Ph.D., Department of Electrical and Engineering and Computer Science, Massachusetts Institute of Technology, Cambridge, MA, 2005.
- [12] A. N. Tikhonov and V. Y. Arsenin, *Solutions of Ill-Posed Problems*. New York, NY: Winston, 1977.
- [13] G. Binnig, *et al.*, "Atomic Force Microscope," *Physical Review Letters*, vol. 56, p. 930, 1986.
- [14] J. R. Matey, "Scanning Capacitance Microscope," United States Patent 4,481,616, 1981.

- [15] C. C. Williams, "Two-dimensional dopant profiling by scanning capacitance microscopy," *Annual Review of Materials Science*, vol. 29, pp. 471-504, 1999.
- [16] COMSOL Multiphysics, Ver. 3.5a: www.comsol.com, 2008.
- [17] M. Abramovici and P. L. Levin. (Jan/Feb 2009, *Protecting Integrated Circuits from Silicon Trojan Horses*. Available: <http://www.mil-embedded.com/articles/id/?3748>
- [18] G. W. Neudeck, *The PN Junction Diode: Volume 2 (Modular Series on Solid State Devices)*, 2nd ed. Reading, MA: Addison-Wesley, 1989.
- [19] S. M. Sze, *Physics of Semiconductor Devices*, 2nd ed. New York, NY: John Wiley & Sons, Inc., 1981.
- [20] M. Zahn, *Electromagnetic Field Theory: A Problem Solving Approach*. Malabar, FL: Krieger, 2003.
- [21] B. Wu and A. Kumar, "Extreme ultraviolet lithography: A review," *Journal of Vacuum Science & Technology B: Microelectronics and Nanometer Structures*, vol. 25, pp. 1743-1761, 2007.
- [22] R. Carminati, *et al.*, "Reciprocity of evanescent electromagnetic waves," *J. Opt. Soc. Am. A*, vol. 15, pp. 706-712, 1998.
- [23] D. M. Pozar, *Microwave Engineering: Third Edition*. New York, NY: John Wiley & Sons, Inc., 2008.
- [24] *AD7747 24-Bit Capacitance-to-Digital Converter with Temperature Sensor*: Analog Devices, Inc. www.analog.com, 2007.
- [25] R. Sarpeshkar, *et al.*, "White Noise in MOS Transistors and Resistors," *IEEE Circuits & Devices Magazine*, vol. 9, pp. 23-29, Nov. 1993.
- [26] P. R. Gray, *et al.*, *Analysis and Design of Analog Integrated Circuits: Fourth Edition*. New York, NY: John Wiley & Sons, 2001.
- [27] J. M. Meek and J. D. Craggs, *Electrical breakdown of gases*. New York, NY: John Wiley & Sons, 1978.
- [28] M. Zahn, "Solid, Liquid, and Gaseous Electrical Insulation," in *Encyclopedia of Applied Physics* vol. 18, ed. Weinheim: VCH Publishers, 1997, pp. 431-466.
- [29] T. H. Lee, *The Design of CMOS Radio-Frequency Integrated Circuits: Second Edition*. Cambridge: Cambridge University Press, 2004.
- [30] K. Hwang, *et al.*, "Application of Wavelet Basis Function Neural Networks to NDE," in *IEEE 39th Midwest Symposium on Circuits and Systems*, 1996, pp. 1420-1423.
- [31] P. Ramuhalli, *et al.*, "Electromagnetic NDE signal inversion by function-approximation neural networks," *Magnetics, IEEE Transactions on*, vol. 38, pp. 3633-3642, 2002.
- [32] MATLAB Online Helpdesk for Radial Basis Functions: Neural Network Toolbox: The MathWorks, Inc. http://www.mathworks.com/access/helpdesk/help/toolbox/nnet/radial_3.html, 2010.
- [33] J. Park, *et al.*, "Observation of biological samples using a scanning microwave microscope," *Ultramicroscopy*, vol. 102, pp. 101-106, 2005.

Appendix A: MATLAB Code for Iterative Signal Inversion Routine

The following code corresponds to the iterative signal inversion routine described in Section 4.2.

```
%Function RBF_Input_Predictor takes in three parameters:
%  initial_guess - An initial guess at the trench
%    dimensions: [depth ; width]
%  measured_output_data - measured impedance signal for the
%    unknown trench
%  network - A trained artificial neural network to approximate
%    forward model
%Attempts to converge to a set of predicted trench dimensions [depth ;
%width] that might have caused measured_output_data. Implements
%fminsearch() to minimize a sum of squares error between RBF-ANN output
%and measured output data.

function Inputs = RBF_Input_Predictor( initial_guess, measured_output_data,
network )

    iter = 0;
    net = network;

%Function errorfun calculates a sum-of-squares error between the
%current iteration's predicted output and the measured output data.
%Takes in two parameters:
%  currentInputValues - current iteration's guess at the trench
%    dimensions [depth ; width]
%  measured_output_data - measured impedance signal for the unknown
%    trench
function Error = errorfun( currentInputValues, measured_output_data )

    hold on;

    %run the RBFANN forward model for the current
    %iteration's input values
    CurrentOutput = sim(net, currentInputValues);
```

```

    %determine the sum of squares error for the current
    %output vs the measured output data
    Difference = CurrentOutput - measured_output_data;
    SqDifference = Difference.^2;
    Error = sqrt(sum(SqDifference));

    %plotting details
    disp([currentInputValues', Error]);
    curdepth = currentInputValues(1);
    curwidth = currentInputValues(2);
    iter = iter + 1;
    handlevec(:,1)=plot(iter, curdepth, 'b+');
    handlevec(:,2)=plot(iter, curwidth, 'ro');
    pause(0.01);

end

%Termination tolerance on error
Options = optimset('TolFun', 0.05);
%Iterative error minimization search function. Attempts
%to minimize function errorfun() for measured_output_data
%with initial_guess.
Inputs = fminsearch(@(currentInputValues) errorfun(currentInputValues,
measured_output_data ), initial_guess, Options );

%plotting details
legend(handlevec);
end

```

Appendix B: COMSOL Settings for p-n Junction Geometry #1

The following is a COMSOL auto-generated report that corresponds to the FEM simulation results that were presented in Section 2.3 and Section 2.4. The report provides information about FEM model properties, meshing settings, boundary conditions, solver settings, solver variables, constants used, etc.



p-n junction Geometry



1. Model Properties

Property	Value
Model name	p-n junction Geometry
Author	COMSOL
Company	COMSOL
Department	
Reference	Copyright (c) 1998-2008 by COMSOL AB
URL	www.comsol.com
Saved date	Mar 30, 2010 8:08:53 AM
Creation date	Nov 17, 2008 7:33:45 PM
COMSOL version	COMSOL 3.5.0.603

File name: C:\Documents and Settings\BCANNON\Desktop\PN Junction Air Cases\Segmented Electrodes\1GHz PN_transient Step epsilon = 1.mph

Application modes and modules used in this model:

- Geom1 (2D)
 - Electrostatics
 - Convection and Diffusion
 - Convection and Diffusion
 - Weak Form, Boundary

1.1. Model description

Semiconductor Diode

A semiconductor device model featuring a diode with p- and n-type regions. The image shows the hole concentration for 0.5V forward bias.

2. Constants

Name	Expression	Value	Description
q	1.602e-19[C]		Elementary charge
T	300[K]		Room temperature

file://C:\Documents and Settings\BCANNON\Desktop\PN Junction Air Cases\Segmented ... 4/20/2010

k	1.38e-23[J/K]	Boltzmann constant
epsilon	11.8	Rel. permittivity for Si
ni	1.46e10[1/cm^3]	Intrinsic concentration for Si
mun	800[cm^2/(V*s)]	Electron mobility for Si
mup	400[cm^2/(V*s)]	Hole mobility for Si
Dn	k^*T/q^*mun	Electron diffusivity
Dp	k^*T/q^*mup	Hole diffusivity
taun	0.1[us]	Electron life time
taup	0.1[us]	Hole life time
c	$q/(k^*T)$	Reciprocal thermal voltage
y1	7[um]	Diode dimension
x1	5[um]	Diode dimension
ju	.707[um]	Junction depth
ac	2[um]	Anode dimension
NAprmax	1e16[1/cm^3]	Maximum p-type doping
NDn	1e14[1/cm^3]	Drift layer n-type doping
NDnmax	1e16[1/cm^3]	Maximum n-type doping
ch	$ju/sqrt(log(NAprmax/NDn))$	Doping fall-off constant
Va	0[V]	Applied voltage
ya	-0.3e-6[m]	
tbreak	.00001[s]	

3. Geom1

Space dimensions: 2D

Independent variables: x, y, z

3.1. Scalar Expressions

Name	Expression	Unit	Description
N	$((y > ya) * (2 * NDnmax * exp(-((y - ya) / ch)^2) - NAprmax) + (y <= ya) * NDnmax)$	1/m^3	Doping concentration
n_init	$(abs(N) / 2 + sqrt(N^2 / 4 + ni^2)) * (N >= 0) + ni^2 / (abs(N) / 2 + sqrt(N^2 / 4 + ni^2)) * (N < 0)$	1/m^3	Charge neutrality electron concentration
p_init	$(abs(N) / 2 + sqrt(N^2 / 4 + ni^2)) * (N < 0) + ni^2 / (abs(N) / 2 + sqrt(N^2 / 4 + ni^2)) * (N >= 0)$	1/m^3	Charge neutrality hole concentration
psi_init	$1/c * (-log(p_init/ni) * (N < 0) + log(n_init/ni) * (N >= 0))$	V	Charge neutrality voltage
RSRH	$(cn * cp - ni^2) / (taup * (cn + ni) + taun * (cp + ni))$		Recombination term
Va1	$(t - tbreak) * .1 * sin(2 * pi * 1000 * (t - tbreak))$		

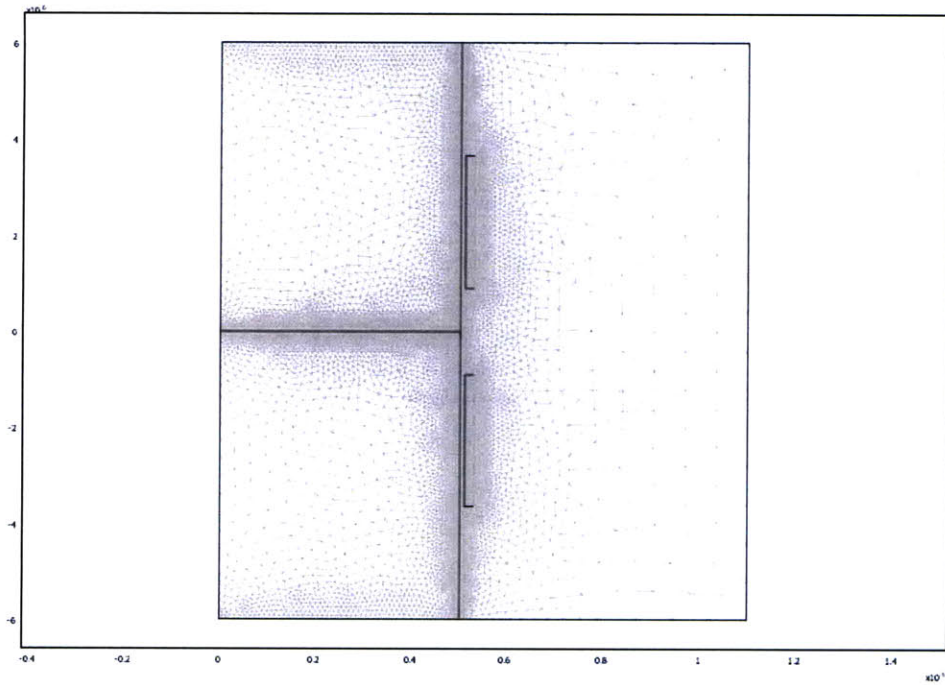
3.2. Mesh

3.2.1. Mesh Statistics

Number of degrees of freedom	117673
Number of mesh points	14279
Number of elements	28333
Triangular	28333
Quadrilateral	0
Number of boundary elements	1182

file://C:\Documents and Settings\BCANNON\Desktop\PN Junction Air Cases\Segmented ... 4/20/2010

Number of vertex elements	18
Minimum element quality	0.601
Element area ratio	0



3.3. Application Mode: Electrostatics (es)

Application mode type: Electrostatics

Application mode name: es

3.3.1. Scalar Variables

Name	Variable	Value	Unit	Description
epsilon0	epsilon0_es	8.854187817e-12	F/m	Permittivity of vacuum

3.3.2. Application Mode Properties

Property	Value
Default element type	Lagrange - Quadratic
Input property	Forced voltage
Frame	Frame (ref)

Weak constraints	Off
Constraint type	Ideal

3.3.3. Variables

Dependent variables: psi

Shape functions: shlag(2,'psi')

Interior boundaries active

3.3.4. Boundary Settings

Boundary		1, 3, 7, 9, 20	2, 5	4
Type		Zero charge/Symmetry	Electric potential	Continuity
Surface charge density (rhos)	C/m ²	0	0	0
Electric potential (V0)	V	0	psi_init	0

Boundary		6, 8	10-13, 18	14-17, 19
Type		Surface charge	Electric potential	Electric potential
Surface charge density (rhos)	C/m ²	rhos	0	0
Electric potential (V0)	V	0	-15*sin(2000000000*pi*t)	15*sin(2000000000*pi*t)

3.3.5. Subdomain Settings

Subdomain		1-2	3-5
Relative permittivity (epsilon_r)	1	{epsilon_rn,0,0,epsilon_rn}	{1,0,0,1}
Space charge density (rho)	C/m ³	q*(N-cn+cp)	0

Subdomain initial value	1-2	3-5
Electric potential (psi)	V psi_init	0

3.4. Application Mode: Convection and Diffusion (cd)

Application mode type: Convection and Diffusion

Application mode name: cd

3.4.1. Application Mode Properties

Property	Value
Default element type	Lagrange - Quadratic
Analysis type	Transient
Equation form	Conservative
Frame	Frame (ref)
Weak constraints	On
Constraint type	Ideal

3.4.2. Variables

Dependent variables: cn

Shape functions: shlag(2,'lm2'), shlag(2,'cn')

Interior boundaries active

3.4.3. Boundary Settings

Boundary		1, 3	2, 5	4, 7, 9-20
Type		Insulation/Symmetry	Concentration	Continuity
Concentration (c0)	mol/m ³	0	n_init	0

Boundary		6, 8
Type		Convective flux
Concentration (c0)	mol/m ³	0

3.4.4. Subdomain Settings

Subdomain		1-2
Shape functions (shape)		shlag(2,'lm2') shlag(2,'cn')
Integration order (gporder)		4
Diffusion coefficient (D)	m ² /s	Dn
x-velocity (u)	m/s	mun*psix
y-velocity (v)	m/s	mun*psiy

Subdomain initial value		1-2
Concentration, cn (cn)	mol/m ³	n_init

3.5. Application Mode: Convection and Diffusion (cd2)

Application mode type: Convection and Diffusion

Application mode name: cd2

3.5.1. Application Mode Properties

Property	Value
Default element type	Lagrange - Quadratic
Analysis type	Transient
Equation form	Conservative
Frame	Frame (ref)
Weak constraints	On
Constraint type	Ideal

3.5.2. Variables

Dependent variables: cp

Shape functions: shlag(2,'lm3'), shlag(2,'cp')

Interior boundaries active

3.5.3. Boundary Settings

Boundary		1, 3	2, 5	4, 7, 9-20
Type		Insulation/Symmetry	Concentration	Continuity
Concentration (c0)	mol/m ³	0	p_init	0

Boundary		6, 8
Type		Convective flux
Concentration (c0)	mol/m ³	0

3.5.4. Subdomain Settings

Subdomain		1-2
Shape functions (shape)		shlag(2,'lm3') shlag(2,'cp')
Integration order (gporder)		4
Diffusion coefficient (D)	m ² /s	Dp
x-velocity (u)	m/s	-mup*psix
y-velocity (v)	m/s	-mup*psiy

Subdomain initial value		1-2
Concentration, cp (cp)	mol/m ³	p_init

3.6. Application Mode: Weak Form, Boundary (wb)

Application mode type: Weak Form, Boundary

Application mode name: wb

3.6.1. Application Mode Properties

Property	Value
Default element type	Lagrange - Quadratic
Wave extension	Off
Frame	Frame (ref)
Weak constraints	Off

3.6.2. Variables

Dependent variables: rhos, rhos_t

Shape functions: shlag(2,'rhos')

Interior boundaries not active

3.6.3. Boundary Settings

Boundary		6, 8
Weak term (weak)		rhos_test*(-q*ntflux_cn_cd+q*ntflux_cp_cd2)
Time-dependent weak term (dweak)		rhos_test*rhos_time

4. Materials/Coefficients Library

file://C:\Documents and Settings\BCANNON\Desktop\PN Junction Air Cases\Segmented ... 4/20/2010

4.1. Air

Parameter	Value
Heat capacity at constant pressure (C)	$C_p(T[1/K])[J/(kg*K)]$
Speed of sound (cs)	$cs(T[1/K])[m/s]$
Dynamic viscosity (eta)	$eta(T[1/K])[Pa*s]$
Ratio of specific heats (gamma)	1.4
Thermal conductivity (k)	$k(T[1/K])[W/(m*K)]$
Kinematic viscosity (nu0)	$nu_0(T[1/K])[m^2/s]$
Density (rho)	$rho(p[1/Pa], T[1/K])[kg/m^3]$
Electric conductivity (sigma)	0[S/m]

4.1.1. Functions

Function	Expression	Derivatives	Complex output
cs(T)	$\sqrt{1.4*287*T}$	$d(\sqrt{1.4*287*T}, T)$	false
rho(p, T)	$p^{0.02897/8.314/T}$	$d(p^{0.02897/8.314/T}, p), d(p^{0.02897/8.314/T}, T)$	false

4.1.2. Piecewise Analytic Functions

4.1.2.1. Function: Cp(T)

Type: Polynomial

x_start	x_end	f(x)
200	1600	0 1.04763657E+03 1 -3.72589265E-01 2 9.45304214E-04 3 -6.02409443E-07 4 1.28589610E-10

4.1.2.2. Function: eta(T)

Type: Polynomial

x_start	x_end	f(x)
200	1600	0 -8.38278000E-07 1 8.35717342E-08 2 -7.69429583E-11 3 4.64372660E-14 4 -1.06585607E-17

4.1.2.3. Function: nu0(T)

Type: Polynomial

x_start	x_end	f(x)
200	1600	0 -5.86912450E-06 1 5.01274491E-08 2 7.50108343E-11 3 1.80336823E-15 4 -2.91688030E-18

4.1.2.4. Function: k(T)

Type: Polynomial

x_start	x_end	f(x)
200	1600	0 -2.27583562E-03 1 1.15480022E-04 2 -7.90252856E-08 3 4.11702505E-11 4 -7.43864331E-15

5. Integration Coupling Variables

5.1. Geom1

6. Solver Settings

Solve using a script: off

Auto select solver	On
Solver	Time dependent
Solution form	Automatic
Symmetric	Off
Adaptive mesh refinement	Off
Optimization/Sensitivity	Off
Plot while solving	Off

6.1. Direct (PARDISO)

Solver type: Linear system solver

Parameter	Value
Preordering algorithm	Nested dissection
Row preordering	On
Bunch-Kaufmann	Off
Pivoting perturbation	1.0E-8
Relative tolerance	1.0E-6
Factor in error estimate	400.0
Check tolerances	On

6.2. Time Stepping

Parameter	Value
Times	range(0.,00000000001,.000000004)
Relative tolerance	.0005
Absolute tolerance	.0000005
Times to store in output	Specified times
Time steps taken by solver	Strict
Maximum BDF order	5
Singular mass matrix	Maybe
Consistent initialization of DAE systems	Backward Euler
Error estimation strategy	Include algebraic
Allow complex numbers	Off

6.3. Advanced

Parameter	Value
Constraint handling method	Elimination
Null-space function	Automatic
Automatic assembly block size	On
Assembly block size	1000
Use Hermitian transpose of constraint matrix and in symmetry detection	Off
Use complex functions with real input	Off

file://C:\Documents and Settings\BCANNON\Desktop\PN Junction Air Cases\Segmented ... 4/20/2010

Stop if error due to undefined operation	On
Store solution on file	Off
Type of scaling	Automatic
Manual scaling	
Row equilibration	On
Manual control of reassembly	Off
Load constant	On
Constraint constant	On
Mass constant	On
Damping (mass) constant	On
Jacobian constant	On
Constraint Jacobian constant	On

7. Variables

7.1. Boundary

7.1.1. Boundary 1-6, 8

Name	Description	Unit	Expression
unTE _x _es	Maxwell surface stress tensor (x)	Pa	$-0.5 * (\text{up}(Dx_es) * \text{up}(Ex_es) + \text{up}(Dy_es) * \text{up}(Ey_es)) * \text{dnx} + (\text{dnx} * \text{up}(Dx_es) + \text{dny} * \text{up}(Dy_es)) * \text{up}(Ex_es)$
unTE _y _es	Maxwell surface stress tensor (y)	Pa	$-0.5 * (\text{up}(Dx_es) * \text{up}(Ex_es) + \text{up}(Dy_es) * \text{up}(Ey_es)) * \text{dny} + (\text{dnx} * \text{up}(Dx_es) + \text{dny} * \text{up}(Dy_es)) * \text{up}(Ey_es)$
dnTE _x _es	Maxwell surface stress tensor (x)	Pa	$-0.5 * (\text{down}(Dx_es) * \text{down}(Ex_es) + \text{down}(Dy_es) * \text{down}(Ey_es)) * \text{unx} + (\text{unx} * \text{down}(Dx_es) + \text{uny} * \text{down}(Dy_es)) * \text{down}(Ex_es)$
dnTE _y _es	Maxwell surface stress tensor (y)	Pa	$-0.5 * (\text{down}(Dx_es) * \text{down}(Ex_es) + \text{down}(Dy_es) * \text{down}(Ey_es)) * \text{uny} + (\text{unx} * \text{down}(Dx_es) + \text{uny} * \text{down}(Dy_es)) * \text{down}(Ey_es)$
unTx _{es}	Exterior Maxwell stress tensor (u), x component	Pa	unTE _x _es+unTM _x _es
unTM _x _es	Exterior magnetic Maxwell stress tensor (u), x component	Pa	0
unTy _{es}	Exterior Maxwell stress tensor (u), y component	Pa	unTE _y _es+unTM _y _es
unTM _y _es	Exterior magnetic Maxwell stress tensor (u), y component	Pa	0
dnTx _{es}	Exterior Maxwell stress tensor (d), x component	Pa	dnTE _x _es+dnTM _x _es
dnTM _x _es	Exterior magnetic Maxwell stress tensor (d), x component	Pa	0
dnTy _{es}	Exterior Maxwell stress tensor (d), y component	Pa	dnTE _y _es+dnTM _y _es
dnTM _y _es	Exterior magnetic Maxwell stress tensor (d), y component	Pa	0
dVol _{nd} _es	Volume integration contribution	m	d _{es}
nD _{es}	Surface charge density	C/m ²	unx * (down(Dx _{es})-up(Dx _{es}))+uny * (down(Dy _{es})-up(Dy _{es}))

file://C:\Documents and Settings\BCANNON\Desktop\PN Junction Air Cases\Segmented ... 4/20/2010

			(Dy_es)
ndflux_cn_cd	Normal diffusive flux, cn	mol/(m ² *s)	rx_cd * dflux_cn_x_cd+ny_cd * dflux_cn_y_cd
nflux_cn_cd	Normal convective flux, cn	mol/(m ² *s)	rx_cd * cflux_cn_x_cd+ny_cd * cflux_cn_y_cd
ntflux_cn_cd	Normal total flux, cn	mol/(m ² *s)	rx_cd * tflux_cn_x_cd+ny_cd * tflux_cn_y_cd
ndflux_cp_cd2	Normal diffusive flux, cp	mol/(m ² *s)	rx_cd2 * dflux_cp_x_cd2+ny_cd2 * dflux_cp_y_cd2
nflux_cp_cd2	Normal convective flux, cp	mol/(m ² *s)	rx_cd2 * cflux_cp_x_cd2+ny_cd2 * cflux_cp_y_cd2
ntflux_cp_cd2	Normal total flux, cp	mol/(m ² *s)	rx_cd2 * tflux_cp_x_cd2+ny_cd2 * tflux_cp_y_cd2

7.1.2. Boundary 7, 9-20

Name	Description	Unit	Expression
unTE _x _{es}	Maxwell surface stress tensor (x)	Pa	-0.5 * (up(Dx _{es}) * up(Ex _{es})+up(Dy _{es}) * up(Ey _{es})) * dnx+(d _{nx} * up(Dx _{es})+d _{ny} * up(Dy _{es})) * up(Ex _{es})
unTE _y _{es}	Maxwell surface stress tensor (y)	Pa	-0.5 * (up(Dx _{es}) * up(Ex _{es})+up(Dy _{es}) * up(Ey _{es})) * dny+(d _{nx} * up(Dx _{es})+d _{ny} * up(Dy _{es})) * up(Ey _{es})
dnTE _x _{es}	Maxwell surface stress tensor (x)	Pa	-0.5 * (down(Dx _{es}) * down(Ex _{es})+down(Dy _{es}) * down(Ey _{es})) * unx+(unx * down(Dx _{es})+uny * down(Dy _{es})) * down(Ex _{es})
dnTE _y _{es}	Maxwell surface stress tensor (y)	Pa	-0.5 * (down(Dx _{es}) * down(Ex _{es})+down(Dy _{es}) * down(Ey _{es})) * uny+(unx * down(Dx _{es})+uny * down(Dy _{es})) * down(Ey _{es})
unTx _{es}	Exterior Maxwell stress tensor (u), x component	Pa	unTE _x _{es} +unTM _x _{es}
unTM _x _{es}	Exterior magnetic Maxwell stress tensor (u), x component	Pa	0
unTy _{es}	Exterior Maxwell stress tensor (u), y component	Pa	unTE _y _{es} +unTM _y _{es}
unTM _y _{es}	Exterior magnetic Maxwell stress tensor (u), y component	Pa	0
dnTx _{es}	Exterior Maxwell stress tensor (d), x component	Pa	dnTE _x _{es} +dnTM _x _{es}
dnTM _x _{es}	Exterior magnetic Maxwell stress tensor (d), x component	Pa	0
dnTy _{es}	Exterior Maxwell stress tensor (d), y component	Pa	dnTE _y _{es} +dnTM _y _{es}
dnTM _y _{es}	Exterior magnetic Maxwell stress tensor (d), y component	Pa	0
dVolbnd _{es}	Volume integration contribution	m	d _{es}
nD _{es}	Surface charge density	C/m ²	unx * (down(Dx _{es})-up(Dx _{es}))+uny * (down(Dy _{es})-up(Dy _{es}))
ndflux_cn_cd	Normal diffusive flux, cn	mol/(m ² *s)	
nflux_cn_cd	Normal convective flux, cn	mol/(m ² *s)	

ntflux_cn_cd	Normal total flux, cn	mol/ (m ² *s)	
ndflux_cp_cd2	Normal diffusive flux, cp	mol/ (m ² *s)	
ncflux_cp_cd2	Normal convective flux, cp	mol/ (m ² *s)	
ntflux_cp_cd2	Normal total flux, cp	mol/ (m ² *s)	

7.2. Subdomain

7.2.1. Subdomain 1-2

Name	Description	Unit	Expression
dVol_es	Volume integration contribution	m	d_es
Dx_es	Electric displacement, x component	C/m ²	epsilon _{xx} _es * Ex_es+epsilon _{xy} _es * Ey_es
Dy_es	Electric displacement, y component	C/m ²	epsilon _{yx} _es * Ex_es+epsilon _{yy} _es * Ey_es
epsilon_es	Permittivity	F/m	epsilon ₀ _es * epsilon _r _es
epsilon _{xx} _es	Permittivity, xx component	F/m	epsilon ₀ _es * epsilon _{xx} _es
epsilon _{xy} _es	Permittivity, xy component	F/m	epsilon ₀ _es * epsilon _{xy} _es
epsilon _{yx} _es	Permittivity, yx component	F/m	epsilon ₀ _es * epsilon _{yx} _es
epsilon _{yy} _es	Permittivity, yy component	F/m	epsilon ₀ _es * epsilon _{yy} _es
normE_es	Electric field, norm	V/m	sqrt(abs(Ex_es)^2+abs(Ey_es)^2)
normD_es	Electric displacement, norm	C/m ²	sqrt(abs(Dx_es)^2+abs(Dy_es)^2)
normDr_es	Remanent displacement, norm	C/m ²	sqrt(abs(Drx_es)^2+abs(Dry_es)^2)
normP_es	Electric polarization, norm	C/m ²	sqrt(abs(Px_es)^2+abs(Py_es)^2)
We_es	Electric energy density	J/m ³	0.5 * ((Dx_es+Drx_es) * Ex_es+(Dy_es+Dry_es) * Ey_es)
dW_es	Integrand for total energy	N/m	dVol_es * We_es
Ex_es	Electric field, x component	V/m	-psix
Ey_es	Electric field, y component	V/m	-psiy
grad_cn_x_cd	Concentration gradient, cn, x component	mol/m ⁴	cnx
dflux_cn_x_cd	Diffusive flux, cn,	mol/	-Dxx_cn_cd * cnx-Dxy_cn_cd * cny

	x component	(m ² *s)	
cflux_cn_x_cd	Convective flux, cn, x component	mol/(m ² *s)	cn * u_cn_cd
tflux_cn_x_cd	Total flux, cn, x component	mol/(m ² *s)	dflux_cn_x_cd+cflux_cn_x_cd
grad_cn_y_cd	Concentration gradient, cn, y component	mol/m ⁴	cny
dflux_cn_y_cd	Diffusive flux, cn, y component	mol/(m ² *s)	-Dyx_cn_cd * cnx-Dyy_cn_cd * cny
cflux_cn_y_cd	Convective flux, cn, y component	mol/(m ² *s)	cn * v_cn_cd
tflux_cn_y_cd	Total flux, cn, y component	mol/(m ² *s)	dflux_cn_y_cd+cflux_cn_y_cd
beta_cn_x_cd	Convective field, cn, x component	m/s	u_cn_cd
beta_cn_y_cd	Convective field, cn, y component	m/s	v_cn_cd
grad_cn_cd	Concentration gradient, cn	mol/m ⁴	sqrt(grad_cn_x_cd ² +grad_cn_y_cd ²)
dflux_cn_cd	Diffusive flux, cn	mol/(m ² *s)	sqrt(dflux_cn_x_cd ² +dflux_cn_y_cd ²)
cflux_cn_cd	Convective flux, cn	mol/(m ² *s)	sqrt(cflux_cn_x_cd ² +cflux_cn_y_cd ²)
tflux_cn_cd	Total flux, cn	mol/(m ² *s)	sqrt(tflux_cn_x_cd ² +tflux_cn_y_cd ²)
cellPe_cn_cd	Cell Peclet number, cn	1	h * sqrt(beta_cn_x_cd ² +beta_cn_y_cd ²)/Dm_cn_cd
Dm_cn_cd	Mean diffusion coefficient, cn	m ² /s	(Dxx_cn_cd * u_cn_cd ² +Dxy_cn_cd * u_cn_cd * v_cn_cd+Dyx_cn_cd * v_cn_cd * u_cn_cd+Dyy_cn_cd * v_cn_cd ²)/(u_cn_cd ² +v_cn_cd ² +eps)
res_cn_cd	Equation residual for cn	mol/(m ³ *s)	-Dxx_cn_cd * cnxx-Dxy_cn_cd * cnxy+cnx * u_cn_cd-Dyx_cn_cd * cnyx-Dyy_cn_cd * cnyy+cny * v_cn_cd-R_cn_cd
res_sc_cn_cd	Shock capturing residual for cn	mol/(m ³ *s)	cnx * u_cn_cd+cny * v_cn_cd-R_cn_cd
da_cn_cd	Total time scale factor, cn	1	Dts_cn_cd
grad_cp_x_cd2	Concentration gradient, cp, x component	mol/m ⁴	cpx
dflux_cp_x_cd2	Diffusive flux, cp, x component	mol/(m ² *s)	-Dxx_cp_cd2 * cpx-Dxy_cp_cd2 * cpy
cflux_cp_x_cd2	Convective flux, cp, x component	mol/(m ² *s)	cp * u_cp_cd2
tflux_cp_x_cd2	Total flux, cp, x component	mol/(m ² *s)	dflux_cp_x_cd2+cflux_cp_x_cd2
grad_cp_y_cd2	Concentration gradient, cp, y component	mol/m ⁴	cpy
dflux_cp_y_cd2	Diffusive flux, cp, y component	mol/(m ² *s)	-Dyx_cp_cd2 * cpx-Dyy_cp_cd2 * cpy
cflux_cp_y_cd2	Convective flux, cp, y component	mol/(m ² *s)	cp * v_cp_cd2
tflux_cp_y_cd2	Total flux, cp, y component	mol/(m ² *s)	dflux_cp_y_cd2+cflux_cp_y_cd2

beta_cp_x_cd2	Convective field, cp, x component	m/s	u_cp_cd2
beta_cp_y_cd2	Convective field, cp, y component	m/s	v_cp_cd2
grad_cp_cd2	Concentration gradient, cp	mol/m ⁴	sqrt(grad_cp_x_cd2 ² +grad_cp_y_cd2 ²)
dflux_cp_cd2	Diffusive flux, cp	mol/(m ² *s)	sqrt(dflux_cp_x_cd2 ² +dflux_cp_y_cd2 ²)
cflux_cp_cd2	Convective flux, cp	mol/(m ² *s)	sqrt(cflux_cp_x_cd2 ² +cflux_cp_y_cd2 ²)
tflux_cp_cd2	Total flux, cp	mol/(m ² *s)	sqrt(tflux_cp_x_cd2 ² +tflux_cp_y_cd2 ²)
cellPe_cp_cd2	Cell Peclet number, cp	1	h * sqrt(beta_cp_x_cd2 ² +beta_cp_y_cd2 ²)/Dm_cp_cd2
Dm_cp_cd2	Mean diffusion coefficient, cp	m ² /s	(Dxx_cp_cd2 * u_cp_cd2 ² +Dxy_cp_cd2 * u_cp_cd2 * v_cp_cd2+Dyx_cp_cd2 * v_cp_cd2 * u_cp_cd2+Dyy_cp_cd2 * v_cp_cd2 ²)/(u_cp_cd2 ² +v_cp_cd2 ² +eps)
res_cp_cd2	Equation residual for cp	mol/(m ³ *s)	-Dxx_cp_cd2 * cpxx-Dxy_cp_cd2 * cpxy+cpx * u_cp_cd2-Dyx_cp_cd2 * cpyx-Dyy_cp_cd2 * cpyy+cpy * v_cp_cd2-R_cp_cd2
res_sc_cp_cd2	Shock capturing residual for cp	mol/(m ³ *s)	cpx * u_cp_cd2+cpy * v_cp_cd2-R_cp_cd2
da_cp_cd2	Total time scale factor, cp	1	Dts_cp_cd2

7.2.2. Subdomain 3-5

Name	Description	Unit	Expression
dVol_es	Volume integration contribution	m	d_es
Dx_es	Electric displacement, x component	C/m ²	epsilon _{xx} _es * Ex_es+epsilon _{xy} _es * Ey_es
Dy_es	Electric displacement, y component	C/m ²	epsilon _{yx} _es * Ex_es+epsilon _{yy} _es * Ey_es
epsilon_es	Permittivity	F/m	epsilon ₀ _es * epsilon _r _es
epsilon _{xx} _es	Permittivity, xx component	F/m	epsilon ₀ _es * epsilon _{rx} _es
epsilon _{xy} _es	Permittivity, xy component	F/m	epsilon ₀ _es * epsilon _{rx} _es
epsilon _{yx} _es	Permittivity, yx component	F/m	epsilon ₀ _es * epsilon _{ry} _es
epsilon _{yy} _es	Permittivity, yy component	F/m	epsilon ₀ _es * epsilon _{ry} _es
normE_es	Electric field, norm	V/m	sqrt(abs(Ex_es) ² +abs(Ey_es) ²)
normD_es	Electric displacement, norm	C/m ²	sqrt(abs(Dx_es) ² +abs(Dy_es) ²)
normDr_es	Remanent displacement, norm	C/m ²	sqrt(abs(Drx_es) ² +abs(Dry_es) ²)
normP_es	Electric polarization, norm	C/m ²	sqrt(abs(Px_es) ² +abs(Py_es) ²)
We_es	Electric energy density	J/m ³	0.5 * ((Dx_es+Drx_es) * Ex_es+(Dy_es+Dry_es) * Ey_es)
dW_es	Integrand for total energy	N/m	dVol_es * We_es
Ex_es	Electric field, x component	V/m	-psix
Ey_es	Electric field, y component	V/m	-psiy
grad_cn_x_cd	Concentration gradient, cn, x component	mol/m ⁴	
dflux_cn_x_cd	Diffusive flux, cn, x component	mol/(m ² *s)	
cflux_cn_x_cd	Convective flux, cn, x component	mol/(m ² *s)	
tflux_cn_x_cd	Total flux, cn, x component	mol/	

file://C:\Documents and Settings\BCANNON\Desktop\PN Junction Air Cases\Segmented ... 4/20/2010

grad_cn_y_cd	Concentration gradient, cn, y component	mol/m^4	
dflux_cn_y_cd	Diffusive flux, cn, y component	$\text{mol}/(\text{m}^2\text{s})$	
cflux_cn_y_cd	Convective flux, cn, y component	$\text{mol}/(\text{m}^2\text{s})$	
tflux_cn_y_cd	Total flux, cn, y component	$\text{mol}/(\text{m}^2\text{s})$	
beta_cn_x_cd	Convective field, cn, x component	m/s	
beta_cn_y_cd	Convective field, cn, y component	m/s	
grad_cn_cd	Concentration gradient, cn	mol/m^4	
dflux_cn_cd	Diffusive flux, cn	$\text{mol}/(\text{m}^2\text{s})$	
cflux_cn_cd	Convective flux, cn	$\text{mol}/(\text{m}^2\text{s})$	
tflux_cn_cd	Total flux, cn	$\text{mol}/(\text{m}^2\text{s})$	
cellPe_cn_cd	Cell Peclet number, cn	1	
Dm_cn_cd	Mean diffusion coefficient, cn	m^2/s	
res_cn_cd	Equation residual for cn	$\text{mol}/(\text{m}^3\text{s})$	
res_sc_cn_cd	Shock capturing residual for cn	$\text{mol}/(\text{m}^3\text{s})$	
da_cn_cd	Total time scale factor, cn	1	
grad_cp_x_cd2	Concentration gradient, cp, x component	mol/m^4	
dflux_cp_x_cd2	Diffusive flux, cp, x component	$\text{mol}/(\text{m}^2\text{s})$	
cflux_cp_x_cd2	Convective flux, cp, x component	$\text{mol}/(\text{m}^2\text{s})$	
tflux_cp_x_cd2	Total flux, cp, x component	$\text{mol}/(\text{m}^2\text{s})$	
grad_cp_y_cd2	Concentration gradient, cp, y component	mol/m^4	
dflux_cp_y_cd2	Diffusive flux, cp, y component	$\text{mol}/(\text{m}^2\text{s})$	
cflux_cp_y_cd2	Convective flux, cp, y component	$\text{mol}/(\text{m}^2\text{s})$	
tflux_cp_y_cd2	Total flux, cp, y component	$\text{mol}/(\text{m}^2\text{s})$	
beta_cp_x_cd2	Convective field, cp, x component	m/s	
beta_cp_y_cd2	Convective field, cp, y component	m/s	
grad_cp_cd2	Concentration gradient, cp	mol/m^4	
dflux_cp_cd2	Diffusive flux, cp	$\text{mol}/(\text{m}^2\text{s})$	
cflux_cp_cd2	Convective flux, cp	$\text{mol}/(\text{m}^2\text{s})$	
tflux_cp_cd2	Total flux, cp	$\text{mol}/(\text{m}^2\text{s})$	
cellPe_cp_cd2	Cell Peclet number, cp	1	

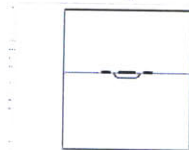
Dm_cp_cd2	Mean diffusion coefficient, cp	m ² /s	
res_cp_cd2	Equation residual for cp	mol/ (m ³ *s)	
res_sc_cp_cd2	Shock capturing residual for cp	mol/ (m ³ *s)	
da_cp_cd2	Total time scale factor, cp	1	

Appendix C: COMSOL Settings for p-n Junction Geometry #2

The following is a COMSOL auto-generated report that corresponds to the FEM simulation results that were presented in Section 2.5 and Section 2.6. The report provides information about FEM model properties, meshing settings, boundary conditions, solver settings, solver variables, constants used, etc.



p-well Geometry



1. Model Properties

Property	Value
Model name	p-well Geometry
Author	COMSOL
Company	COMSOL
Department	
Reference	Copyright (c) 1998-2008 by COMSOL AB
URL	www.comsol.com
Saved date	Feb 22, 2010 5:45:21 PM
Creation date	Nov 17, 2008 7:33:45 PM
COMSOL version	COMSOL 3.5.0.603

File name: C:\Documents and Settings\BCANNON\Desktop\PWWell Starting 2-12-10\1GHZ 4 Periods Good Transient.mph

Application modes and modules used in this model:

- Geom1 (2D)
 - Electrostatics
 - Convection and Diffusion
 - Convection and Diffusion
 - Weak Form, Boundary

1.1. Model description

Semiconductor Diode

A semiconductor device model featuring a diode with p- and n-type regions. The image shows the hole concentration for 0.5V forward bias.

2. Constants

Name	Expression	Value	Description
q	1.602e-19[C]		Elementary charge
T	300[K]		Room temperature

file://C:\Documents and Settings\BCANNON\Desktop\PWWell Starting 2-12-10\1GHZ 4 Pe... 4/20/2010

k	1.38e-23[J/K]	Boltzmann constant
epsilon_r	11.8	Rel. permittivity for Si
ni	1.46e10[1/cm^3]	Intrinsic concentration for Si
mun	800[cm^2/(V*s)]	Electron mobility for Si
mup	200[cm^2/(V*s)]	Hole mobility for Si
Dn	k^*T/q^*mun	Electron diffusivity
Dp	k^*T/q^*mup	Hole diffusivity
taun	0.1[us]	Electron life time
taup	0.1[us]	Hole life time
c	$q/(k^*T)$	Reciprocal thermal voltage
y1	18[um]	Diode dimension
x1	5[um]	Diode dimension
ju	1[um]	Junction depth
ac	2[um]	Anode dimension
NAPmax	1e16[1/cm^3]	Maximum p-type doping
NDn	1e15[1/cm^3]	Drift layer n-type doping
NDnmax	1e16[1/cm^3]	Maximum n-type doping
ch	$ju/sqrt(log(NAPmax/NDn))$	Doping fall-off constant
Va	0[V]	Applied voltage

3. Geom1

Space dimensions: 2D

Independent variables: x, y, z

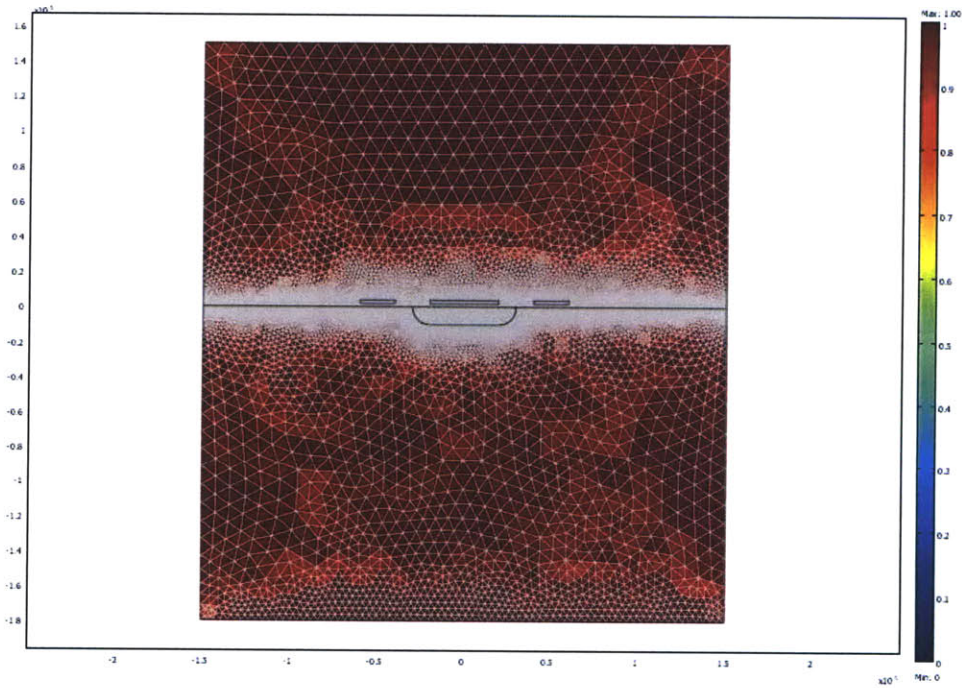
3.1. Scalar Expressions

Name	Expression	Unit	Description
N	$NDn+NDnmax*exp(-((y+y1)/ch)^2)-NAPmax*exp(-(y/ch)^2)*((x-ac)+(x>=ac)*exp(-((x-ac)/ch)^2)+(x<=-ac)*exp(-((x+ac)/ch)^2))$	1/m^3	Doping concentration
n_init	$(abs(N)/2+sqrt(N^2/4+ni^2))*(N>=0)+ni^2/(abs(N)/2+sqrt(N^2/4+ni^2))*(N<0)$	1/m^3	Charge neutrality electron concentration
p_init	$(abs(N)/2+sqrt(N^2/4+ni^2))*(N<0)+ni^2/(abs(N)/2+sqrt(N^2/4+ni^2))*(N>=0)$	1/m^3	Charge neutrality hole concentration
psi_init	$1/c*(-log(p_init/ni)*(N<0)+log(n_init/ni)*(N>=0))$	V	Charge neutrality voltage
RSRH	$(cn^*cp-ni^2)/(taup^*(cn+ni)+taun^*(cp+ni))$		Recombination term

3.2. Mesh

3.2.1. Mesh Statistics

Number of degrees of freedom	189018
Number of mesh points	21963
Number of elements	43688
Triangular	43688
Quadrilateral	0
Number of boundary elements	1344
Number of vertex elements	33
Minimum element quality	0.62
Element area ratio	0



3.3. Application Mode: Electrostatics (es)

Application mode type: Electrostatics

Application mode name: es

3.3.1. Scalar Variables

Name	Variable	Value	Unit	Description
epsilon0	epsilon0_es	8.854187817e-12	F/m	Permittivity of vacuum

3.3.2. Application Mode Properties

Property	Value
Default element type	Lagrange - Quadratic
Input property	Forced voltage
Frame	Frame (ref)
Weak constraints	Off
Constraint type	Ideal

3.3.3. Variables

file://C:\Documents and Settings\B CANNON\Desktop\PWell Starting 2-12-10\1GHZ 4 Pe... 4/20/2010

Dependent variables: psi

Shape functions: shlag(2,'psi')

Interior boundaries active

3.3.4. Boundary Settings

Boundary		1, 3, 5, 32-33	2, 18	12, 19, 34-35
Type		Zero charge/Symmetry	Electric potential	Continuity
Surface charge density (rhos)	C/m ²	0	0	0
Electric potential (V0)	V	0	psi_init	0

Boundary		13, 20	4, 11, 24, 26	14-17, 21-23, 25
Type		Surface charge	Surface charge	Electric potential
Surface charge density (rhos)	C/m ²	rhos	rhos	0
Electric potential (V0)	V	psi_init	0	5*sin(2*pi*1e9*t)

Boundary		6-10, 27-31
Type		Electric potential
Surface charge density (rhos)	C/m ²	0
Electric potential (V0)	V	-5*sin(2*pi*1e9*t)

3.3.5. Subdomain Settings

Subdomain		1, 4	2-3, 5-6
Relative permittivity (epsilon_r)	1	{epsilon_r,0;0,epsilon_r}	{1,0;0,1}
Space charge density (rho)	C/m ³	q*(N-cn+cp)	0

Subdomain initial value	1, 4	2-3, 5-6
Electric potential (psi)	V psi_init	0

3.4. Application Mode: Convection and Diffusion (cd)

Application mode type: Convection and Diffusion

Application mode name: cd

3.4.1. Application Mode Properties

Property	Value
Default element type	Lagrange - Quadratic
Analysis type	Transient
Equation form	Conservative
Frame	Frame (ref)
Weak constraints	On
Constraint type	Ideal

3.4.2. Variables

Dependent variables: cn

Shape functions: shlag(2,'lm2'), shlag(2,'cn')

Interior boundaries active

3.4.3. Boundary Settings

Boundary		1, 32	2, 18	3, 5-10, 12, 14-17, 19, 21-23, 25, 27-31, 33-35
Type		Insulation/Symmetry	Concentration	Continuity
Concentration (c0)	mol/m ³	0	n_init	0

Boundary		4, 11, 24, 26	13, 20
Type		Convective flux	Convective flux
Concentration (c0)	mol/m ³	0	n_init

3.4.4. Subdomain Settings

Subdomain		1, 4
Shape functions (shape)		shlag(2,'lm2') shlag(2,'cn')
Integration order (gporder)		4
Diffusion coefficient (D)	m ² /s	Dn
Reaction rate (R)	mol/(m ³ Πs)	-RSRH
x-velocity (u)	m/s	mun*psix
y-velocity (v)	m/s	mun*psiy

Subdomain initial value		1, 4
Concentration, cn (cn)	mol/m ³	n_init

3.5. Application Mode: Convection and Diffusion (cd2)

Application mode type: Convection and Diffusion

Application mode name: cd2

3.5.1. Application Mode Properties

Property	Value
Default element type	Lagrange - Quadratic
Analysis type	Transient
Equation form	Conservative
Frame	Frame (ref)
Weak constraints	On
Constraint type	Ideal

3.5.2. Variables

Dependent variables: cp

Shape functions: shlag(2,'lm3'), shlag(2,'cp')

Interior boundaries not active

3.5.3. Boundary Settings

Boundary		1, 32	2, 18	4, 11, 24, 26
Type		Insulation/Symmetry	Concentration	Convective flux
Concentration (c0)	mol/m ³	0	p_init	0

Boundary		13, 20
Type		Convective flux
Concentration (c0)	mol/m ³	p_init

3.5.4. Subdomain Settings

Subdomain		1, 4
Shape functions (shape)		shlag(2,'lm3') shlag(2,'cp')
Integration order (gorder)		4
Diffusion coefficient (D)	m ² /s	Dp
Reaction rate (R)	mol/(m ³ ·s)	-RSRH
x-velocity (u)	m/s	-mup*psix
y-velocity (v)	m/s	-mup*psiy

Subdomain initial value		1, 4
Concentration, cp (cp)	mol/m ³	p_init

3.6. Application Mode: Weak Form, Boundary (wb)

Application mode type: Weak Form, Boundary

Application mode name: wb

3.6.1. Application Mode Properties

Property	Value
Default element type	Lagrange - Quadratic
Wave extension	Off
Frame	Frame (ref)
Weak constraints	Off

3.6.2. Variables

Dependent variables: rhos, rhos_t

Shape functions: shlag(2,'rhos')

Interior boundaries not active

3.6.3. Boundary Settings

Boundary		4, 11, 13, 20, 24, 26
Weak term (weak)		rhos_test*(-q*ntflux_cn_cd+q*ntflux_cp_cd2)
Time-dependent weak term (dweak)		rhos_test*rhos_time

file://C:\Documents and Settings\BCANNON\Desktop\PWell Starting 2-12-10\1GHZ 4 Pe... 4/20/2010

4. Integration Coupling Variables

4.1. Geom1

4.1.1. Source Boundary: 2, 18

Name	Value
Variable name	lc
Expression	$1e-6*q*(lm2-lm3)$
Order	4
Global	Yes

5. Solver Settings

Solve using a script: off

Auto select solver	On
Solver	Time dependent
Solution form	Automatic
Symmetric	auto
Adaptive mesh refinement	Off
Optimization/Sensitivity	Off
Plot while solving	On

5.1. Direct (UMFPACK)

Solver type: Linear system solver

Parameter	Value
Pivot threshold	0.1
Memory allocation factor	0.7

5.2. Time Stepping

Parameter	Value
Times	range(0,1e-11,4e-9)
Relative tolerance	0.001
Absolute tolerance	0.00010
Times to store in output	Specified times
Time steps taken by solver	Free
Maximum BDF order	5
Singular mass matrix	Maybe
Consistent initialization of DAE systems	Backward Euler
Error estimation strategy	Include algebraic
Allow complex numbers	Off

5.3. Advanced

Parameter	Value
Constraint handling method	Elimination

Null-space function	Automatic
Automatic assembly block size	On
Assembly block size	1000
Use Hermitian transpose of constraint matrix and in symmetry detection	Off
Use complex functions with real input	Off
Stop if error due to undefined operation	On
Store solution on file	Off
Type of scaling	Automatic
Manual scaling	
Row equilibration	On
Manual control of reassembly	Off
Load constant	On
Constraint constant	On
Mass constant	On
Damping (mass) constant	On
Jacobian constant	On
Constraint Jacobian constant	On

6. Variables

6.1. Boundary

6.1.1. Boundary 1-2, 4, 11-13, 18-20, 24, 26, 32, 34-35

Name	Description	Unit	Expression
unTE _x _{es}	Maxwell surface stress tensor (x)	Pa	$-0.5 * (up(Dx_{es}) * up(Ex_{es}) + up(Dy_{es}) * up(Ey_{es})) * dnx + (dnx * up(Dx_{es}) + dny * up(Dy_{es})) * up(Ex_{es})$
unTE _y _{es}	Maxwell surface stress tensor (y)	Pa	$-0.5 * (up(Dx_{es}) * up(Ex_{es}) + up(Dy_{es}) * up(Ey_{es})) * dny + (dnx * up(Dx_{es}) + dny * up(Dy_{es})) * up(Ey_{es})$
dnTE _x _{es}	Maxwell surface stress tensor (x)	Pa	$-0.5 * (down(Dx_{es}) * down(Ex_{es}) + down(Dy_{es}) * down(Ey_{es})) * unx + (unx * down(Dx_{es}) + uny * down(Dy_{es})) * down(Ex_{es})$
dnTE _y _{es}	Maxwell surface stress tensor (y)	Pa	$-0.5 * (down(Dx_{es}) * down(Ex_{es}) + down(Dy_{es}) * down(Ey_{es})) * uny + (unx * down(Dx_{es}) + uny * down(Dy_{es})) * down(Ey_{es})$
unTx _{es}	Exterior Maxwell stress tensor (u), x component	Pa	unTE _x _{es} + unTM _x _{es}
unTM _x _{es}	Exterior magnetic Maxwell stress tensor (u), x component	Pa	0
unTy _{es}	Exterior Maxwell stress tensor (u), y component	Pa	unTE _y _{es} + unTM _y _{es}
unTM _y _{es}	Exterior magnetic Maxwell stress tensor (u), y component	Pa	0
dnTx _{es}	Exterior Maxwell stress tensor (d), x component	Pa	dnTE _x _{es} + dnTM _x _{es}
dnTM _x _{es}	Exterior magnetic Maxwell stress tensor (d), x component	Pa	0
dnTy _{es}	Exterior Maxwell stress tensor (d), y component	Pa	dnTE _y _{es} + dnTM _y _{es}
dnTM _y _{es}	Exterior magnetic Maxwell	Pa	0

file://C:\Documents and Settings\BCANNON\Desktop\PWell Starting 2-12-10\1GHZ 4 Pe... 4/20/2010

	stress tensor (d), y component		
dVolbnd_es	Volume integration contribution	m	d_es
nD_es	Surface charge density	C/m^2	unx * (down(Dx_es)-up(Dx_es))+uny * (down(Dy_es)-up(Dy_es))
ndflux_cn_cd	Normal diffusive flux, cn	mol/(m^2*s)	nx_cd * dflux_cn_x_cd+ny_cd * dflux_cn_y_cd
ncflux_cn_cd	Normal convective flux, cn	mol/(m^2*s)	nx_cd * cflux_cn_x_cd+ny_cd * cflux_cn_y_cd
ntflux_cn_cd	Normal total flux, cn	mol/(m^2*s)	nx_cd * tflux_cn_x_cd+ny_cd * tflux_cn_y_cd
ndflux_cp_cd2	Normal diffusive flux, cp	mol/(m^2*s)	nx_cd2 * dflux_cp_x_cd2+ny_cd2 * dflux_cp_y_cd2
ncflux_cp_cd2	Normal convective flux, cp	mol/(m^2*s)	nx_cd2 * cflux_cp_x_cd2+ny_cd2 * cflux_cp_y_cd2
ntflux_cp_cd2	Normal total flux, cp	mol/(m^2*s)	nx_cd2 * tflux_cp_x_cd2+ny_cd2 * tflux_cp_y_cd2

6.1.2. Boundary 3, 5-10, 14-17, 21-23, 25, 27-31, 33

Name	Description	Unit	Expression
unTE _x _es	Maxwell surface stress tensor (x)	Pa	-0.5 * (up(Dx_es) * up(Ex_es)+up(Dy_es) * up(Ey_es)) * dnx+(dnx * up(Dx_es)+dny * up(Dy_es)) * up(Ex_es)
unTE _y _es	Maxwell surface stress tensor (y)	Pa	-0.5 * (up(Dx_es) * up(Ex_es)+up(Dy_es) * up(Ey_es)) * dny+(dnx * up(Dx_es)+dny * up(Dy_es)) * up(Ey_es)
dnTE _x _es	Maxwell surface stress tensor (x)	Pa	-0.5 * (down(Dx_es) * down(Ex_es)+down(Dy_es) * down(Ey_es)) * unx+(unx * down(Dx_es)+uny * down(Dy_es)) * down(Ex_es)
dnTE _y _es	Maxwell surface stress tensor (y)	Pa	-0.5 * (down(Dx_es) * down(Ex_es)+down(Dy_es) * down(Ey_es)) * uny+(unx * down(Dx_es)+uny * down(Dy_es)) * down(Ey_es)
unT _x _es	Exterior Maxwell stress tensor (u), x component	Pa	unTE _x _es+unTM _x _es
unTM _x _es	Exterior magnetic Maxwell stress tensor (u), x component	Pa	0
unT _y _es	Exterior Maxwell stress tensor (u), y component	Pa	unTE _y _es+unTM _y _es
unTM _y _es	Exterior magnetic Maxwell stress tensor (u), y component	Pa	0
dnT _x _es	Exterior Maxwell stress tensor (d), x component	Pa	dnTE _x _es+dnTM _x _es
dnTM _x _es	Exterior magnetic Maxwell stress tensor (d), x component	Pa	0
dnT _y _es	Exterior Maxwell stress tensor (d), y component	Pa	dnTE _y _es+dnTM _y _es
dnTM _y _es	Exterior magnetic Maxwell stress tensor (d), y component	Pa	0
dVolbnd_es	Volume integration contribution	m	d_es
nD_es	Surface charge density	C/m^2	unx * (down(Dx_es)-up(Dx_es))+uny * (down(Dy_es)-up(Dy_es))

			(Dy_es))
ndflux_cn_cd	Normal diffusive flux, cn	mol/ (m ² *s)	
ncflux_cn_cd	Normal convective flux, cn	mol/ (m ² *s)	
ntflux_cn_cd	Normal total flux, cn	mol/ (m ² *s)	
ndflux_cp_cd2	Normal diffusive flux, cp	mol/ (m ² *s)	
ncflux_cp_cd2	Normal convective flux, cp	mol/ (m ² *s)	
ntflux_cp_cd2	Normal total flux, cp	mol/ (m ² *s)	

6.2. Subdomain

6.2.1. Subdomain 1, 4

Name	Description	Unit	Expression
dVol_es	Volume integration contribution	m	d_es
Dx_es	Electric displacement, x component	C/m ²	epsilon _{xx} _es * Ex_es+epsilon _{xy} _es * Ey_es
Dy_es	Electric displacement, y component	C/m ²	epsilon _{yx} _es * Ex_es+epsilon _{yy} _es * Ey_es
epsilon_es	Permittivity	F/m	epsilon ₀ _es * epsilon _r _es
epsilon _{xx} _es	Permittivity, xx component	F/m	epsilon ₀ _es * epsilon _{xx} _es
epsilon _{xy} _es	Permittivity, xy component	F/m	epsilon ₀ _es * epsilon _{xy} _es
epsilon _{yx} _es	Permittivity, yx component	F/m	epsilon ₀ _es * epsilon _{yx} _es
epsilon _{yy} _es	Permittivity, yy component	F/m	epsilon ₀ _es * epsilon _{yy} _es
normE_es	Electric field, norm	V/m	sqrt(abs(Ex_es)^2+abs(Ey_es)^2)
normD_es	Electric displacement, norm	C/m ²	sqrt(abs(Dx_es)^2+abs(Dy_es)^2)
normDr_es	Remanent displacement, norm	C/m ²	sqrt(abs(Drx_es)^2+abs(Dry_es)^2)
normP_es	Electric polarization, norm	C/m ²	sqrt(abs(Px_es)^2+abs(Py_es)^2)
We_es	Electric energy density	J/m ³	0.5 * ((Dx_es+Drx_es) * Ex_es+(Dy_es+Dry_es) * Ey_es)
dW_es	Integrand for total energy	N/m	dVol_es * We_es
Ex_es	Electric field, x component	V/m	-psix
Ey_es	Electric field, y component	V/m	-psiy

file://C:\Documents and Settings\BCANNON\Desktop\PWell Starting 2-12-10\1GHZ 4 Pe... 4/20/2010

grad_cn_x_cd	Concentration gradient, cn, x component	mol/m ⁴	cnx
dflux_cn_x_cd	Diffusive flux, cn, x component	mol/(m ² *s)	-Dxx_cn_cd * cnx-Dxy_cn_cd * cny
cflux_cn_x_cd	Convective flux, cn, x component	mol/(m ² *s)	cn * u_cn_cd
tflux_cn_x_cd	Total flux, cn, x component	mol/(m ² *s)	dflux_cn_x_cd+cflux_cn_x_cd
grad_cn_y_cd	Concentration gradient, cn, y component	mol/m ⁴	cny
dflux_cn_y_cd	Diffusive flux, cn, y component	mol/(m ² *s)	-Dyx_cn_cd * cnx-Dyy_cn_cd * cny
cflux_cn_y_cd	Convective flux, cn, y component	mol/(m ² *s)	cn * v_cn_cd
tflux_cn_y_cd	Total flux, cn, y component	mol/(m ² *s)	dflux_cn_y_cd+cflux_cn_y_cd
beta_cn_x_cd	Convective field, cn, x component	m/s	u_cn_cd
beta_cn_y_cd	Convective field, cn, y component	m/s	v_cn_cd
grad_cn_cd	Concentration gradient, cn	mol/m ⁴	sqrt(grad_cn_x_cd ² +grad_cn_y_cd ²)
dflux_cn_cd	Diffusive flux, cn	mol/(m ² *s)	sqrt(dflux_cn_x_cd ² +dflux_cn_y_cd ²)
cflux_cn_cd	Convective flux, cn	mol/(m ² *s)	sqrt(cflux_cn_x_cd ² +cflux_cn_y_cd ²)
tflux_cn_cd	Total flux, cn	mol/(m ² *s)	sqrt(tflux_cn_x_cd ² +tflux_cn_y_cd ²)
cellPe_cn_cd	Cell Peclet number, cn	1	h * sqrt(beta_cn_x_cd ² +beta_cn_y_cd ²)/Dm_cn_cd
Dm_cn_cd	Mean diffusion coefficient, cn	m ² /s	(Dxx_cn_cd * u_cn_cd ² +Dxy_cn_cd * u_cn_cd * v_cn_cd+Dyx_cn_cd * v_cn_cd * u_cn_cd+Dyy_cn_cd * v_cn_cd ²)/(u_cn_cd ² +v_cn_cd ² +eps)
res_cn_cd	Equation residual for cn	mol/(m ³ *s)	-Dxx_cn_cd * cnxx-Dxy_cn_cd * cnxy+cnx * u_cn_cd-Dyx_cn_cd * cnyx-Dyy_cn_cd * cnyy+cny * v_cn_cd-R_cn_cd
res_sc_cn_cd	Shock capturing residual for cn	mol/(m ³ *s)	cnx * u_cn_cd+cny * v_cn_cd-R_cn_cd
da_cn_cd	Total time scale factor, cn	1	Dts_cn_cd
grad_cp_x_cd2	Concentration gradient, cp, x component	mol/m ⁴	cpx
dflux_cp_x_cd2	Diffusive flux, cp, x component	mol/(m ² *s)	-Dxx_cp_cd2 * cpx-Dxy_cp_cd2 * cpy
cflux_cp_x_cd2	Convective flux, cp, x component	mol/(m ² *s)	cp * u_cp_cd2
tflux_cp_x_cd2	Total flux, cp, x component	mol/(m ² *s)	dflux_cp_x_cd2+cflux_cp_x_cd2
grad_cp_y_cd2	Concentration gradient, cp, y component	mol/m ⁴	cpy
dflux_cp_y_cd2	Diffusive flux, cp, y component	mol/(m ² *s)	-Dyx_cp_cd2 * cpx-Dyy_cp_cd2 * cpy

	y component	(m ² *s)	
cflux_cp_y_cd2	Convective flux, cp, y component	mol/(m ² *s)	cp * v_cp_cd2
tflux_cp_y_cd2	Total flux, cp, y component	mol/(m ² *s)	dflux_cp_y_cd2+cflux_cp_y_cd2
beta_cp_x_cd2	Convective field, cp, x component	m/s	u_cp_cd2
beta_cp_y_cd2	Convective field, cp, y component	m/s	v_cp_cd2
grad_cp_cd2	Concentration gradient, cp	mol/m ⁴	sqrt(grad_cp_x_cd2 ² +grad_cp_y_cd2 ²)
dflux_cp_cd2	Diffusive flux, cp	mol/(m ² *s)	sqrt(dflux_cp_x_cd2 ² +dflux_cp_y_cd2 ²)
cflux_cp_cd2	Convective flux, cp	mol/(m ² *s)	sqrt(cflux_cp_x_cd2 ² +cflux_cp_y_cd2 ²)
tflux_cp_cd2	Total flux, cp	mol/(m ² *s)	sqrt(tflux_cp_x_cd2 ² +tflux_cp_y_cd2 ²)
cellPe_cp_cd2	Cell Peclet number, cp	1	h * sqrt(beta_cp_x_cd2 ² +beta_cp_y_cd2 ²)/Dm_cp_cd2
Dm_cp_cd2	Mean diffusion coefficient, cp	m ² /s	(Dxx_cp_cd2 * u_cp_cd2 ² +Dxy_cp_cd2 * u_cp_cd2 * v_cp_cd2+Dyx_cp_cd2 * v_cp_cd2 * u_cp_cd2+Dyy_cp_cd2 * v_cp_cd2 ²)/(u_cp_cd2 ² +v_cp_cd2 ² +eps)
res_cp_cd2	Equation residual for cp	mol/(m ³ *s)	-Dxx_cp_cd2 * cpxx-Dxy_cp_cd2 * cpxy+cpx * u_cp_cd2-Dyx_cp_cd2 * cpyx-Dyy_cp_cd2 * cpyy+cpy * v_cp_cd2-R_cp_cd2
res_sc_cp_cd2	Shock capturing residual for cp	mol/(m ³ *s)	cpx * u_cp_cd2+cpy * v_cp_cd2-R_cp_cd2
da_cp_cd2	Total time scale factor, cp	1	Dts_cp_cd2

6.2.2. Subdomain 2-3, 5-6

Name	Description	Unit	Expression
dVol_es	Volume integration contribution	m	d_es
Dx_es	Electric displacement, x component	C/m ²	epsilon _{xx} * Ex_es+epsilon _{xy} * Ey_es
Dy_es	Electric displacement, y component	C/m ²	epsilon _{yx} * Ex_es+epsilon _{yy} * Ey_es
epsilon_es	Permittivity	F/m	epsilon ₀ * epsilon _r
epsilon _{xx} _es	Permittivity, xx component	F/m	epsilon ₀ * epsilon _{rx}
epsilon _{xy} _es	Permittivity, xy component	F/m	epsilon ₀ * epsilon _{rx}
epsilon _{yx} _es	Permittivity, yx component	F/m	epsilon ₀ * epsilon _{ry}
epsilon _{yy} _es	Permittivity, yy component	F/m	epsilon ₀ * epsilon _{ry}
normE_es	Electric field, norm	V/m	sqrt(abs(Ex_es) ² +abs(Ey_es) ²)
normD_es	Electric displacement, norm	C/m ²	sqrt(abs(Dx_es) ² +abs(Dy_es) ²)
normDr_es	Remanent displacement, norm	C/m ²	sqrt(abs(Drx_es) ² +abs(Dry_es) ²)
normP_es	Electric polarization, norm	C/m ²	sqrt(abs(Px_es) ² +abs(Py_es) ²)
We_es	Electric energy density	J/m ³	0.5 * ((Dx_es+Drx_es) * Ex_es+(Dy_es+Dry_es) * Ey_es)
dW_es	Integrand for total energy	N/m	dVol_es * We_es
Ex_es	Electric field, x component	V/m	-psix
Ey_es	Electric field, y component	V/m	-psiy
grad_cn_x_cd	Concentration gradient, cn, x component	mol/m ⁴	

file://C:\Documents and Settings\BCANNON\Desktop\PWell Starting 2-12-10\1GHZ 4 Pe... 4/20/2010

dflux_cn_x_cd	Diffusive flux, cn, x component	mol/ (m ² *s)	
cflux_cn_x_cd	Convective flux, cn, x component	mol/ (m ² *s)	
tflux_cn_x_cd	Total flux, cn, x component	mol/ (m ² *s)	
grad_cn_y_cd	Concentration gradient, cn, y component	mol/m ⁴	
dflux_cn_y_cd	Diffusive flux, cn, y component	mol/ (m ² *s)	
cflux_cn_y_cd	Convective flux, cn, y component	mol/ (m ² *s)	
tflux_cn_y_cd	Total flux, cn, y component	mol/ (m ² *s)	
beta_cn_x_cd	Convective field, cn, x component	m/s	
beta_cn_y_cd	Convective field, cn, y component	m/s	
grad_cn_cd	Concentration gradient, cn	mol/m ⁴	
dflux_cn_cd	Diffusive flux, cn	mol/ (m ² *s)	
cflux_cn_cd	Convective flux, cn	mol/ (m ² *s)	
tflux_cn_cd	Total flux, cn	mol/ (m ² *s)	
cellPe_cn_cd	Cell Peclet number, cn	1	
Dm_cn_cd	Mean diffusion coefficient, cn	m ² /s	
res_cn_cd	Equation residual for cn	mol/ (m ³ *s)	
res_sc_cn_cd	Shock capturing residual for cn	mol/ (m ³ *s)	
da_cn_cd	Total time scale factor, cn	1	
grad_cp_x_cd2	Concentration gradient, cp, x component	mol/m ⁴	
dflux_cp_x_cd2	Diffusive flux, cp, x component	mol/ (m ² *s)	
cflux_cp_x_cd2	Convective flux, cp, x component	mol/ (m ² *s)	
tflux_cp_x_cd2	Total flux, cp, x component	mol/ (m ² *s)	
grad_cp_y_cd2	Concentration gradient, cp, y component	mol/m ⁴	
dflux_cp_y_cd2	Diffusive flux, cp, y component	mol/ (m ² *s)	
cflux_cp_y_cd2	Convective flux, cp, y component	mol/ (m ² *s)	
tflux_cp_y_cd2	Total flux, cp, y component	mol/ (m ² *s)	
beta_cp_x_cd2	Convective field, cp, x component	m/s	
beta_cp_y_cd2	Convective field, cp, y component	m/s	
grad_cp_cd2	Concentration gradient, cp	mol/m ⁴	
dflux_cp_cd2	Diffusive flux, cp	mol/ (m ² *s)	

cflux_cp_cd2	Convective flux, cp	mol/ (m ² *s)	
tflux_cp_cd2	Total flux, cp	mol/ (m ² *s)	
cellPe_cp_cd2	Cell Peclet number, cp	1	
Dm_cp_cd2	Mean diffusion coefficient, cp	m ² /s	
res_cp_cd2	Equation residual for cp	mol/ (m ³ *s)	
res_sc_cp_cd2	Shock capturing residual for cp	mol/ (m ³ *s)	
da_cp_cd2	Total time scale factor, cp	1	

Appendix D: COMSOL Settings for Contaminated Photomask

The following is a COMSOL auto-generated report that corresponds to the FEM simulation results that were presented in Section 3.1. The report provides information about FEM model properties, meshing settings, boundary conditions, solver settings, solver variables, constants used, etc.



photomask Geometry



1. Model Properties

Property	Value
Model name	photomask Geometry
Author	COMSOL
Company	COMSOL
Department	
Reference	Copyright (c) 1998-2008 by COMSOL AB
URL	www.comsol.com
Saved date	Oct 20, 2009 7:38:19 PM
Creation date	Sep 19, 2008 1:22:44 PM
COMSOL version	COMSOL 3.5.0.603

File name: C:\Documents and Settings\BCANNON\Desktop\ASML 70nm diameter particle True Absorber Conductivity Values\ASML_0nm.mph

Application modes and modules used in this model:

- Geom1 (2D)
 - In-Plane Electric Currents (AC/DC Module)

2. Geom1

Space dimensions: 2D

Independent variables: x, y, z

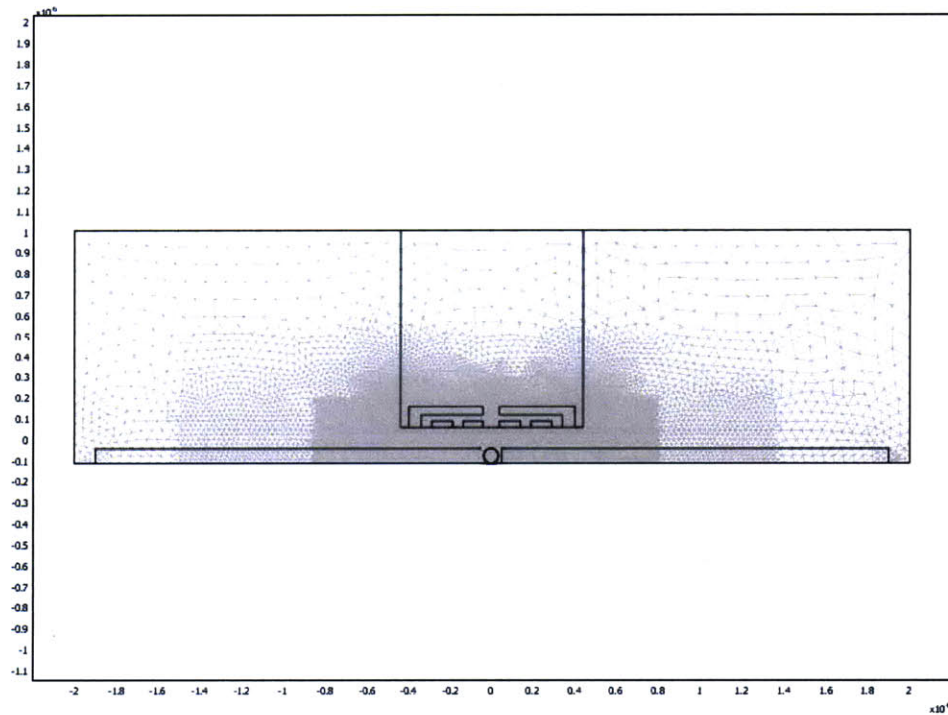
2.1. Mesh

2.1.1. Mesh Statistics

Number of degrees of freedom	161277
Number of mesh points	45221
Number of elements	89980
Triangular	89980
Quadrilateral	0

file://C:\Documents and Settings\BCANNON\Desktop\ASML 70nm diameter particle Tru... 4/20/2010

Number of boundary elements	2090
Number of vertex elements	50
Minimum element quality	0.018
Element area ratio	0



2.2. Application Mode: In-Plane Electric Currents (emqww)

Application mode type: In-Plane Electric Currents (AC/DC Module)

Application mode name: emqww

2.2.1. Scalar Variables

Name	Variable	Value	Unit	Description
epsilon0	epsilon0_emqww	8.854187817e-12	F/m	Permittivity of vacuum
mu0	mu0_emqww	4*pi* 1e-7	H/m	Permeability of vacuum
nu	nu_emqww	1e9	Hz	Frequency

2.2.2. Application Mode Properties

Property	Value

file://C:\Documents and Settings\BCANNON\Desktop\ASML 70nm diameter particle Tru... 4/20/2010

Default element type	Lagrange - Quadratic
Analysis type	Time-harmonic, electric currents
Bias application mode	None
Potentials	Electric and magnetic
Gauge fixing	Automatic
Input property	Forced voltage
Solve for	Total potential
Background field	Magnetic vector potential
Frame	Frame (ref)
Weak constraints	On
Vector element constraint	Off
Constraint type	Ideal

2.2.3. Variables

Dependent variables: V, Ax, Ay, redAx, redAy, psi

Shape functions: shlag(2,'lm1'), shlag(2,'V')

Interior boundaries active

2.2.4. Boundary Settings

Boundary	1, 56	2, 5, 38, 55	3, 9, 53
Electric potential (V0)	V 0	0	0
Port number (portnr)	7	7	1
inport	0	0	0
eltype	Electric insulation	Floating potential	Electric insulation
magtype	Magnetic insulation	Magnetic insulation	Magnetic insulation

Boundary	4, 15, 21, 28, 41, 46, 52, 54, 57-60	6, 25, 37, 39	7-8, 50
Electric potential (V0)	V 0	0	1
Port number (portnr)	1	10	5
inport	0	0	0
eltype	Continuity	Continuity	Continuity
magtype	Continuity	Continuity	Continuity

Boundary	10-14, 16, 29	17-20	22-24, 27
Electric potential (V0)	V 1	1	1
Port number (portnr)	5	3	1
inport	0	1	0
eltype	Port	Port	Port
magtype	Magnetic insulation	Magnetic insulation	Magnetic insulation

Boundary	26, 30	31-33, 40	34-36, 47-49, 51
Electric potential (V0)	V 0	-1	-1
Port number (portnr)	10	2	6
inport	0	0	0
eltype	Floating potential	Port	Port
magtype	Magnetic insulation	Magnetic insulation	Magnetic insulation



Boundary	42-45
Electric potential (V0)	V -1
Port number (portnr)	4
inport	0
eltype	Port
magtype	Magnetic insulation

2.2.5. Subdomain Settings

Subdomain	1	2, 9	3
Shape functions (shape)	shlag(2,'lm1') shlag(2,'V')	shlag(2,'lm1') shlag(2,'V')	shlag(2,'lm1') shlag(2,'V')
Integration order (gporder)	4	4	4
name			
Electric conductivity (sigma)	S/m {0,0;0,0}	{1e6,0;0,1e6}	{0,0;0,0}
Relative permittivity (epsilon)	1 {1,0;0,1}	{2,0;0,2}	{3.9,0;0,3.9}
Source point (nTsrcpnt)	{{0,0}}	{{0,0}}	{{0,0}}

Subdomain	11
Shape functions (shape)	shlag(2,'lm1') shlag(2,'V')
Integration order (gporder)	4
name	particle
Electric conductivity (sigma)	S/m {0,0;0,0}
Relative permittivity (epsilon)	1 {1,0;0,1}
Source point (nTsrcpnt)	0

3. Solver Settings

Solve using a script: off

Analysis type	Time-harmonic_electric_currents
Auto select solver	On
Solver	Stationary
Solution form	Automatic
Symmetric	auto
Adaptive mesh refinement	Off
Optimization/Sensitivity	Off
Plot while solving	Off

3.1. Direct (UMFPACK)

Solver type: Linear system solver

Parameter	Value
Pivot threshold	0.1
Memory allocation factor	0.7

3.2. Stationary

Parameter	Value
Linearity	Automatic
Relative tolerance	1.0E-6
Maximum number of iterations	25
Manual tuning of damping parameters	Off
Highly nonlinear problem	Off
Initial damping factor	1.0
Minimum damping factor	1.0E-4
Restriction for step size update	10.0

3.3. Advanced

Parameter	Value
Constraint handling method	Elimination
Null-space function	Automatic
Automatic assembly block size	On
Assembly block size	5000
Use Hermitian transpose of constraint matrix and in symmetry detection	Off
Use complex functions with real input	Off
Stop if error due to undefined operation	On
Store solution on file	Off
Type of scaling	Automatic
Manual scaling	
Row equilibration	On
Manual control of reassembly	Off
Load constant	On
Constraint constant	On
Mass constant	On
Damping (mass) constant	On
Jacobian constant	On
Constraint Jacobian constant	On

4. Variables

4.1. Boundary

4.1.1. Boundary 1, 3-4, 6-9, 15, 21, 25, 28, 37, 39, 41, 46, 50, 52-54, 56-60

Name	Description	Unit	Expression
dVolbnd_emqvw	Area integration contribution	m	d_emqvw
nJ_emqvw	Normal current density	A/m ²	$n_x \text{emqvw} * J_x \text{emqvw} + n_y \text{emqvw} * J_y \text{emqvw}$
unTExav_emqvw	Electric Maxwell surface stress tensor, time average, x component	Pa	$\text{real}(-0.25 * (\text{Ex_emqvw_up} * \text{conj}(\text{Dx_emqvw_up}) + \text{Ey_emqvw_up} * \text{conj}(\text{Dy_emqvw_up})) * \text{dnx} + 0.5 * (\text{dnx} * \text{Ex_emqvw_up} + \text{dny} * \text{Ey_emqvw_up}) * \text{conj}(\text{Dx_emqvw_up}))$
dnTExav_emqvw	Electric Maxwell surface stress tensor, time average, x component	Pa	$\text{real}(-0.25 * (\text{Ex_emqvw_down} * \text{conj}(\text{Dx_emqvw_down}) + \text{Ey_emqvw_down} * \text{conj}(\text{Dy_emqvw_down})) * \text{unx} + 0.5 * (\text{unx} * \text{Ex_emqvw_down} + \text{uny} * \text{Ey_emqvw_down}) * \text{conj}(\text{Dx_emqvw_down}))$
unTEyav_emqvw	Electric Maxwell	Pa	$\text{real}(-0.25 * (\text{Ex_emqvw_up} * \text{conj}(\text{Dx_emqvw_up}))$

	surface stress tensor, time average, y component		$+E_{y_emqvw_up} * conj(D_{y_emqvw_up}) * dny + 0.5 * (dnx * E_{x_emqvw_up} + dny * E_{y_emqvw_up}) * conj(D_{y_emqvw_up})$
dnTEyav_emqvw	Electric Maxwell surface stress tensor, time average, y component	Pa	$real(-0.25 * (E_{x_emqvw_down} * conj(D_{x_emqvw_down}) + E_{y_emqvw_down} * conj(D_{y_emqvw_down})) * uny + 0.5 * (unx * E_{x_emqvw_down} + uny * E_{y_emqvw_down}) * conj(D_{y_emqvw_down}))$
nJs_emqvw	Source current density	A/m ²	$unx * (down(J_{x_emqvw}) - up(J_{x_emqvw})) + uny * (down(J_{y_emqvw}) - up(J_{y_emqvw}))$
tEx_emqvw	Tangential electric field, x component	V/m	-VTx
tEy_emqvw	Tangential electric field, y component	V/m	-VTy
tDx_emqvw	Tangential electric displacement, x component	C/m ²	$epsilon_{0_emqvw} * epsilon_{r_bnd_emqvw} * tEx_emqvw$
tDy_emqvw	Tangential electric displacement, y component	C/m ²	$epsilon_{0_emqvw} * epsilon_{r_bnd_emqvw} * tEy_emqvw$
normtE_emqvw	Tangential electric field, norm	V/m	$sqrt(abs(tEx_emqvw)^2 + abs(tEy_emqvw)^2)$
normtD_emqvw	Tangential electric displacement, norm	C/m ²	$sqrt(abs(tDx_emqvw)^2 + abs(tDy_emqvw)^2)$
unTx_emqvw	Exterior Maxwell stress tensor (u), x component	Pa	$unTE_{x_emqvw} + unTM_{x_emqvw}$
unTE _x _emqvw	Exterior electric Maxwell stress tensor (u), x component	Pa	0
unTM _x _emqvw	Exterior magnetic Maxwell stress tensor (u), x component	Pa	0
unTy_emqvw	Exterior Maxwell stress tensor (u), y component	Pa	$unTE_{y_emqvw} + unTM_{y_emqvw}$
unTE _y _emqvw	Exterior electric Maxwell stress tensor (u), y component	Pa	0
unTM _y _emqvw	Exterior magnetic Maxwell stress tensor (u), y component	Pa	0
dnTx_emqvw	Exterior Maxwell stress tensor (d), x component	Pa	$dnTE_{x_emqvw} + dnTM_{x_emqvw}$
dnTE _x _emqvw	Exterior electric Maxwell stress tensor (d), x component	Pa	0
dnTM _x _emqvw	Exterior magnetic Maxwell stress tensor (d), x component	Pa	0
dnTy_emqvw	Exterior Maxwell stress tensor (d), y component	Pa	$dnTE_{y_emqvw} + dnTM_{y_emqvw}$
dnTE _y _emqvw	Exterior electric Maxwell stress tensor (d), y component	Pa	0

dnTMy_emqww	Exterior magnetic Maxwell stress tensor (d), y component	Pa	0
-------------	--	----	---

4.1.2. Boundary 2, 5, 10-14, 16-20, 22-24, 26-27, 29-36, 38, 40, 42-45, 47-49, 51, 55

Name	Description	Unit	Expression
dVolbnd_emqww	Area integration contribution	m	d_emqww
nJ_emqww	Normal current density	A/m ²	rx_emqww * Jx_emqww + ny_emqww * Jy_emqww
unTEXav_emqww	Electric Maxwell surface stress tensor, time average, x component	Pa	real(-0.25 * (Ex_emqww_up * conj(Dx_emqww_up) + Ey_emqww_up * conj(Dy_emqww_up)) * dnx + 0.5 * (dnx * Ex_emqww_up + dny * Ey_emqww_up) * conj(Dx_emqww_up))
dnTEXav_emqww	Electric Maxwell surface stress tensor, time average, x component	Pa	real(-0.25 * (Ex_emqww_down * conj(Dx_emqww_down) + Ey_emqww_down * conj(Dy_emqww_down)) * unx + 0.5 * (unx * Ex_emqww_down + uny * Ey_emqww_down) * conj(Dx_emqww_down))
unTEyav_emqww	Electric Maxwell surface stress tensor, time average, y component	Pa	real(-0.25 * (Ex_emqww_up * conj(Dx_emqww_up) + Ey_emqww_up * conj(Dy_emqww_up)) * dny + 0.5 * (dnx * Ex_emqww_up + dny * Ey_emqww_up) * conj(Dy_emqww_up))
dnTEyav_emqww	Electric Maxwell surface stress tensor, time average, y component	Pa	real(-0.25 * (Ex_emqww_down * conj(Dx_emqww_down) + Ey_emqww_down * conj(Dy_emqww_down)) * uny + 0.5 * (unx * Ex_emqww_down + uny * Ey_emqww_down) * conj(Dy_emqww_down))
nJs_emqww	Source current density	A/m ²	Im1/d_emqww
tEx_emqww	Tangential electric field, x component	V/m	-VTx
tEy_emqww	Tangential electric field, y component	V/m	-VTy
tDx_emqww	Tangential electric displacement, x component	C/m ²	epsilon0_emqww * epsilon0r_bnd_emqww * tEx_emqww
tDy_emqww	Tangential electric displacement, y component	C/m ²	epsilon0_emqww * epsilon0r_bnd_emqww * tEy_emqww
normtE_emqww	Tangential electric field, norm	V/m	sqrt(abs(tEx_emqww)^2 + abs(tEy_emqww)^2)
normtD_emqww	Tangential electric displacement, norm	C/m ²	sqrt(abs(tDx_emqww)^2 + abs(tDy_emqww)^2)
unTx_emqww	Exterior Maxwell stress tensor (u), x component	Pa	unTEX_emqww + unTMx_emqww
unTEX_emqww	Exterior electric Maxwell stress tensor (u), x component	Pa	0
unTMx_emqww	Exterior magnetic Maxwell stress tensor (u), x component	Pa	0
unTy_emqww	Exterior Maxwell stress tensor (u), y component	Pa	unTEy_emqww + unTMy_emqww
unTEy_emqww	Exterior electric Maxwell stress tensor (u), y component	Pa	0

unTMy_emqvw	Exterior magnetic Maxwell stress tensor (u), y component	Pa	0
dnTx_emqvw	Exterior Maxwell stress tensor (d), x component	Pa	dnTEx_emqvw+dnTMx_emqvw
dnTEx_emqvw	Exterior electric Maxwell stress tensor (d), x component	Pa	0
dnTMx_emqvw	Exterior magnetic Maxwell stress tensor (d), x component	Pa	0
dnTy_emqvw	Exterior Maxwell stress tensor (d), y component	Pa	dnTEy_emqvw+dnTMy_emqvw
dnTEy_emqvw	Exterior electric Maxwell stress tensor (d), y component	Pa	0
dnTMy_emqvw	Exterior magnetic Maxwell stress tensor (d), y component	Pa	0

4.2. Subdomain

4.2.1. Subdomain 1, 3, 11

Name	Description	Unit	Expression
dr_guess_emqvw	Width in radial direction default guess	m	0
R0_guess_emqvw	Inner radius default guess	m	0
Sx_emqvw	Infinite element x coordinate	m	x
S0x_guess_emqvw	Inner x coordinate default guess	m	0
Sdx_guess_emqvw	Width in x direction default guess	m	0
Sy_emqvw	Infinite element y coordinate	m	y
S0y_guess_emqvw	Inner y coordinate default guess	m	0
Sdy_guess_emqvw	Width in y direction default guess	m	0
delta_emqvw	Skin depth	m	$1/\text{real}(\sqrt{j * \omega_{emqvw} * \mu_{0_emqvw} * \mu_{r_emqvw} * (\sigma_{emqvw} + j * \omega_{emqvw} * \epsilon_{0_emqvw} * \epsilon_{r_{emqvw}})})$
dVol_emqvw	Volume integration contribution	m	detJ_emqvw * d_emqvw
Dx_emqvw	Electric displacement, x component	C/m ²	$\epsilon_{xx_emqvw} * E_{x_emqvw} + \epsilon_{xy_emqvw} * E_{y_emqvw}$
Dy_emqvw	Electric displacement, y component	C/m ²	$\epsilon_{yx_emqvw} * E_{x_emqvw} + \epsilon_{yy_emqvw} * E_{y_emqvw}$

epsilon_emqvw	Permittivity	F/m	epsilon0_emqvw * epsilon_r_emqvw
epsilon_xx_emqvw	Permittivity, xx component	F/m	epsilon0_emqvw * epsilon_xx_emqvw
epsilon_xy_emqvw	Permittivity, xy component	F/m	epsilon0_emqvw * epsilon_xy_emqvw
epsilon_yx_emqvw	Permittivity, yx component	F/m	epsilon0_emqvw * epsilon_yx_emqvw
epsilon_yy_emqvw	Permittivity, yy component	F/m	epsilon0_emqvw * epsilon_yy_emqvw
sigma_emqvw	Electric conductivity	S/m	sigma_xx_emqvw
Jdx_emqvw	Displacement current density, x component	A/m^2	j * omega_emqvw * Dx_emqvw
Jpx_emqvw	Potential current density, x component	A/m^2	0
Jx_emqvw	Total current density, x component	A/m^2	Jex_emqvw+Jdx_emqvw+Jpx_emqvw
Jdy_emqvw	Displacement current density, y component	A/m^2	j * omega_emqvw * Dy_emqvw
Jpy_emqvw	Potential current density, y component	A/m^2	0
Jy_emqvw	Total current density, y component	A/m^2	Jey_emqvw+Jdy_emqvw+Jpy_emqvw
normP_emqvw	Electric polarization, norm	C/m^2	sqrt(abs(Px_emqvw)^2+abs(Py_emqvw)^2)
normDr_emqvw	Remanent displacement, norm	C/m^2	sqrt(abs(Drx_emqvw)^2+abs(Dry_emqvw)^2)
normD_emqvw	Electric displacement, norm	C/m^2	sqrt(abs(Dx_emqvw)^2+abs(Dy_emqvw)^2)
normE_emqvw	Electric field, norm	V/m	sqrt(abs(Ex_emqvw)^2+abs(Ey_emqvw)^2)
normJp_emqvw	Potential current density, norm	A/m^2	sqrt(abs(Jpx_emqvw)^2+abs(Jpy_emqvw)^2)
normJd_emqvw	Displacement current density, norm	A/m^2	sqrt(abs(Jdx_emqvw)^2+abs(Jdy_emqvw)^2)
normJe_emqvw	External current density, norm	A/m^2	sqrt(abs(Jex_emqvw)^2+abs(Jey_emqvw)^2)
normJ_emqvw	Total current density, norm	A/m^2	sqrt(abs(Jx_emqvw)^2+abs(Jy_emqvw)^2)
Weav_emqvw	Electric energy density, time average	J/m^3	0.25 * real(Ex_emqvw * conj(Dx_emqvw)+Ey_emqvw * conj(Dy_emqvw))
Wav_emqvw	Total energy density, time average	J/m^3	Weav_emqvw
Qav_emqvw	Resistive heating, time average	W/m^3	0.5 * real(Jx_emqvw * conj(Ex_emqvw)+Jy_emqvw * conj(Ey_emqvw))
Ex_emqvw	Electric field, x component	V/m	-invJxx_emqvw * Vx
Ey_emqvw	Electric field, y component	V/m	-invJyy_emqvw * Vy

4.2.2. Subdomain 2, 9

Name	Description	Unit	Expression
dr_guess_emqww	Width in radial direction default guess	m	0
R0_guess_emqww	Inner radius default guess	m	0
Sx_emqww	Infinite element x coordinate	m	x
S0x_guess_emqww	Inner x coordinate default guess	m	0
Sdx_guess_emqww	Width in x direction default guess	m	0
Sy_emqww	Infinite element y coordinate	m	y
S0y_guess_emqww	Inner y coordinate default guess	m	0
Sdy_guess_emqww	Width in y direction default guess	m	0
delta_emqww	Skin depth	m	$1/\text{real}(\sqrt{(j * \omega_{emqww} * \mu_{0_emqww} * \mu_{r_emqww} * (\sigma_{emqww} + j * \omega_{emqww} * \epsilon_{0_emqww} * \epsilon_{r_emqww}))})$
dVol_emqww	Volume integration contribution	m	detJ_emqww * d_emqww
Dx_emqww	Electric displacement, x component	C/m ²	$\epsilon_{xx_emqww} * E_{x_emqww} + \epsilon_{xy_emqww} * E_{y_emqww}$
Dy_emqww	Electric displacement, y component	C/m ²	$\epsilon_{yx_emqww} * E_{x_emqww} + \epsilon_{yy_emqww} * E_{y_emqww}$
epsilon_emqww	Permittivity	F/m	$\epsilon_{0_emqww} * \epsilon_{r_emqww}$
epsilonxx_emqww	Permittivity, xx component	F/m	$\epsilon_{0_emqww} * \epsilon_{rxx_emqww}$
epsilonxy_emqww	Permittivity, xy component	F/m	$\epsilon_{0_emqww} * \epsilon_{rxy_emqww}$
epsilonyx_emqww	Permittivity, yx component	F/m	$\epsilon_{0_emqww} * \epsilon_{ryx_emqww}$
epsilonyy_emqww	Permittivity, yy component	F/m	$\epsilon_{0_emqww} * \epsilon_{ryy_emqww}$
sigma_emqww	Electric conductivity	S/m	sigmaxx_emqww
Jdx_emqww	Displacement current density, x component	A/m ²	$j * \omega_{emqww} * D_{x_emqww}$
Jpx_emqww	Potential current density, x component	A/m ²	$-\sigma_{xx_emqww} * V_x$
Jx_emqww	Total current density, x component	A/m ²	$J_{ex_emqww} + J_{dx_emqww} + J_{px_emqww}$
Jdy_emqww	Displacement current density, y component	A/m ²	$j * \omega_{emqww} * D_{y_emqww}$
Jpy_emqww	Potential current density, y component	A/m ²	$-\sigma_{yy_emqww} * V_y$

Jy_emqww	Total current density, y component	A/m ²	Jey_emqww+Jdy_emqww+Jpy_emqww
normP_emqww	Electric polarization, norm	C/m ²	sqrt(abs(Px_emqww)^2+abs(Py_emqww)^2)
normDr_emqww	Remanent displacement, norm	C/m ²	sqrt(abs(Drx_emqww)^2+abs(Dry_emqww)^2)
normD_emqww	Electric displacement, norm	C/m ²	sqrt(abs(Dx_emqww)^2+abs(Dy_emqww)^2)
normE_emqww	Electric field, norm	V/m	sqrt(abs(Ex_emqww)^2+abs(Ey_emqww)^2)
normJp_emqww	Potential current density, norm	A/m ²	sqrt(abs(Jpx_emqww)^2+abs(Jpy_emqww)^2)
normJd_emqww	Displacement current density, norm	A/m ²	sqrt(abs(Jdx_emqww)^2+abs(Jdy_emqww)^2)
normJe_emqww	External current density, norm	A/m ²	sqrt(abs(Jex_emqww)^2+abs(Jey_emqww)^2)
normJ_emqww	Total current density, norm	A/m ²	sqrt(abs(Jx_emqww)^2+abs(Jy_emqww)^2)
Weav_emqww	Electric energy density, time average	J/m ³	0.25 * real(Ex_emqww * conj(Dx_emqww)+Ey_emqww * conj(Dy_emqww))
Wav_emqww	Total energy density, time average	J/m ³	Weav_emqww
Qav_emqww	Resistive heating, time average	W/m ³	0.5 * real(Jx_emqww * conj(Ex_emqww)+Jy_emqww * conj(Ey_emqww))
Ex_emqww	Electric field, x component	V/m	-invJxx_emqww * Vx
Ey_emqww	Electric field, y component	V/m	-invJyy_emqww * Vy

4.2.3. Subdomain 4-8, 10

Name	Description	Unit	Expression
dr_guess_emqww	Width in radial direction default guess	m	
R0_guess_emqww	Inner radius default guess	m	
Sx_emqww	Infinite element x coordinate	m	
S0x_guess_emqww	Inner x coordinate default guess	m	
Sdx_guess_emqww	Width in x direction default guess	m	
Sy_emqww	Infinite element y coordinate	m	
S0y_guess_emqww	Inner y coordinate default guess	m	
Sdy_guess_emqww	Width in y direction default guess	m	
delta_emqww	Skin depth	m	
dVol_emqww	Volume integration contribution	m	
Dx_emqww	Electric displacement, x component	C/m ²	
Dy_emqww	Electric displacement, y component	C/m ²	
epsilon_emqww	Permittivity	F/m	
epsilononx_emqww	Permittivity, xx component	F/m	
epsilononxy_emqww	Permittivity, xy component	F/m	
epsilononyx_emqww	Permittivity, yx component	F/m	
epsilononyy_emqww	Permittivity, yy component	F/m	
sigma_emqww	Electric conductivity	S/m	

Jdx_emqww	Displacement current density, x component	A/m ²	
Jpx_emqww	Potential current density, x component	A/m ²	
Jx_emqww	Total current density, x component	A/m ²	
Jdy_emqww	Displacement current density, y component	A/m ²	
Jpy_emqww	Potential current density, y component	A/m ²	
Jy_emqww	Total current density, y component	A/m ²	
normP_emqww	Electric polarization, norm	C/m ²	
normDr_emqww	Remanent displacement, norm	C/m ²	
normD_emqww	Electric displacement, norm	C/m ²	
normE_emqww	Electric field, norm	V/m	
normJp_emqww	Potential current density, norm	A/m ²	
normJd_emqww	Displacement current density, norm	A/m ²	
normJe_emqww	External current density, norm	A/m ²	
normJ_emqww	Total current density, norm	A/m ²	
Weav_emqww	Electric energy density, time average	J/m ³	
Wav_emqww	Total energy density, time average	J/m ³	
Qav_emqww	Resistive heating, time average	W/m ³	
Ex_emqww	Electric field, x component	V/m	
Ey_emqww	Electric field, y component	V/m	